Formation and Stability of the Solar Tachocline in MHD Simulations

Aniket Sule

Potsdam 2007

Elektronisch veröffentlicht auf dem
Publikationsserver der Universität Potsdam:
http://opus.kobv.de/ubp/volltexte/2007/1461/
urn:nbn:de:kobv:517-opus-14612
[http://nbn-resolving.de/urn:nbn:de:kobv:517-opus-14612]

Astrophysikalisches Institut Potsdam

Formation and Stability of the Solar Tachocline in MHD Simulations

Dissertation
zur Erlangung des akademischen Grades
”doctor rerum naturalium”
(Dr. rer. nat.)
in der Wissenschaftsdisziplin ”Astrophysik”
der Universität Potsdam

eingereicht an der
Mathematisch–Naturwissenschaftlichen Fakultät
der Universität Potsdam

von
Aniket Sule
Mumbai, Indien

Potsdam, July 6, 2007

Contents

Contents 5

List of Figures 7

1 Introduction 3
- 1.1 Equations of the Standard Solar Model 3
- 1.2 Helioseismology and the Internal Rotation of the Sun 5
- 1.3 Tachocline Properties 8
  - 1.3.1 Location and Shape 8
  - 1.3.2 Width 9
  - 1.3.3 Rotational Frequencies 10
  - 1.3.4 Variability of the solar tachocline 11
  - 1.3.5 Light Element Abundance 11
- 1.4 Modeling the Tachocline 13
  - 1.4.1 Tachocline Formation 13
  - 1.4.2 Tachocline Stability 14
- 1.5 The Numerical Procedure 15
  - 1.5.1 The MHD Equations 15
  - 1.5.2 The Numerical Code 17

2 Formation of the Solar Tachocline 21
- 2.1 Turbulent Tachocline Models 21
- 2.2 Models with Relic Poloidal Field 23
- 2.3 The Chosen Model 27
- 2.4 Results 29
  - 2.4.1 The effect of the meridional flow 29
  - 2.4.2 Varying the magnetic Prandtl number 33
  - 2.4.3 Varying the magnetic Reynolds number 34
  - 2.4.4 Effect on the Lundquist number 35
  - 2.4.5 Effect of a temperature gradient 38
- 2.5 Discussion 40

3 Hydrodynamic Stability **43**
3.1 Lower Dimensional Models . . . 43
3.2 The Model . . . 45
3.3 Results . . . 47
3.3.1 Stability of various solutions . . . 47
3.3.2 Effects of buoyancy . . . 49
3.3.3 Effects of higher-degree terms . . . 50
3.4 Discussion . . . 51

4 MHD stability of the tachocline **55**
4.1 Lower Dimensional Models . . . 56
4.2 The Model . . . 58
4.3 $\boldsymbol{m = 1}$ Mode Stability Analysis . . . 60
4.3.1 Rigid rotation . . . 60
4.3.2 Thickness of field belts . . . 63
4.3.3 Latitudinal differential rotation . . . 64
4.3.4 Full differential rotation . . . 65
4.4 Higher Azimuthal Modes: Linear simulations . . . 68
4.5 Non-linear Simulation . . . 70
4.6 Discussion . . . 71

5 Summary **75**

A Solar Parameters **79**

B Miscellaneous Formulae **81**

Bibliography **85**

List of Figures

1.1 Tachocline Anomaly 6
1.2 Internal rotation profile of the Sun 7
1.3 The mean radial position of the tachocline 9
1.4 The width of the tachocline 10
1.5 1.3 year cycle in the tachocline 12

2.1 Rüdiger & Kitchatinov (1997) results 24
2.2 MacGregor & Charbonneau (1999) results 25
2.3 Garaud (2001) results 26
2.4 Results for the magnetic field confined to radiative zone 29
2.5 Results for the magnetic field coupled to convection zone 30
2.6 Fractional Ω vs. fractional radius plots 32
2.7 B_{pol} snapshots 33
2.8 Meridional flow patterns 34
2.9 Meridional flow amplitudes for various Rm and Pm 35
2.10 Dependence of Lundquist Number on Pm 36
2.11 Dependence of Lundquist Number on Rm 37
2.12 Meridional flow cells and effect of buoyancy 38
2.13 Ω and B_ϕ including buoyancy 39
2.14 Meridional flow amplitudes including buoyancy 40

3.1 3D linear Ω profile 46
3.2 Flow streamlines on the outer surface 47
3.3 Marginal stability lines for symmetric $m = 1$ mode 48
3.4 Marginal stability lines for antisymmetric $m = 1$ and $m = 2$ modes 49
3.5 Rotation periods of the flow pattern 50
3.6 3D modified Ω profile 52
3.7 Lines of marginal stability including buoyancy force 52

4.1 Tayler instability 56
4.2 Background B_ϕ profile 59
4.3 Marginal stability lines for different symmetries and different Pm 61
4.4 Growing magnetic instability 62

4.5 Marginal stability lines for different Pm with the horizontal flow only . . . 63
4.6 Dependence on thickness of the field belt 63
4.7 Marginal stability lines for latitudinal differential rotation 65
4.8 Marginal stability lines for full differential rotation profile 66
4.9 Marginal stability lines for field belts at various latitudes 67
4.10 Results for higher azimuthal modes 68
4.11 Fourier spectrum of the velocity fields 70
4.12 Time series evolution of the velocities in a non-linear simulation 72

A.1 Variation of density and temperature inside the Sun 79

Abstract

The solar tachocline is a thin transition layer between the solar radiative zone rotating uniformly and the solar convection zone, which has a mainly latitudinal differential rotation profile. This layer has a thickness of less than $0.05R$ and is subject to extreme radial as well as latitudinal shears. Helioseismological estimates put this layer at roughly $0.7R$. The tachocline mostly resides in the sub-adiabatic, non-turbulent radiative interior, except for a small overlap with the convection zone on the top. Many proposed dynamo mechanisms involve strong toroidal magnetic fields in this transition region.

The exact mechanisms behind the formation of such a thin layer is still disputed. A very plausible mechanism is the one involving a weak, relic poloidal magnetic field trapped inside the radiative zone, which is responsible for expelling differential rotation outwards. This was first proposed by Rüdiger & Kitchatinov (1997). The present work develops this idea with numerical simulations including additional effects like meridional circulation. It is shown that a relic field of 1 Gauss or smaller would be sufficient to explain the observed thickness of the tachocline.

The stability of the solar tachocline is addressed as the next part of the problem. It is shown that the tachocline is stable up to a differential rotation of 52% in the absence of magnetic fields. This is a new finding as compared to the earlier two dimensional models which estimated the solar differential rotation (about 28%) to be marginally stable or even unstable. The changed stability limit is attributed to the changed stability criterion of the 3-dimensional model which also involves radial gradients of the angular velocity.

In the presence of toroidal magnetic field belts, the lowest non-axisymmetric mode is shown to be the most unstable one for the radiative part of the tachocline. It is estimated that the tachocline would become unstable for toroidal fields exceeding about 100 Gauss. With both formation and stability questions satisfactorily addressed, this work presents the most comprehensive analysis of the physical processes in the solar tachocline to date.

Chapter 1

Introduction

Sun, the primary source of energy for the entire life on the Earth! It has been observed and studied right since the dawn of civilization. Be it Egyptians, Indians or Mayans, the Sun was the most fascinating object for the ancients. Scientists since Galileo have kept track of all the observable changes on the Sun. But after all these years, do we completely understand our Sun?

The observers have made headway in the physics of the outer layers of the Sun like photosphere, chromosphere and corona. The standard solar model has parameterized the Sun in terms of various physical quantities. Yet dynamics of the solar interior is poorly understood. To understand this, let us begin with the basic equations governing the equilibrium of the Sun.

1.1 Equations of the Standard Solar Model

The Sun is a self-gravitating sphere of plasma. Its energy is generated by nuclear fusion at its core, which then is radiated through the solar radiative zone till the base of the convection zone at roughly 0.7 solar radii ($R_\odot$). It is then transported outwards by solar convection. Within a good approximation (assuming non-rotation) the Sun is spherically symmetric and this assumption helps in understanding the physics of the Sun in a set of simple equations.

At every point in the Sun, outward pressure of the expanding gas is balanced by the self-gravitation. This gives rise to “Equation of hydrostatic equilibrium”.

$$\frac{dP(r)}{dr} = -\frac{GM(r)\rho(r)}{r^2}, \tag{1.1}$$

where $P(r)$ is the hydrostatic equilibrium pressure, $\rho(r)$ is the density at radius r. G is the universal gravitational constant. As pressure is the equilibrium pressure, this equation corresponds to the mean state of the Sun.

The equation of continuity is given by,

$$\frac{dM(r)}{dr} = 4\pi r^2 \rho(r). \tag{1.2}$$

Next we should consider the equation governing the energy production in the Sun. The energy generation rate per unit mass (ϵ) is a quantity, which depends on various factors viz the local temperature, local density, metalicity and hydrogen fraction amongst other things. Combining the first and the second law of thermodynamics, for a given ϵ, we can write,

$$\frac{dL(r)}{dr} = 4\pi r^2 \rho(r)(\epsilon - T(r)\frac{\partial S}{\partial t}), \tag{1.3}$$

where $L(r)$ is the total luminosity generated inside a sphere of radius r, $T(r)$ is the local temperature and S is the thermodynamic entropy.

Once the energy is generated, it needs to be transported to the exterior of the Sun. The "energy transport equation" simply states that the total flux coming out of the sphere of radius r is sum of its radiative flux and convective flux. The third mode of energy transport, Conduction, is negligible for the Sun. This equation gives the relation between the temperature gradient and the output flux of the photons. The efficiency of this process (which is a function of temperature and opacity) determines the total luminosity of the Sun. The linearized equation of the process, assuming local thermodynamic equilibrium is given by

$$\begin{aligned} \frac{L(r)}{4\pi r^2} &= F_{\rm rad} + F_{\rm conv} & (1.4) \\ &= -\left(\frac{16\sigma T^3(r)}{3\kappa\rho(r)}\right)\frac{dT(r)}{dr} + F_{\rm conv}, & (1.5) \end{aligned}$$

where κ is the Rosseland mean opacity and σ the Stefan's constant. The quantity in the bracket gives the local heat conductivity. When the temperature gradient required to transport all the energy by radiation exceeds the adiabatic temperature gradient, the energy is physically transported outwards by the material. In this case the convective flux dominated the energy transport equation.

The hydrostatic equilibrium of the Sun is governed mainly by 5 variables, $L(r)$, $P(r)$, $\rho(r)$, $T(r)$ and $M(r)$. We aim to solve the solar equations self-consistently to arrive at the solutions of these variables. The "equation of state", "opacity equation" and the "energy generation equation" of the Sun supplement the equations above for the complete solar model. In practice, however these three equations depend on the chemical composition inside the Sun. The quantum effects come into play close to the center of the Sun. However, for the bulk of the radiative zone, we can approximate the equation of state by the ideal gas Law. In the outer layers, good approximation for it is given by Saha Ionization equation.

The actual energy generation inside the Sun is given by nuclear fusion reactions such as proton-proton (pp) chain and carbon-nitrogen-oxygen (CNO) cycle.

With all the equations and physical parameters fairly well known, we can numerically evolve the Sun from an initial stage (zero-age model) till the current age (≈ 5 Gyr.). A range of models with different initial Helium abundances (Y_0) and mixing length parameters (α) are evolved and the outputs are compared with the present solar luminosity and the radius. By doing this process iteratively, the zero-age model can be tuned up to the initial conditions, which can reproduce the present day Sun. At this point, we get a good detailed model for structure of a non-rotating solar mass star.

However, till recently, these models could be matched only with the observables at the solar surface as, barring neutrinos, there were no tools to probe the solar interior. The accurate measurement and continuous monitoring of the solar oscillations has opened a new branch of observations called helioseismology in the last few years. It has breathed new life in the physics of the solar interior.

1.2 Helioseismology and the Internal Rotation of the Sun

The oscillations on the solar surface were first reported by Leighton et al. (1962). These oscillations are predominantly sound waves, p-modes, with most typical period of 5 minutes. They are stochastically excited and linearly damped by the turbulent motions in the convection zone. Grec et al. (1980) were the first to show that power spectrum of the Sun is a discreet one, thus leading to the thought that accurate measurement of these frequencies could provide information about the internal structure of the Sun.

The standard solar model described in the previous section has parameterized the Sun at different radii. With parameters like sound speed inside the Sun, the solar density etc. specified, the stable oscillatory frequencies can be predicted and the cross-check with the observed helioseismic frequencies can help in refining the model. The SOHO telescope at the Sun-Earth L1 point and group of 6 earth based observatories under the GONG group are continuously monitoring the Sun for finer as well as long period observations. Many discoveries in the recent years like measurement of the depth of the solar convection zone, independent measurement of solar radii, determination of microscopic properties of the Sun are attributed to helioseismology. Yet, none of it is as important as the solar tachocline.

The helioseismic estimation of the sound speeds inside the Sun was found to be well in agreement with the standard solar model except for a small layer near $0.7R$. The particular anomaly near $0.7R$ is clearly visible in the Figure 1.1. In the figure the deviation of the observed sound speeds from the solar model is plotted. One can clearly see a sudden peak at about $0.7R$, giving indication that the Sun is hotter in this region than predicted by the models. This layer formed at the junction of the outer side of solar radiative zone and the inner side of solar convection zone is called the tachocline.

Any small amplitude oscillation on the solar surface can be expressed in terms of spherical harmonics as a function of the axial modes[1] (l), giving dependence on co-latitudes and azimuthal modes (m), giving dependence on the longitudes. At zero rotation, these two types of modes are degenerate from each other. However, as the Sun is rotating, the oscillation frequencies for given azimuthal modes split in to couplets. This frequency line splitting gives a handle on probing the sound speeds inside the sun, which in turn help in

---

[1] The word 'modes' maybe misleading here as the l and m are merely different harmonics in axial or azimuthal direction, yet it is used for brevity.

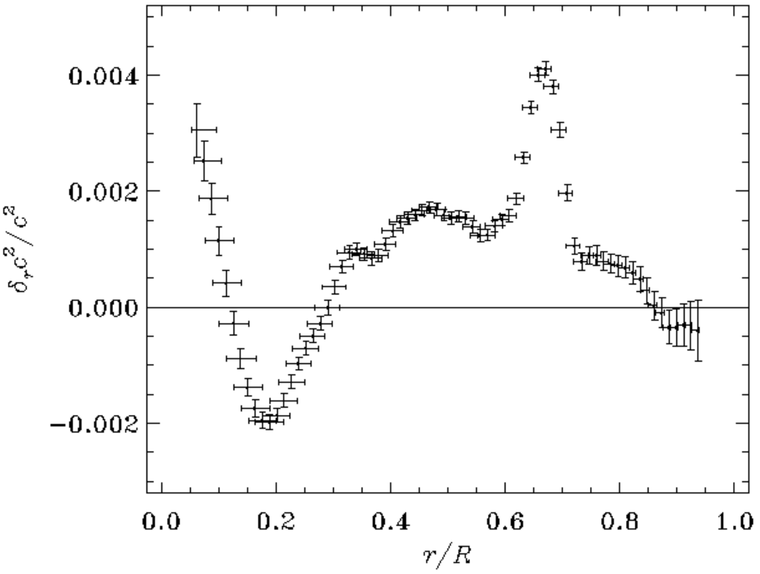

Figure 1.1: Deviation of helioseismically observed squared sound speed from the model prediction.

constructing the rotation profile inside the sun. In this case, solar structures at different depths is reflected in different ls. An exhaustive review of the basic helioseismological techniques and their employment in measuring the internal rotation rate of the Sun is given in Thompson et al. (2003). When the internal rotation profile of the Sun is obtained, this layer is clearly distinguishable. The latitudinal differential rotation of the solar surface was first quantized by Newton & Nunn (1951). Since then many authors have expressed the solar rotation rate as,

$$\Omega(\theta) = \Omega_{\mathrm{eq}}(1 - \alpha_2 \cos^2\theta - \alpha_4 \cos^4\theta). \tag{1.6}$$

Here Ω_{eq} is the angular velocity at the solar equator and θ is the colatitude. With both α_2 and α_4 positive, it dictates that the rotational rate at the equator is maximum and it gradually decreases towards the pole. Out of the three constants, α_4 is the most elusive one as it depends on the accurate determination of the rotation rate near the pole. Prior to helioseismology, the surface observations estimated these constants to be,

$$\Omega_{\mathrm{eq}} = 2.87 \times 10^{-6} \text{ rads}^{-1} \text{ and } \alpha_2 = 0.19, \tag{1.7}$$

With the advent of helioseismology, these constants can be determined in an unprecedented detail. The key features of the solar rotation profile as determined by helioseismology can be summarized as follows:

- The solar convection zone, except a thin layer at the surface undergoes latitudinal shear but nearly no radial shear. This means, the rotation rate at any point in the convection zone depends strongly on its latitude and much weakly on the distance

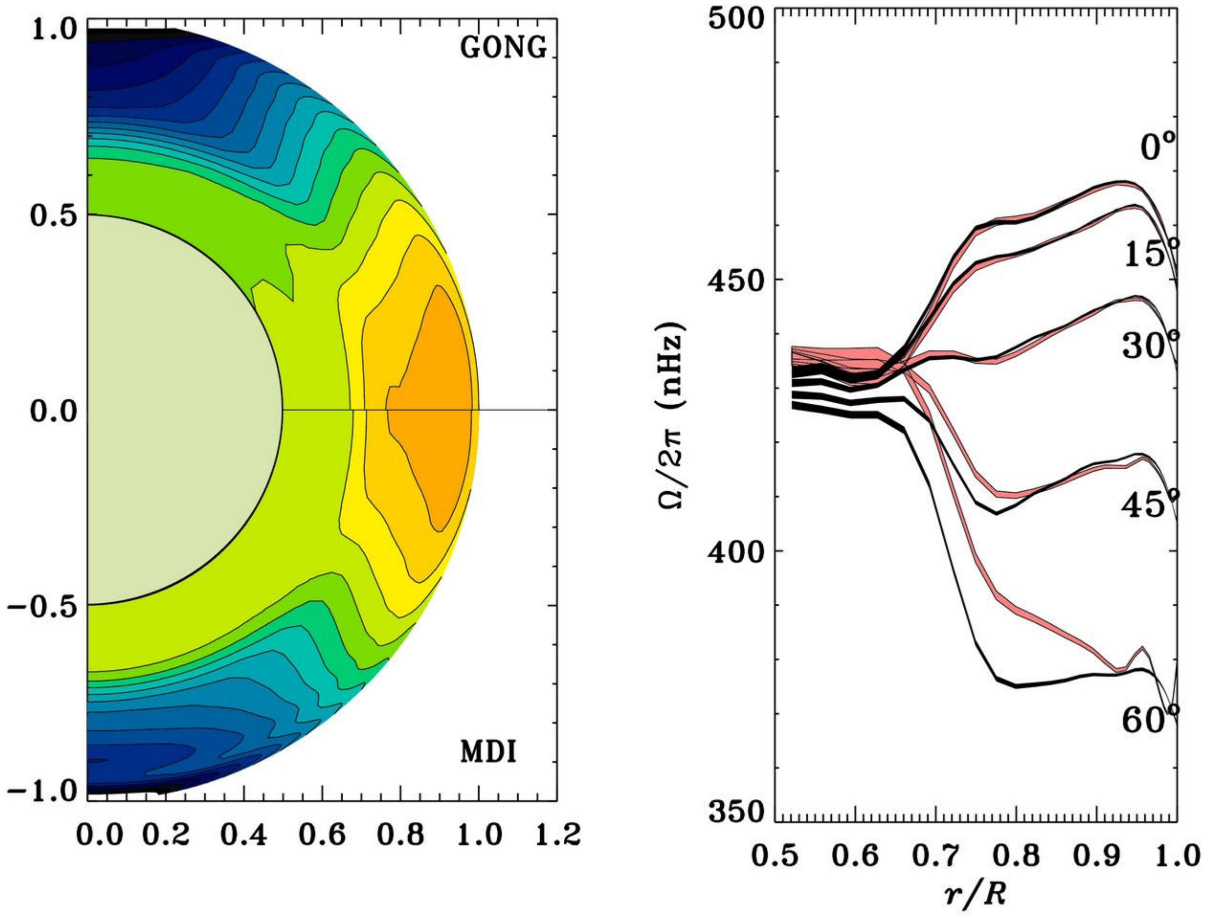

Figure 1.2: Internal rotation profile of the Sun as per 2 different datasets. The left panel shows 2-D plot of iso-contours of the rotation rate with yellow (grey) corresponding to the fastest rotation and black corresponding to the slowest rotation. The data from GONG and MDI projects is shown separately in upper and lower half respectively. The right panel shows the latitudinal rotation frequencies as a function of fractional radius. The GONG and MDI datasets are represented by black and red (grey) colour respectively. Source: R. Howe's presentation (2002).

from the centre. This feature was in contradiction with then existing solar models, which had predicted cylindrical rotation or the so called Taylor-Proudman flow inside the Sun. The latitudinal rotation profile invited a complete revision of this model, which is still an ongoing process.

- The shear layer at the solar surface is another interesting feature of this profile. As seen in the right side panel, the rotation rates suddenly drop after $0.95R$. Consequently, this layer has strong radial shears.

- The solar radiative zone is rotating almost uniformly below $0.65R$ all the way upto

$0.2R$. No significant deviation from uniform rotation is found down to $0.2R$. Its angular velocity is slightly less than that at the equator.

- The uniform rotation in the radiative zone spreads out to latitudinal differential rotation in a very thin layer called tachocline.

The same is shown in the Figure 1.2. In the left panel, the contours clearly show uniformly rotating radiative zone and latitudinal rotation in the convection zone. In the right panel, same is depicted by the fact that at lower radius, lines for different latitudes are nearly inseparable and at the outer part, they are nearly constant but well spread out. The layer between these two regions is the tachocline. In the last 3 years, observations have constrained the tachocline to be even thinner.

1.3 Tachocline Properties

The presence of the shear layer at the base of convection zone was reported as early as 1989 by Brown et al. But, the first definitive measurements of the tachocline properties were carried out by Thompson et al. (1996) by GONG data and Kosovichev et al. (1997) using MDI data. Since then many groups have generated information about basic properties of the tachocline such as its location, shape, size, rotation rate of the radiative zone and latitudinal dependence of the rotation.

1.3.1 Location and Shape

It is generally agreed that tachocline is situated at the base of convection zone at roughly $0.7R$. The best known estimate for tachocline position are given by Kosovichev (1996) (Eq. 1.8), Antia et al. (1998) (Eq. 1.9) and Basu & Antia (2001) (Eq. 1.10).

$$\begin{aligned} r_{\mathrm{k}} &= (0.692 \pm 0.005)R, & (1.8)\\ r_{\mathrm{a}} &= [(0.6991 \pm 0.0099) + (0.0030 \pm 0.0061)P_2(\theta)]R, & (1.9)\\ r_{\mathrm{ba}} &= [(0.6936 \pm 0.0020) + (0.0047 \pm 0.0010)P_2(\theta)]R, & (1.10)\end{aligned}$$

where $P_2(\theta) = 5\cos^2\theta - 1$.

We see the uncertainties in the values have gradually gone down over the years, yet the results are consistent with each other. Results by various other authors like Schou et al. (1998), Charbonneau et al. (1999b), Howe et al. (2000a) and Eff-Darwich et al. (2002) are similar to these estimates. The use of Legendre polynomial in Eqs. (1.9), (1.10), suggests that the midpoint of the tachocline is not equidistant from solar radius at various latitudes. The tachocline is clearly prolate, which implies that larger part of the tachocline is likely to be inside convection zone for the polar latitudes. This fact will have to be borne in mind while simulating the part of the tachocline inside the solar radiative zone. Also we must note, as shown by Schou et al. (1998), that these best fits drawn from the lower latitudes data may not be best fits in the polar region.

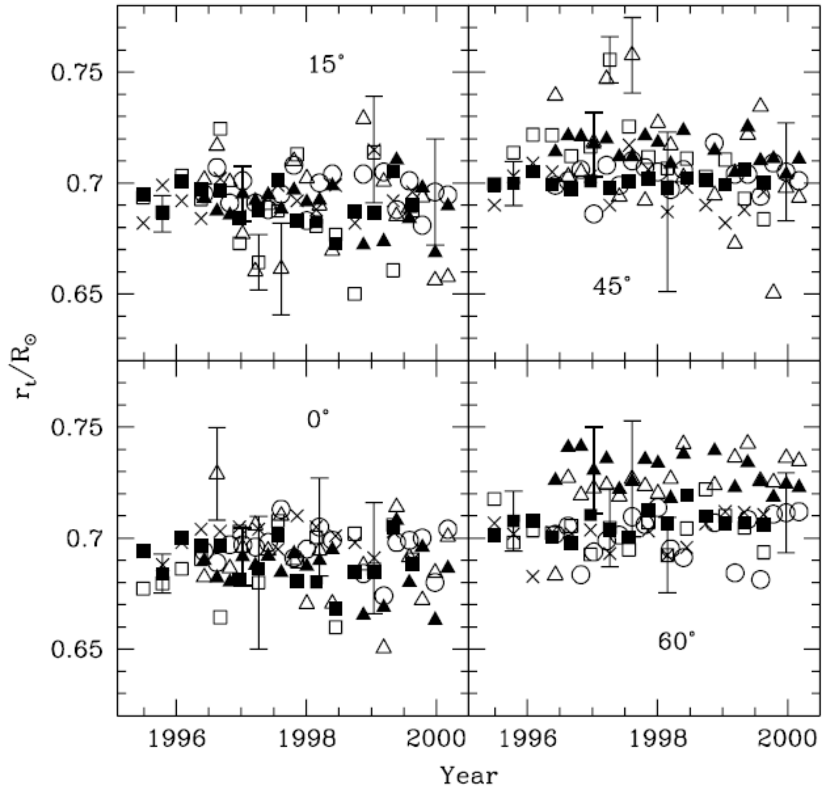

Figure 1.3: The mean radial position of the tachocline at few selected latitudes. The crosses and circles show the results from the calibration method for GONG and MDI data, the open squares and triangles show the 1D annealing results from the GONG and MDI data, while the filled squares and triangles show the results from 2D annealing for GONG and MDI data. Source: Basu & Antia (2001).

1.3.2 Width

The width of the tachocline is differently defined by different authors. Kosovichev (1996), Charbonneau et al. (1999b) (Eq. 1.11) and others describe the tachocline rotation profile as an error function. The width of the tachocline is the thickness for which the error changes from 0.08 to 0.92. On the other hand, others like Antia et al. (1998) (Eq. 1.12) and Basu & Antia (2001) (Eq. 1.13) have chosen to take the width as the thickness of the layer for which, the actual rotation rate increases from a factor $1/(1+e)$ to $1-1/(1+e)$ of its maximum value at a given latitude. We adopt to the first definition. When scaled accordingly, all the results, along with numerous others, agree that thickness of the tachocline is $0.05R$ or smaller.

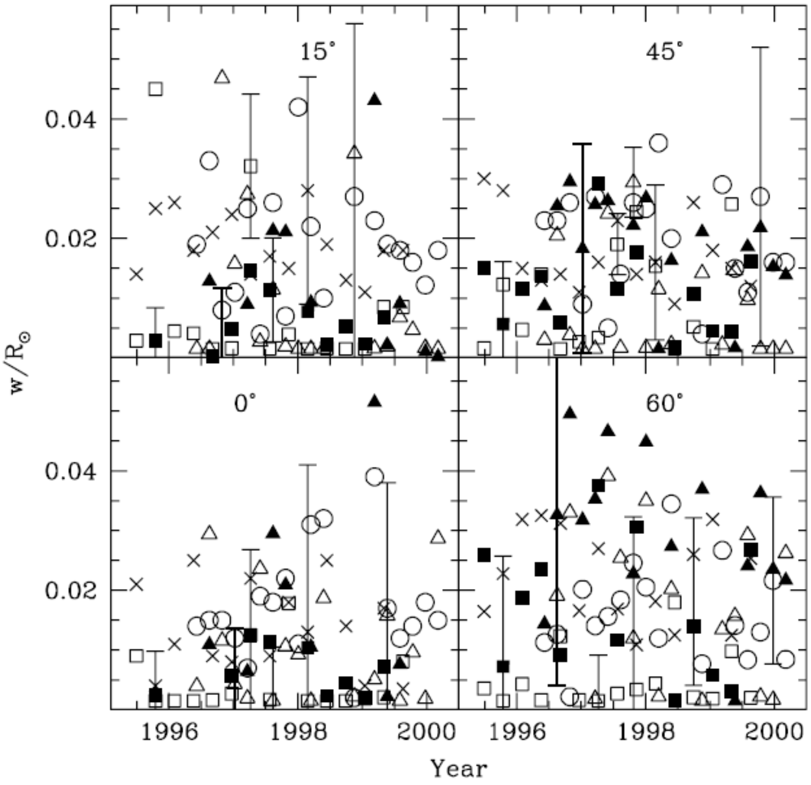

Figure 1.4: Width of the tachocline at few selected latitudes. The data points have same meaning as Figure 1.3. Source: Basu & Antia (2001).

$$\begin{aligned} w_{\rm low} &= (0.039 \pm 0.013)R \quad \text{(at the equator)}, \\ w_{\rm high} &= (0.042 \pm 0.013)R \quad \text{(at 60)}, \qquad (1.11) \\ w_{\rm a} &= [(0.0412 \pm 0.0353) + (0.0230 \pm 0.0206)P_2(\theta)]R, \qquad (1.12) \\ w_{\rm ba} &= [(0.0235 \pm 0.0044) + (0.0142 \pm 0.0083)P_2(\theta)]R. \qquad (1.13) \end{aligned}$$

Again here, the dependence of the tachocline width on the Legendre polynomial implies that the tachocline becomes thicker at the higher latitudes. At the same time, Basu & Antia (2001) claim that position of the base of convection zone or the overshoot layer do not show any significant latitudinal dependence. Thus, tachocline has larger overlap with the convection zone at polar latitudes.

Converting these estimates in physical units, tachocline width may be less than 10Mm at the equator and may be as high as 70Mm near the pole.

1.3.3 Rotational Frequencies

The solar convection zone undergoes latitudinal differential rotation. As the rotation rate weakly depends on radius, the best fit for the rotation profile is mentioned along with the radius at which it was measured. The rotational rate at various latitudes at the base of convection zone is given by Antia et al. (1998) (Eq. 1.15), Schou et al. (1998) (Eq. 1.14) and also by Basu & Antia (2001) (Eq. 1.15).

$$\begin{aligned}
\Omega_{\mathrm{s}}(\theta) &= (455.8 - 51.2\cos^2\theta - 84.0\cos^4\theta) \quad \mathrm{nHz} \quad \text{(at lower latitudes)}, && (1.14)\\
\Omega_{\mathrm{a}}(\theta) &= (436.6 \pm 2.2) - [(1.83 \pm 2.18) + (22.71 \pm 1.01)P_2(\theta) \\
&\quad +(3.88 \pm 0.45)P_4(\theta)] \quad \mathrm{nHz}, && (1.15)\\
\Omega_{\mathrm{ba}}(\theta) &= (436.6 \pm 2.2) - [(1.17 \pm 0.68) + (21.86 \pm 0.21)P_2(\theta) \\
&\quad +(3.44 \pm 0.11)P_4(\theta)] \quad \mathrm{nHz}, && (1.16)
\end{aligned}$$

where $P_4(\theta) = 21\cos^4\theta - 14\cos^2\theta + 1$.

In Eq. (1.14), the first term represents the equatorial frequency of the convection zone. Schou et al. (1998) noted that the rotation rate in the radiative core is the same as that at 30 latitude in the convection zone. On the other hand, in the Eqs. (1.15), (1.16), the first term gives the rotation rate in the radiative core. These equations also agree that the rotation rate at roughly 30 latitude is same as that in the radiative interior. Similar inversions have also been shown graphically by, Howe et al. (2000a), Eff-Darwich et al. (2002) and Howe (2003) amongst others.

From the equations, it is clear that the pole is rotating with a frequency of about $28 - 30\%$ less than that of equator. This is defined as percentage differential rotation. If for some body, the rotation rate is zero near the pole then the percentage differential rotation will be 100%. For a body where pole rotates faster than the equator (also called anti-solar like), the percentage differential rotation will be negative.

1.3.4 Variability of the solar tachocline

After studying 4 years of MDI as well as GONG data, Howe et al. (2000a) concluded that the equatorial rotation rate at various depths inside the Sun including the rate at the tachocline is variable in an oscillatory manner with a period of roughly 1.3 years (see Figure 1.5). But the observations at 30 as well as 60 failed to show any trace of statistically significant oscillation. These results are also contested by Basu & Antia (2001). They report no significant periodicity in the data used by them and also point out that the only hint of oscillation in the Howe et al. (2000a) is from the GONG data alone which is not well corroborated by the MDI data. The existence of any temporal variation in the tachocline is still an open question.

1.3.5 Light Element Abundance

The convection zone and the overshoot layer, thoroughly mix chemical elements on a very short timescale. As a result, the abundances of the chemical elements, as observed on the solar surface, are constant throughout the convection zone. As the convection zone flows also reach upper layers of the tachocline, it would be reasonable to assume that these elements are also present in the tachocline in same proportion. Light elements like

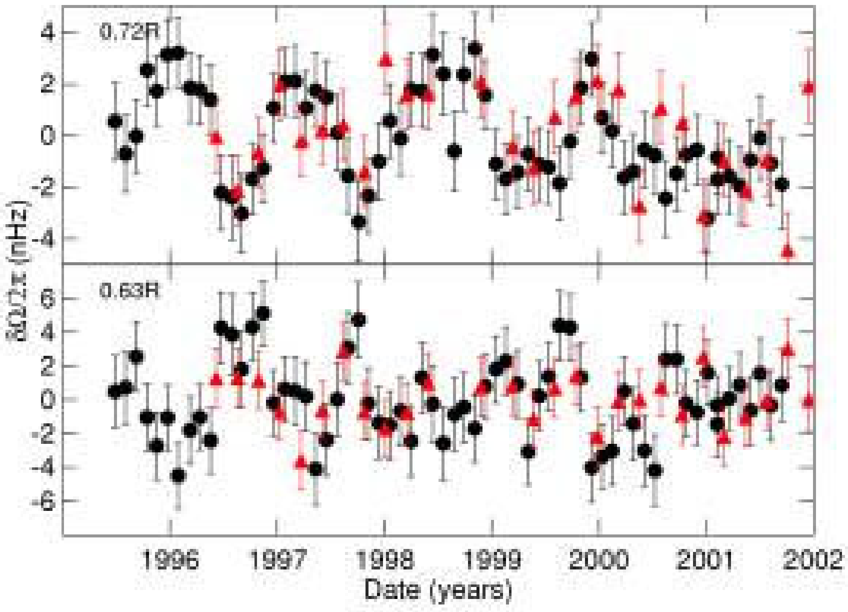

Figure 1.5: Possible 1.3 years temporal variation in the tachocline as seen in the Gong (black) and MDI (red) data. The difference from the time-averaged angular velocity is plotted. The upper plot is for the equatorial region and the lower plot is for higher latitudes. Source: R. Howe's presentation (2002)

Lithium (Li), Beryllium (Be) and Boron (B) have been observed on the solar surface, albeit in a depleted quantity. The temperature in most of the radiative zone is high enough to destroy these elements (for e.g. Be will be destroyed by fusion below $0.61R$, while Li will be destroyed below $0.67R$). This puts a constraint on the efficiency of the mixing of elements in the tachocline and its interaction with the radiative zone. the depleted proportion of the light elements at the solar surface, as compared to the solar models, tells us that there should be some mixing also in the tachocline but as Rüdiger & Pipin (2001) have pointed out, if the tachocline is as turbulent as the convection zone, there wouldn't be any trace of light elements after gigayears of the solar life. It has been argued there that the turbulent velocities in the tachocline, assuming only horizontal turbulence, should be atleast 3-4 orders weaker than those in the convection zone. It is further argued that the turbulent velocities should be even weaker if a full 3-dimensional model is taken into account. Thus, the light elements put a constraint that although the tachocline needs to be turbulent, the turbulence should be very weak as compared to the convection zone.

Any good tachocline model needs to take into account the restrictions imposed by these parameters.

1.4 Modeling the Tachocline

The existence of tachocline raises many fundamental questions. We would like to know why radiative zone is rotating more or less uniformly whereas there is differential rotation in the convection zone. Probing further, it would be good to know why tachocline, the shear layer between the two is so thin. Also the important question, if the tachocline is stable in the solar case, needs to be addressed. In this work I attempt to tackle these questions and related issues.

1.4.1 Tachocline Formation

There are various theories regarding formation of the tachocline. First model attempting to explain tachocline was a hydrodynamic one, given by Spiegel & Zahn (1992). Although this approach was followed by others like Elliott (1997) and Miesch (2003), the model suffered from the primary drawback that the resultant tachocline thickness was more than $0.1R$.

Some others, primarily Forgács-Dajka & Petrovay (2002) and Petrovay (2003) take the view that the tachocline entirely belongs to the convection zone. The stark contrast between the convection zone and the sub-adiabatic radiative interior is the onset of turbulence in the convection region. As a result, viscosity, thermal conductivity and magnetic diffusivity are much higher in the convection zone. Stix & Skaley (1990) estimated that these quantities are as small as $O(10)$ in the radiative zone and as large as $O(10^9)$ or higher in the convection zone. As shown by helioseismology, some parts of the tachocline, especially at the polar latitudes may indeed reside inside convection zone, but these large diffusivities also make diffusive timescales very short and thus numerical simulations using this approach are restricted to the study of short timescale (of the order of a solar cycle or less) variations in the tachocline and say little about formation of the tachocline itself.

Most successful approach to explain the tachocline formation has been the MHD evolution of the solar interior and the tachocline with the help of a relic magnetic field. This approach assumes that the most of the tachocline is a part of the radiative zone rather than the convection zone. This is certainly consistent with the picture of the Sun we get from the helioseismology and the standard solar model. The model also assumes that at the time of formation of the Sun, a small random poloidal field may have been entrapped inside the radiative zone. If we separate any random field in multipoles, it turns out that the axisymmetric dipole mode takes the longest time to decay through magnetic diffusion. With microscopic magnetic diffusivity inside the radiative zone, diffusion time for the dipole field may even be longer than the solar life time. Thus, it would be logical to assume that the field in the radiative interior may be predominantly a dipolar one.

Rüdiger & Kitchatinov (1997) introduced this idea of magnetic field as primary agent of the tachocline formation. The significance of this model was explained independently by Gough & McIntyre (1998). Since then many others like Charbonneau et al. (1999b), Garaud (2001) etc. have used similar models to explain the observed structure of the tachocline. I have also used the model of Rüdiger & Kitchatinov (1997) as a starting point and performed axisymmetric simulations for the formation of the tachocline. All these models and subsequent simulations will be discussed in detail in Chapter 2.

1.4.2 Tachocline Stability

The other key issue in case of the tachocline is its stability. Should the tachocline be completely unstable and hence turbulent, the light elements in the convection zone will be effectively transported to deep layers of radiative zone where they will be destroyed. As the light elements on the solar surface have survived till date, albeit in a depleted quantity, one can deduce that the lower layers of the tachocline should be much more stable than the convection zone i.e. only weakly turbulent. The diffusivities in these layers might be an order or two higher than the radiative zone but they should still be substantially smaller than diffusivities in the convection zone. The depleted quantities of the light elements are then explained by large scale meridional flows coupling the tachocline with the radiative zone below (Rüdiger et al. 2005). Can such a thin layer subject to extreme shears remain stable? What are the key parameters governing the stability criteria? These are just a few of the questions which need to be answered in the context of the solar tachocline. Further, we would also like to know if we can extend the same analysis to other stars and can gauge some general pattern.

The hydrodynamic stability of spherical, inviscid fluid surface under the influence of latitudinal differential rotation was first probed by Watson (1981). He concluded that the instability should set in at a differential rotation of about 28.6%. As seen above, this figure is roughly same as the total differential rotation in the Sun which implies that the Sun may just be marginally stable or even unstable, if the solar rotation profile would contain just the α_2 term from the eq. 1.6. However, the solar rotation profile is more complex and the higher order terms were suspected to have significant influence on the stability of the tachocline. Dikpati & Gilman (2001) revisited the issue with the aid of helioseismological data and performed the analysis again for the spherical surface allowing deformations along the radial extent. The results threw another surprise as the critical differential rotation for the overshoot part of the tachocline was found to be as low as 11%. As mentioned above, since the lower layers of the tachocline can only be weakly turbulent, some piece of this puzzle seems to be missing. In Chapter 3, the hydrodynamic stability problem is revisited with linearized 3-dimensional simulations.

The relic poloidal magnetic field in the solar interior produces belts of toroidal magnetic field in the solar tachocline region. This toroidal field is expected to be larger than the poloidal field by 6 orders of magnitude or even more. Most popular solar dynamo models assume that this winding up of toroidal magnetic fields produces a field of $O(10^5)$ G which, along with the differential rotation in the tachocline, acts as an engine for the dynamos. The emergence of sun-spots on the solar surface, have put an observational constraint on the minimum toroidal field strength required in the tachocline for such models (Choudhuri & Gilman 1987; D'Silva & Choudhuri 1993). It is possible that such strong magnetic fields can further destabilize the tachocline.

The stability of purely toroidal magnetic fields against adiabatic perturbations were investigated analytically by Tayler (1973). It was found that a large class of configurations of toroidal fields is unstable in the linear treatment. Non-axisymmetric modes were more unstable than axisymmetric modes. This instability is known as Tayler instability. Spruit (2002) showed that Tayler Instability is the most important in this regard. The stability of toroidal fields on the tachocline has been studied by a host of authors, under suitable approximations. Most notable are the works of Gilman & Fox (1997), Dikpati & Gilman (1999) and Gilman & Dikpati (2000), which study instabilities on a 2-dimensional spherical surface; Dikpati et al. (2003) and Cally et al. (2003), which extend the analysis to allow perturbations of the spherical surface in radial direction (so-called shallow water approximation) and Cally (2003), which employs full, 3D shell, albeit ignoring radial shears, magnetic field gradients as well as viscous drag. On the other hand, authors like Forgács-Dajka & Petrovay (2002) and Petrovay (2003) concentrate on the turbulent part of the tachocline which resides just below the convection zone in the overshoot layer to explain short timescale phenomenon like the observed 11-year cycle of the sun-spots on the solar surface. Similar to hydrodynamic stability analysis, MHD instabilities are examined with full, 3-dimensional, linearized MHD simulations in the Chapter 4.

1.5 The Numerical Procedure

This section briefly describes the governing MHD equations, various approximations involved, the numerical code and also defines various parameters involved. The treatment here is more general, whereas specific deviations from this generalized form for various simulations will be discussed at their appropriate places.

1.5.1 The MHD Equations

The Sun is a rotating sphere of plasma mostly made up of Hydrogen and Helium. Thus, it will be reasonable to apply equations of fluid dynamics to the Sun. To avoid complexities in the simulations, we can assume the background density profile of this fluid plasma (ρ) as well as its kinematic $(\nu)^2$, thermal (χ) and magnetic (η) diffusivities are uniform throughout. The density fluctuations from this constant background profile are permitted through the buoyancy force. This is a fair assumption for the shells of the thickness of tachocline. However, all these quantities change by about two orders of magnitude across the width of radiative zone. Nevertheless, we will continue with this assumption due to limitations of the computational resources.

The general equation governing the motion of continuous, incompressible fluid or plasma is called Navier-Stokes equation. It is given by

$$\rho \frac{\partial \boldsymbol{u}}{\partial t} = -\rho(\boldsymbol{u} \cdot \nabla)\boldsymbol{u} - \nabla P + \rho\nu\nabla^2\boldsymbol{u} + \boldsymbol{F}. \tag{1.17}$$

---

[2] also known as viscous diffusivity

In this equation, $\boldsymbol{u}$ is the velocity of the fluid, P is the gas pressure and $\boldsymbol{F}$ is the total external force acting on the fluid. As we subject this sphere to the magnetic fields, differential rotation and temperature gradients with self-gravitation, the external force consists of centripetal force, Lorentz force and buoyancy force. Thus Eq. (1.17), with Boussinesq approximation, takes the form,

$$\frac{\partial \boldsymbol{u}}{\partial t} = -(\boldsymbol{u}\cdot\nabla)\boldsymbol{u} - \frac{1}{\rho_0}\nabla P + \nu\Delta\boldsymbol{u} + \frac{1}{\mu_0\rho_0}(\nabla\times\boldsymbol{B})\times\boldsymbol{B} + \frac{\rho(r)\cdot\boldsymbol{g}}{\rho_0}, \tag{1.18}$$

where $\boldsymbol{B}$ is the magnetic field and $\boldsymbol{g}$ is the gravitation term, which also absorbs the effect of temperature gradient. As per the standard practice in the Boussinesq approximation, the $\rho(r)$ symbol denotes local density at the radius r, which may differ from the average density ρ_0.

The evolution of the magnetic field is described by the induction equation. In the Eq. (1.19), magnetic field is constantly generated by the first term on the R.H.S. and is dissipated through diffusion by the second term.

$$\frac{\partial \boldsymbol{B}}{\partial t} = \nabla\times(\boldsymbol{u}\times\boldsymbol{B}) + \eta\Delta\boldsymbol{B}. \tag{1.19}$$

If the varying background profiles for η, ν or ρ are used then one has to make several changes in these equations. In Eq. (1.18), the $-\nu\nabla\times(\nabla\times\boldsymbol{u})$ term, which is absorbed in $\nu\triangle\boldsymbol{u}$ would change to $-\nabla\times(\nu\nabla\times\boldsymbol{u})$. Similarly, in Eq. (1.19), the $-\eta\nabla\times(\nabla\times\boldsymbol{b})$ term, which is absorbed in $\eta\triangle\boldsymbol{b}$ would change to $-\nabla\times(\eta\nabla\times\boldsymbol{b})$. This will include additional terms in the computation, and demand a decent radial resolution in the central part (i.e. away from the boundaries) of the computational domain. As Chebyshev polynomials used in the code are most effective in resolving the boundary layers, the additional points in the central region would mean a significant increase in the radial resolution forcing smaller time steps. The time stepping has lower bound as after a certain stage random noise in the code becomes comparable to the change in numerical values of the velocity and magnetic field rendering the computation useless. For the density variation the situation is even more complex. If a varying density profile is used in the background, then the code instead of the velocity field calculates the product $\rho\cdot\boldsymbol{u}$. To obtain the velocity field from these, the computational time for a simple $1/r$ type of density profile increases by atleast an order of magnitude. The trade-off of saving the computational time by constant background density profile was considered as an appropriate choice.

As there is no source or sink for the velocity field, we get solenoidal conditions in terms of Eqs. (1.20) and (1.21).

$$\nabla\cdot\boldsymbol{u} = 0, \tag{1.20}$$

$$\nabla\cdot\boldsymbol{B} = 0. \tag{1.21}$$

The temperature of the fluid is evolved through Eq. (1.22);

$$\frac{\partial T}{\partial t} = \chi\Delta T - \boldsymbol{u}\cdot\nabla T. \tag{1.22}$$

In this equation, it is assumed that the contribution from viscous and ohmic dissipation is small. Thus, the corresponding terms are neglected. We further assume that the tachocline lies completely inside the radiative zone. Given the very high turbulent viscosity in the convection zone, we can safely assume that the convection zone rotation profile acts like an axisymmetric rigid outer boundary on the tachocline. We use Eq. (1.6) as the profile at the base of the convection zone. As the tachocline is lying in the radiative zone values of diffusivities in the tachocline will be the microscopic ones (Stix & Skaley 1990) or just higher (Rüdiger & Pipin 2001). This may not be computationally possible but we will try to drive the diffusivities as low as possible in our simulations. As mentioned in the previous section a host of authors including Garaud (2001) and Brun & Zahn (2006) tried to drive the diffusivities as low as possible with a conviction that diffusivities in the tachocline are closer to the microscopic values than the turbulent ones. The diffusivities used in this work are the lowest achieved yet. This is remarkable as Brun & Zahn (2006) used a parallel code running on an efficient pc cluster whereas the code used here is merely a serial code.

1.5.2 The Numerical Code

The equations described above are solved using the spectral code developed by Hollerbach (2000). The code is designed for spherical shell. In order to solve the equations in the most efficient manner, it decomposes both velocity and magnetic fields in it toroidal and poloidal components as,

$$\begin{aligned} \boldsymbol{u} &= \nabla \times (e\hat{\boldsymbol{r}}) + \nabla \times \nabla \times (f\hat{\boldsymbol{r}}), && (1.23)\\ \boldsymbol{B} &= \nabla \times (g\hat{\boldsymbol{r}}) + \nabla \times \nabla \times (h\hat{\boldsymbol{r}}). && (1.24) \end{aligned}$$

where $\hat{r}$ is the unit vector in radial direction in the spherical co-ordinates.

These potentials are further expanded into functions of the spherical co-ordinates. A typical expansion, like the one shown in Eq. (1.25) consists of Chebyshev polynomials depending on radius and spherical harmonics in co-latitude. The code facilitates separate resolution for each spherical coordinates thus revealing fine structures without compromising much of speed. Further, choice of Chebyshev polynomials for the radial modes ensures fine resolution in the boundary layer.

$$e(r,\theta,\phi,t) = \sum_m \sum_l \sum_k e_{klm}(t) T_k(x) P_l^{|m|}(\cos\theta) e^{im\phi}, \qquad (1.25)$$

where k, l and m are radial, co-latitudinal and azimuthal wave-numbers, $T_k(x)$ are the Chebyshev polynomials of degree k with x being a function of radius (for details: see Appendix B) and $P_l^{|m|}(\cos\theta)$ are the associated Legendre polynomials of degree (l, m). The non-linear force terms in the Eq. (1.18) are computed in the real space whereas potentials are advanced by second-order Runge-Kutta method in the spectral space. In the various computational setups explored in this work, not all of these components in the sum may be used. As radial, latitudinal and azimuthal modes are separated from each other, the spectral space resolution for each of these types can be chosen independently depending on the problem at hand. As an example, in the simulations regarding tachocline formation, as axisymmetry is assumed, the resolution in the azimuthal modes can be reduced significantly or while analysing stability for simple latitudinal rotation (Chap. 3), one can get away with minimal resolution in the radial modes. In principle, one can go even a step further and trim the actual code to avoid any unnecessary steps, but the performance of the code as compared to the former method (reducing the resolution) is not drastically improved.

The curling of the velocity and magnetic fields in the code in order to get the toroidal and poloidal components separately, is particularly useful as it automatically takes care of the gradient terms in the Eq. (1.18), improving the efficiency of the code. To improve the efficiency further, the temperature equation assumes a standard background temperature profile $T_0(r)$ and the numerical code only evolves the perturbations Θ from this profile. Thus,

$$T = T_0(r) + \Theta(r, \theta, \phi, t). \tag{1.26}$$

The normalized background solar temperature profile given by Eq. (1.27), is chosen as solution to the equation $\Delta T_0 = 0$;

$$T_0 = \frac{R_{\text{in}}}{R_{\text{out}} - R_{\text{in}}} \left(\frac{R_{\text{out}}}{r} - 1 \right). \tag{1.27}$$

Θ is decomposed in the same way as e in the Eq. (1.25). As the temperature profile is normalised with the temperature at the inner boundary, T_0 is dimensionless. Further, as the code requires only the temperature differences rather than absolute temperature, before normalisation, one can subtract the temperature at the outer boundary from the temperature profile. Thus, although the equation gives an impression that the temperature is zero at the outer boundary, physically it only implies that the temperature is lowest at the outer boundary.

Similar to the temperature, normalization also needs to be applied to the other physical variables. The length is scaled by R_{out}, time by the magnetic diffusion time, $\tau_{\text{diff}} = R_{\text{out}}^2/\eta$, velocity by η/R_{out}, and the magnetic field is represented in the form of Lundquist number (S),

$$\mathrm{S} = \frac{B_0 R_{\text{out}}}{\sqrt{\mu_0 \rho_0}\, \eta}. \tag{1.28}$$

This reduces the equations to very few free parameters, namely R_{out}, R_{in}, S, magnetic Reynolds number (Rm), magnetic Prandtl number (Pm) and magnetic Rayleigh number $\tilde{\mathrm{Ra}}$. The last three are defined as,

$$\mathrm{Rm} = \frac{R_{\text{out}}^2 \Omega_{\text{eq}}}{\eta} = \frac{R_{\text{out}} u_{\text{rot}}}{\eta}, \tag{1.29}$$

$$\mathrm{Pm} = \frac{\nu}{\eta}, \tag{1.30}$$

$$\tilde{\mathrm{Ra}} = \frac{g \alpha \Delta T R_{\text{out}}^3}{\eta^2}. \tag{1.31}$$

α is the coefficient of volume expansion for the fluid, g the average gravitational acceleration and ΔT the absolute difference between temperatures at the two boundaries. As R_{out} and Ω_{eq} are fairly well known in the solar case, Rm acts as a measure of magnetic diffusivity. In the solar case, assuming that the diffusivities take microscopic values, these parameters roughly take the values $\text{Rm} = 5 \times 10^{12}$ and $\text{Pm} = 0.005$ (Stix & Skaley 1990). If the tachocline is weakly turbulent, these values of the parameters will be lower accordingly. The magnetic field will be directly calibrated as,

$$B_0 = \frac{\text{S}}{\text{Rm}} \times \sqrt{\mu_0 \rho} R_{\text{out}} \Omega = \frac{\text{S}}{\text{Rm}} \times 700 \text{ kG} \tag{1.32}$$

With these scalings, Eqs. (1.18), (1.19), (1.22) take the form

$$\begin{aligned} \text{Rm}\frac{\partial \boldsymbol{u}}{\partial t} &= -\text{Rm}^2(\boldsymbol{u} \cdot \nabla)\boldsymbol{u} + \text{PmRm}\Delta \boldsymbol{u} + \text{S}^2(\nabla \times \boldsymbol{B}) \times \boldsymbol{B} + \tilde{\text{R}}\text{a}\Theta \boldsymbol{r} - K\nabla P, && (1.33) \\ \frac{\partial \boldsymbol{B}}{\partial t} &= \text{Rm}\nabla \times (\boldsymbol{u} \times \boldsymbol{B}) + \Delta \boldsymbol{B}, && (1.34) \\ \frac{\partial \Theta}{\partial t} &= -\text{Rm}\boldsymbol{u} \cdot \nabla(\Theta + T_0) + \frac{\text{Pm}}{\text{Pr}}\Delta\Theta, && (1.35) \end{aligned}$$

where Θ is the temperature perturbation and $\text{Pr} = \nu/\chi$ is the Prandtl number using the thermal diffusivity χ. The $\boldsymbol{u}$ and $\boldsymbol{B}$ in the equations above are normalised to unity. As explained above, the pressure term in the Eq. (1.33) will drop out after curling, thus, the constant K in that term is not discussed explicitly. As the limits of simulation domain, boundary conditions and the initial conditions for the simulations are varied for different setups, they are discussed alongwith with description of various setups.

With this much acquaintance with the background of the solar tachocline problem, let us proceed to the examination of the issue of tachocline formation in detail.

Chapter 2

Formation of the Solar Tachocline

The discovery of a very sharp shear layer at the base of the solar convection zone, i.e. tachocline, in the late 80's suggested radical reforms were needed in our understanding of the Sun. In the last 15 years, many theories have been developed to explain the existence of such a thin layer. Amongst them, the MHD models have been more successful than the hydrodynamic ones and this work is also an improvement on an existing MHD model. Yet, to appreciate the advantages of MHD models, one has to start with the hydrodynamic models first.

2.1 Turbulent Tachocline Models

The main characteristic of the solar differential rotation that any model will have to explain is the transition layer at the base of the convection zone. Assuming it is not merely a temporary feature, it is a good approximation to consider its dynamic and hydrostatic structure to be in a steady state. The observed differential rotation in the tachocline can therefore be regarded as the result of a subtle dynamic equilibrium between various angular momentum transporting processes.

A first model for this shear layer was proposed by Spiegel & Zahn (1992). They were also the ones to coin the term "tachocline". The model is based on the assumption that the Sun is an axisymmetric sphere and only axisymmetric flow fields are considered. The viscosity in the tachocline is assumed to be much smaller than the turbulent value. The resultant flow is termed as heliostrophic. After evolving the hydrodynamic equations, however, it was realized that in absence of turbulent viscosity, the wind stress exerted on the radiative interior would force the tachocline to penetrate at least half-way to the solar center. The situation does not improve much when weak isotropic horizontal turbulence is included. The picture is drastically altered if we allow dynamic interaction between strongly anisotropic turbulence and large-scale advection.

Elliott (1997) presented a time series evolution of the Spiegel & Zahn (1992) model, using numerical simulations. He showed that in absence of anisotropic turbulence, the tachocline would be as thick as $0.1R$ in the equatorial region and even thicker in the polar region. Imposing an anisotropic turbulence, the spreading of the tachocline was reduced to $0.05R$ in the equatorial region and $0.1R$ in the polar region. He also tried to explain the observed sound speed anomaly in the tachocline (see Figure 1.1), using turbulent helium mixing in the tachocline region. Miesch (2003) repeated the numerical simulations for a thin shell 3D geometry. An artificial lower boundary was imposed on the thin shell. This configuration with high viscosity was chosen so as to produce a thin tachocline, in agreement with Spiegel & Zahn (1992), but the model was inadequate to explain the uniform rotation rate in the solar interior.

The hydrodynamic models could not strengthen their case, as soon Rüdiger & Kitchatinov (1997) and Gough & McIntyre (1998) showed that the strong restriction of the turbulent motions to spherical shells by background stratification in the radiative zone leads to Reynolds stresses that would drive the system away from rather than towards uniform rotation. Further, the assumption of a turbulent tachocline is not supported by the hydrodynamic stability analysis of the tachocline. Yet, the notion of a turbulent tachocline was used by other authors in a different form. As shown below, some authors introduced a MHD turbulence in order to explain the tachocline.

The primary argument used in case of MHD turbulence is that the tachocline is dynamically coupled with the convection zone rather than the radiative interior. The convection cells from the convection zone overshoot in the tachocline and are the primary drivers of the meridional flow in the region. For this, it is necessary that the magnetic diffusivity in the region is 10^9 cm^2/s or higher. This value is about 6 orders higher than the microscopic value of η assumed to be prevalent in the solar interior. The dynamo field actively controls the tachocline dynamics in this case. The positive side of this approach is that the essential simulation parameters like Reynolds number are much smaller and thus, in the computational range. On the flip side, the diffusive timescales also get smaller and are of the order of the solar cycle i.e. 22 years. This is known as "fast" solar tachocline. The model is primarily advocated by Forgács-Dajka & Petrovay (2002) and Petrovay (2003). They impose a 22-year oscillatory magnetic field on the outer boundary and study dynamic changes in the tachocline for various imposed stream functions. The model is effective in confining the thickness of the tachocline to its small observed values. It also predicts that the tachocline thickness would be larger for polar latitudes. For all its triumphs, the model can be of hardly any use for predicting long term formation history or evolution of the tachocline. The simulations of the fast tachocline are limited to time series of a few solar cycles which are way too short as compared to the solar life. Secondly, the analytical models show that a thin ($\leq 0.05R$), turbulent tachocline would require a poloidal field of 1kGauss or more which looks implausible. Further, there is no direct evidence that the tachocline, which mostly lies in the stably stratified radiative interior at least for lower latitudes, can be dynamically coupled to the convection zone.

We thus come to the most successful of the models which couple the tachocline to the radiative interior and employ a large-scale relic poloidal magnetic field to aid the tachocline formation.

2.2 Models with Relic Poloidal Field

The idea of a large scale weak poloidal magnetic field was first introduced by Rüdiger & Kitchatinov (1997). As explained earlier, if there is a relic poloidal magnetic field in the tachocline, it will be predominantly dipolar. An axisymmetric dipolar magnetic field given by

$$\boldsymbol{B} = \left(\frac{1}{r^2 \sin\theta} \frac{\partial A}{\partial \theta}, -\frac{1}{r \sin\theta} \frac{\partial A}{\partial r}, 0 \right), \tag{2.1}$$

with the generating function

$$A = \mathrm{S}_0 r^2 \left(1 - \frac{r}{R_{\mathrm{out}}} \right) \sin^2\theta \tag{2.2}$$

was chosen as the initial field configuration. S_0 is the Lundquist number (S) corresponding to the initial condition. The equilibrium solutions for the axisymmetric MHD equations were searched; but the meridional flow was ignored. The analytical results from simple shear flow model suggested that the thickness of the tachocline should be roughly

$$\frac{\delta R}{R} \propto \mathrm{Ha}^{-1/2}, \tag{2.3}$$

with the Hartmann number

$$\mathrm{Ha} = \frac{\mathrm{S}}{\sqrt{\mathrm{Pm}}} = \frac{B_0 R}{\sqrt{\mu_0 \rho \nu \eta}}. \tag{2.4}$$

This means, for a solar like tachocline ($\leq 0.05R$), a Hartmann number of $O(10^3)$ is required, assuming microscopic magnetic diffusivity. Further, the induced toroidal field winds itself to a converged value independent of the initial poloidal field amplitude (B_0). Their ratio is given by

$$\frac{B_\phi}{B_0} \simeq \frac{\Omega_0 R}{B_0} \left(\frac{\mu_0 \rho \nu}{\eta} \right)^{1/2} \simeq \frac{\mathrm{Rm}}{\mathrm{Ha}}. \tag{2.5}$$

With $\eta \simeq 10^3$ cm^2/s (Stix & Skaley 1990) as a rough estimate for the solar diffusivity in the tachocline, one finds $\mathrm{Rm} \simeq 5 \times 10^{12}$ for the solar transition region between the convection zone and the radiative interior. With this configuration and a given rotation profile at the outer boundary various amplitudes of the poloidal fields were chosen. The results are graphically shown in Figure 2.1. A thin tachocline was achieved for a B_0 of 0.1mG. The toroidal field was always found to be of the order of 200G in all these simulations. A special feature in these results is a polar cap which shows a thick tachocline in the polar region. As we will show later, this feature no longer exists when meridional flow is included. Gough & McIntyre (1998) independently arrived at the same conclusion that the large scale poloidal magnetic fields are inevitable in the tachocline formation models. In this work they pointed out that a strong non-linear coupling between a thermally driven meridional flow and a large scale interior magnetic field is essential to the formation of the tachocline. The analytical expressions derived for the thickness as well as the toroidal field matched fairly well with observations and solar dynamo models.

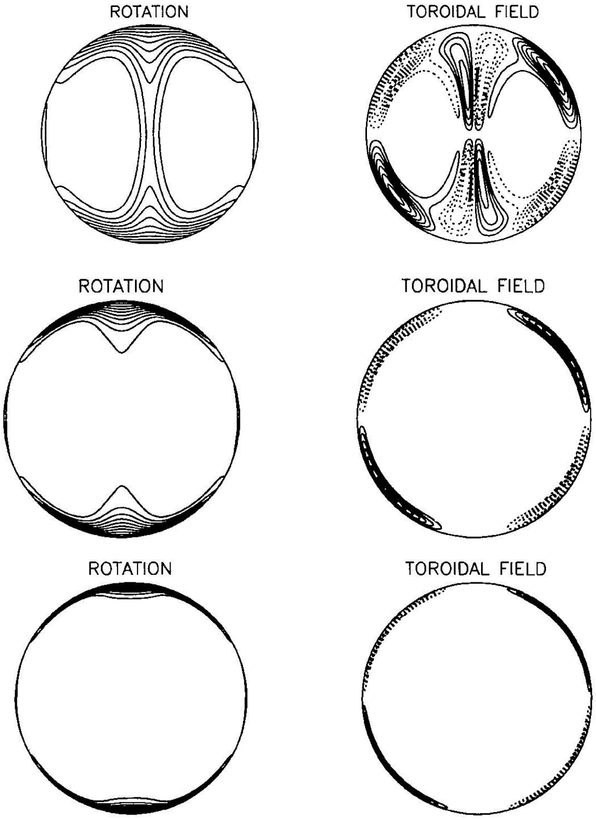

Figure 2.1: Contour lines of both angular velocity (left panels) and toroidal field (right panels) for a large scale dipolar internal magnetic field as given in Rüdiger & Kitchatinov (1997). In the right panels, different line styles indicate different signs of the toroidal magnetic field. The field strengths are 10^{-5} G (top), 10^{-4} G (middle) and 10^{-3} G (bottom).

MacGregor & Charbonneau (1999) performed numerical simulations for two different magnetic field profiles for various Rm. An initial setup of a stable radiative interior threaded by a poloidal magnetic field was used to find equilibrium solutions for the MHD equations. Rotation profile on the outer boundary of the simulation domain, which coincides with the top of radiative zone, was rigidly fixed to

$$\Omega_{\mathrm{out}} = \Omega_0 \left(1 - 0.1264\cos^2\theta - 0.1591\cos^4\theta\right), \qquad (2.6)$$

where θ is the co-latitude[1]. The Reynolds numbers in the simulations were defined with the Alfvén velocity instead of the rotational velocity as in Eq. (1.29). Figure 2.2 summarizes their results. In both rows, the leftmost panel shows the poloidal field profile. In the upper row, the poloidal field crosses the outer boundary of the radiative interior and is dynamically coupled with the convection zone above. On the other hand, in the lower row,

---

[1] MacGregor & Charbonneau (1999) give a positive sign for the $\cos^4\theta$ term which appears to be a typographic error. The negative sign used here is essential for a solar-like differential rotation.

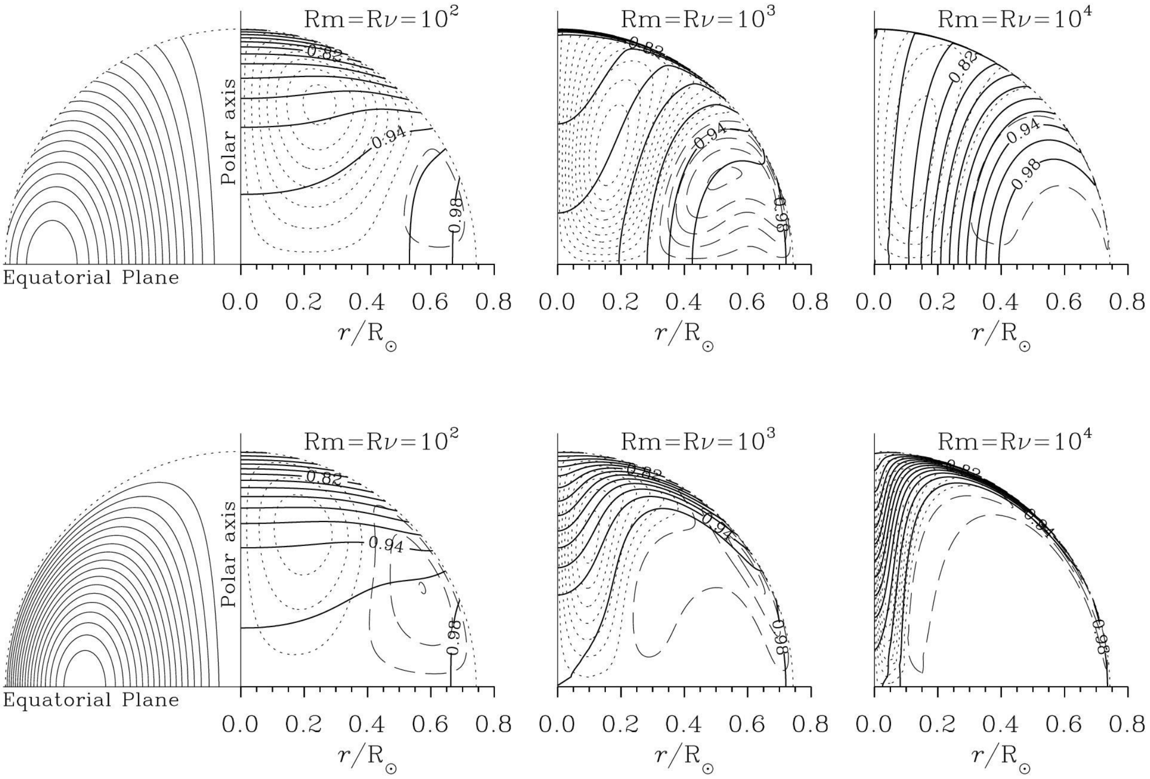

Figure 2.2: Sequences of steady state solutions for two different configurations for increasing Rm as given in MacGregor & Charbonneau (1999). The leftmost panel shows the poloidal field configuration used to generate each sequence. In the other panels, the solid lines are iso-rotation contours, normalized to the surface equatorial rotation rate. Dashed (dotted) lines are contours of constant positive (negative) toroidal field strength.

the poloidal field is confined to the radiative interior. A vacuum boundary condition is used for the magnetic field. In the panels except the leftmost ones in each row, in each row, the solid lines represent contours of constant angular velocity, normalized to the equatorial rotation rate at the outer boundary. The dashed and dotted lines are contours of constant positive and negative toroidal magnetic field strengths respectively. From the plots, it is clear that at very low Rm, representing small magnetic fields, the magnetic field is unable to alter the rotation, and the resulting rotation profile looks very similar to the non-magnetic case. In the upper panel, where the poloidal field is coupled to the convection zone, if the magnetic field strength is very high, the contour lines of constant Ω follow the poloidal magnetic field lines throughout the interior, in accordance with the theorem of Ferraro (1937). Thus no tachocline is formed. In the lower panels, for high magnetic field, the tachocline does get formed at lower latitudes, with uniform rotation throughout interior, but the rotation axis itself seems to be unaffected by the magnetic field. MacGregor & Charbonneau (1999) concluded that the poloidal field should be confined to the radiative

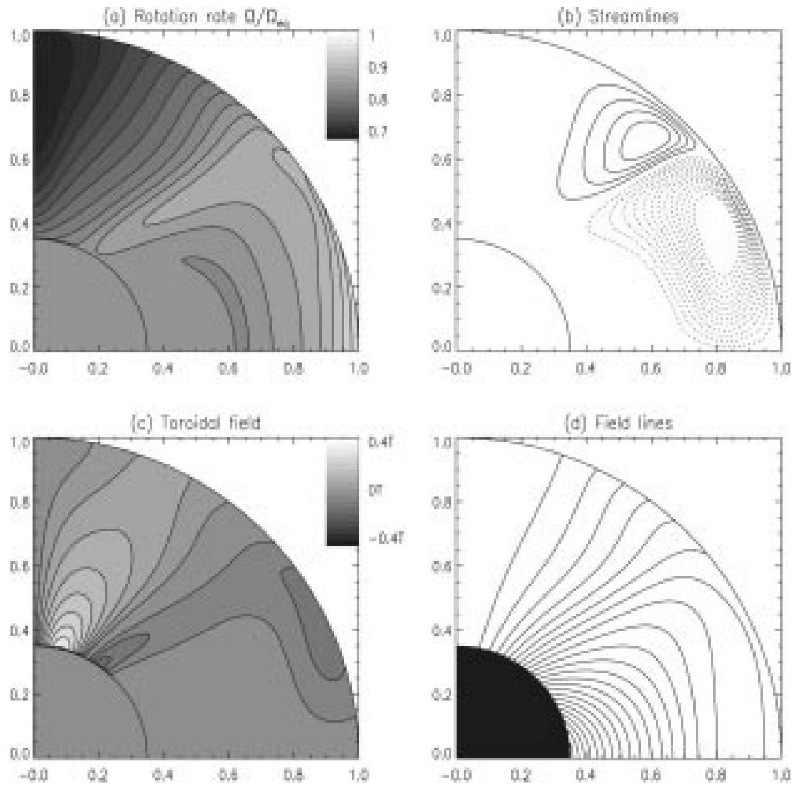

Figure 2.3: Simulation results by Garaud (2001) for an intermediate magnetic field strength, with iso-rotation contours (top left), streamlines (top right), toroidal (bottom left) and poloidal (bottom right) magnetic field plotted in the four panels. In the left panels, darker shades represent smaller values. In panel (b), solid (dotted) lines show anti-clockwise (clockwise) motions.

zone for the formation of the tachocline. Using boundary layer analysis and assuming standard constants like $\rho = 1$ gm/cm^3 and microscopic magnetic diffusivity, they got

$$\frac{h}{R_{\mathrm{out}}} \approx 3 \times 10^{-3} B_0^{-1/3}, \qquad (2.7)$$

$$B_\phi \approx 2 \times 10^{6} B_0^{1/3}. \qquad (2.8)$$

Assuming the thickness of the solar tachocline (h/R_{out}) as 5%, the required strength of B_0 was calculated as roughly 0.2 mG. This leads to a toroidal field strength of 100kG, as required by the popular dynamo models.

The next major improvement on the tachocline models was presented by Garaud (2001). The meridional flows were introduced through the judicious choice of boundary conditions on the flow at the top. Yet the simulations could not perform a time evolution of the system and only equilibrium solutions were found. As ν and η were introduced in the equation, the poloidal field would diffuse on short timescales, for computationally achievable small Reynolds numbers. To avoid this, a constant regeneration of poloidal field at the far placed inner boundary ($0.35R$) was introduced. The system was assumed to be axisymmetric and the rigid boundary conditions on the flow at the inner as well as the outer boundary ($0.7R$) ensured that the stream flows are restricted to the simulation domain.

After the inclusion of the meridional flow, the "Taylor-Proudman" flow patterns were found to be the stable solution in the non-magnetic case. The inclusion of a weak magnetic field was not able to alter this stable solution much. In accordance with MacGregor & Charbonneau (1999), the iso-rotation contours followed Ferraro's law for high magnetic field. However, for an intermediate value, a tachocline like structure could be seen at the low latitude. Again the angular velocity along the rotation axis was least affected (see Figure 2.3). As seen in the last panel, the poloidal field lines cross the outer boundary and are coupled with the convection zone. The uniform rotation in the inner parts of the radiative zone and the shape of the tachocline become even more prominent when the magnetic Reynolds number was increased by a factor of 4 to 16000. Even though the model was successful in showing the importance of the meridional circulation to the tachocline formation, it was found unsatisfactory on other issues, in particular the fact that the poloidal field was coupled to the convection zone and only equilibrium solutions were obtained instead of a full time series evolution.

In short, there is a need for a more comprehensive study of the tachocline. The model should be able to evolve itself in time to study tachocline evolution, should include meridional flow as shown by Garaud (2001) and yet, at the same time be consistent with observations. A model complying with these needs is presented below.

2.3 The Chosen Model

Starting from the MHD equations described by Eqs. (1.33), (1.34), we evolve an axisymmetric fluid sphere. As discussed earlier, the radiative zone of the Sun has a very small (microscopic) value of η. This means the diffusion time is very large. For a dipolar field, the diffusion time becomes comparable or even larger than the solar life time, this implies that the dipolar component of the poloidal field may decrease by only a factor of three or smaller whereas the stable tachocline solution is reached in a much shorter timescale and in this period the toroidal magnetic field is amplified by few orders of magnitude. Thus, it would be a good approximation to keep the poloidal dipolar field as time invariant. The Eq. (1.34) can be reduced to

$$\frac{\partial B_\phi}{\partial t} = [\nabla \times (\boldsymbol{u} \times \boldsymbol{B})]_\phi + [\Delta \boldsymbol{B}]_\phi. \tag{2.9}$$

This approximation is essential for the simulation purposes as the real solar magnetic Reynolds number ($O(10^{12})$) is not achievable for current computational resources. We will use values of Rm not exceeding 10^5. This numerically constrained choice of Rm implies very high values of η and ν in the simulations.

It is assumed that the tachocline lies completely inside the radiative zone. Although it would be better to include density stratification for more realistic simulations, the test runs with even moderate density gradients proved computationally too expensive. The outer radius of the computational domain is taken as $R_{\text{out}} = 0.75R$ and the inner radius as $R_{\text{in}} = 0.1R$. Due to numerical constraints, the study was restricted to spherical shells instead of a complete sphere. The size of the remaining inner hole was found to have a negligible effect on the results.

It is assumed that the rotation profile in the convection zone is independent of the dynamics in the radiative zone and can be prescribed as a boundary condition. It is further assumed that any physical phenomenon occurring in the convection zone, including a dynamo, does not have an effect on the dynamics within the radiative zone and the tachocline. For the first set of simulations, the effect of the temperature gradient and hence buoyancy force on the fluid is also neglected. The equations and results involving a temperature gradient along the radius will be discussed in a later section.

Given the very high turbulent viscosity in the convection zone, it can be safely assumed that the convection zone rotation profile acts like a rigid outer boundary on the tachocline. Therefore, the rotation profile of the angular velocity at the outer boundary is chosen to match the observed rotation profile in the bulk of the convection zone, given by Eq. (2.6) as a rigid boundary condition. Only the axisymmetric modes of the originally three-dimensional spectral code are evolved. The runs typically employ 60 radial Chebyshev (k) modes and 60 latitudinal Legendre (l) modes. It has been verified by additional computations that the results change very little at different resolutions.

The magnetic field used is given in the Eq. (2.1). The generating function is changed to

$$A = \mathrm{S}_0 r^2 \left(1 - \frac{r}{R_{\text{out}}}\right)\left(1 - \frac{R_{\text{in}}}{r}\right) \sin^2\theta. \tag{2.10}$$

This involves the second bracket in order to avoid the magnetic field lines crossing the inner boundary. This will introduce small toroidal currrents near the inner boundary. We eliminate the curl of the poloidal magnetic field, which is dominant only at the inner boundary, by equating it to zero at every time step. A comparison with computations including the full Lorentz force did not show significantly different results.

At the outer boundary, the rotational velocity was maintained rigidly, where as other components adhered to the stress free boundary conditions. At the inner boundary stress-free boundary conditions were used. Vacuum boundary conditions were used for the magnetic field. In short,

$$\text{At} R_{\text{in}} \qquad u_r = 0 \quad \frac{\partial}{\partial r}\left(\frac{u_\theta}{r}\right) = 0 \quad \frac{\partial}{\partial r}\left(\frac{u_\phi}{r}\right) = 0 \tag{2.11}$$

$$\nabla \times \boldsymbol{B} = 0 \tag{2.12}$$

$$\text{At} R_{\text{out}} \qquad u_r = 0 \quad \frac{\partial}{\partial r}\left(\frac{u_\theta}{r}\right) = R_{\text{out}}\Omega_{\text{out}} \quad u_\phi = 0 \tag{2.13}$$

$$\nabla \times \boldsymbol{B} = 0 \tag{2.14}$$

The meridional flow from above (convection zone) is not included in the simulation. However, it will not change the results as it is expected to have very low penetration depth

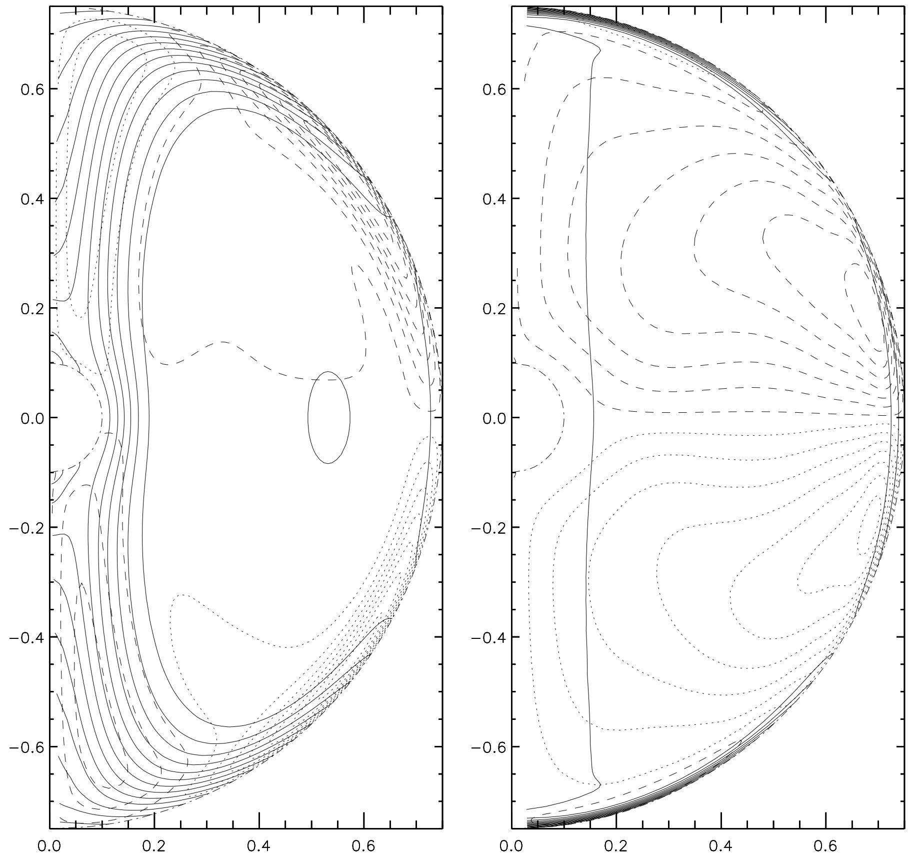

Figure 2.4: Results for the simulations excluding (left) and including (right) the meridional circulation with the magnetic field being confined to the core. The solid lines are the iso-rotation curves, whereas the dashed and the dotted lines represent the contours of the positive and the negative toroidal field strength respectively. The dot-dashed lines indicate the boundaries of the simulation domain. The time-invariant poloidal magnetic field is not shown. $S_0 = 1100$, $\mathrm{Pm} = 1$ and $\mathrm{Rm} = 10^4$.

(Rüdiger et al. 2005) and the model considers only the lower layers of the tachocline which are not turbulent.

2.4 Results

2.4.1 The effect of the meridional flow

Earlier investigations have shown that even a weak poloidal seed field is able to produce a solar-like tachocline. It was found that the region near the rotation axis (i.e. poles) is least affected by the field and the tachocline is thickest in that part. Further, when the poloidal field amplitude is very small, the magnetic field is unable to alter the rotation, and the

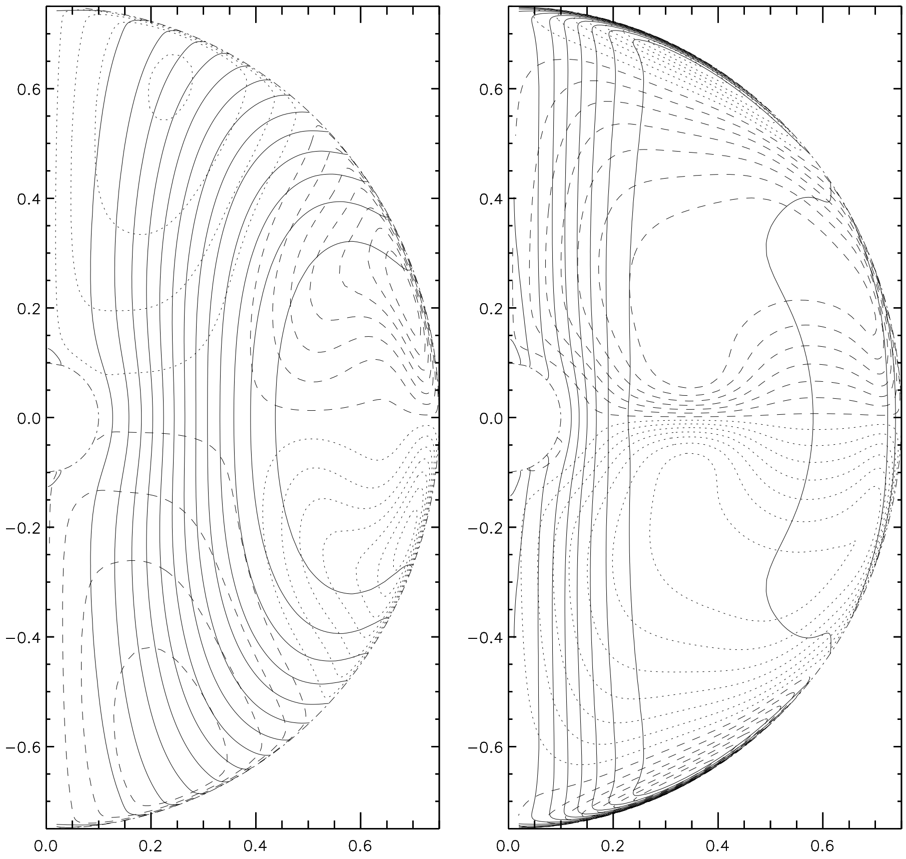

Figure 2.5: Results for the simulations excluding (left) and including (right) the meridional circulation when the magnetic field lines are crossing the outer boundary. The legend is same as Figure 2.4

. Note the thin Ekman layer (tachocline) produced along the outer boundary in the right panel.

resulting rotation profile looks very similar to the non-magnetic case. At the other extreme, if the magnetic field strength is very high, the contour lines of constant Ω follow the poloidal magnetic field lines throughout the interior, in accordance with Ferraro's theorem. A solar-like tachocline is thus impossible in either case. To study the effect of a meridional flow, the same parameter configuration was evolved twice starting from same initial conditions, once excluding meridional flows and then including them. The initial flow pattern was chosen to be a Taylor-Proudman flow, which is known to be hydrodynamically stable.

In these simulations, $\mathrm{Rm} = 10^4$ and $\mathrm{Pm} = 1$ are used. In all the simulations, it was found that the system converges to an equilibrium solution in less than $0.1\tau_{\mathrm{diff}}$. Unless mentioned otherwise, the figures and numerical values throughout this Chapter refer to the final equilibrium solutions. While the simulations without meridional flow concur with most of the key features noted by the previous authors, the simulations including the meridional flow reveal quite new features. The results are best represented by the comparison of the two graphs in the Figure 2.4. The left panel is just a reproduction of the earlier MacGregor & Charbonneau (1999) result, where the magnetic fields are confined to the simulation domain (see rightmost panel on the bottom in the Figure 2.2) and the right panel shows the same model including the meridional circulation. The solid lines are the iso-rotation curves whereas the dashed and the dotted lines represent the contours of the positive and negative toroidal field strengths, respectively. While in the left graph the region along the rotation axis is not affected at all, we see that the inclusion of the meridional circulation changes the picture completely.

In the right side panel, the entire core, including the region near the rotation axis, has achieved nearly uniform rotation. The tachocline is formed near the outer boundary. In contrast with the results ignoring the meridional flow, the tachocline is now thinnest near the pole. In the region near the equator, where the magnetic field influence is smaller, the iso-rotation curves tend to be similar to the characteristic Taylor-Proudman flow. The toroidal magnetic field strength is only 30% of the poloidal magnetic field strength.

MacGregor & Charbonneau (1999), in their paper studied another case, where the poloidal magnetic field is no longer confined to the computational domain and the magnetic field lines are crossing the outer boundary of the simulation domain. It was reported that tachocline cannot form in such a configuration. Recently, Brun & Zahn (2006) argued that any magnetic seed field, confined to the radiative core, will be eventually coupled to the outer convection zone and this configuration is more realistic than the previous one. To test this model of magnetic field, the computational setup was restructured. The magnetic field dipole was chosen much bigger than the computational domain, such that the eye of the field remains inside the domain. Vacuum boundary conditions on the outer boundary allow magnetic field to penetrate easily. In reality, the magnetic field penetrating to the convection zone is distorted by the flows but as the convection zone is outside the computational domain, this effect is ignored in favour of computationally simple ideal dipole field. The results obtained were a stark contrast to the MacGregor & Charbonneau (1999) results. Due to (near) rigid outer convection zone, the Ekman layer is again formed along outer boundary with the characteristics similar to the one formed in the previous configuration (see Figure 2.5). This layer can be identified as the tachocline. Brun & Zahn (2006) also obtained this layer in their simulations with similar configuration. It was argued there that this layer is a transient feature and is destroyed eventually but its presence in the sun at the current solar age cannot be ruled out. One distinct feature of this configuration is the cylindrical pattern formed by iso-rotation contours near the axis of rotation, conforming to the Ferraro's law. As the particular configuration can only produce transient tachocline, the former configuration with simpler setup is used in the future discussion.

For the former configuration, the initial and final states in terms of fractional Ω are shown as functions over radius for various latitudes in the upper panels of Figure 2.6. The upper-left panel in the figure is a characteristic plot for the Taylor-Proudman flow.

Some test simulations were performed with a decaying poloidal magnetic field. During these simulations, it was observed that the magnetic field does form a tachocline during

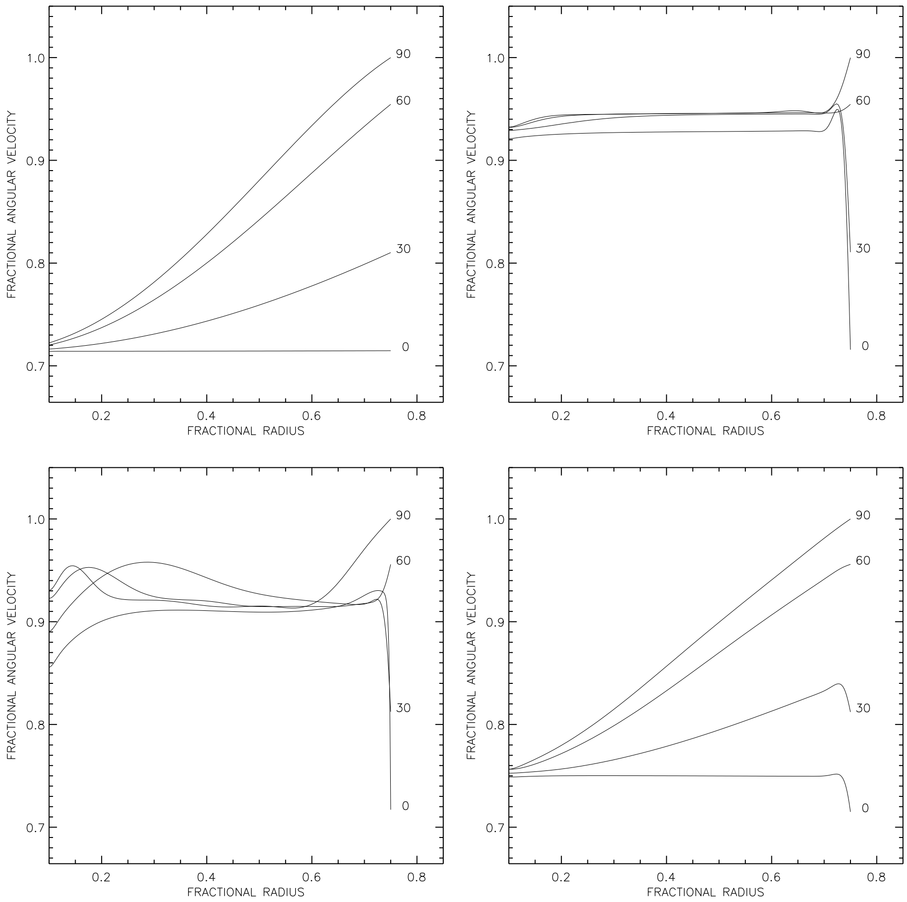

Figure 2.6: Fractional Ω vs. fractional radius plot. The four panels represent the initial configuration (top-left), the equilibrium solution when $B_{\rm pol}$ is constant (top-right) and snapshots at $0.05\tau_{\rm diff}$ (bottom-left) and $0.5\tau_{\rm diff}$ (bottom-right) with decaying $B_{\rm pol}$. Different lines represent Ω at different co-latitudes.

the period up to $\sim 0.05\tau_{\rm diff}$, but as the magnetic field decays gradually due to the high value of η assumed in the simulations, the flows readjust themselves, and the resulting pattern will be the same as the purely hydrodynamic case, i.e. it will approach the Taylor-Proudman flow. The lower-left panel of Figure 2.6 shows the fractional Ω in an intermediate stage at $t = 0.05\tau_{\rm diff}$ for a decaying poloidal magnetic field, keeping the other parameters the same as for the run in Figure 2.6. The effect of forming a tachocline structure by a time-dependent poloidal field is thus very similar to the non-decaying field, but diffusivity reduces the field too early, and the final tachocline state is not achieved. Figure 2.7 shows the evolution of the poloidal magnetic field at three different times. Note how an initially dipolar field changes to predominantly vertical.

In the solar case, if the magnetic diffusivities take microscopic values, the diffusion time scale (50 Gyr) is much larger than the solar age (5 Gyr). Thus, in the Sun, tachocline

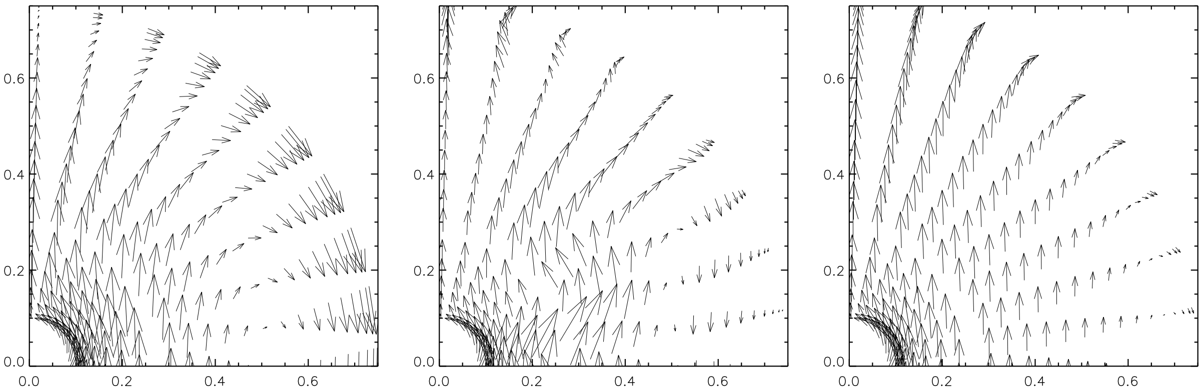

Figure 2.7: Snapshots of $B_{\rm pol}$ in case of a decaying poloidal field at (from left to right) $t = 0$, $0.05\tau_{\rm diff}$, and $0.5\tau_{\rm diff}$. For each snapshot, the length of the arrows is proportional to the amplitude of $B_{\rm pol}$ at each point. The length of the arrows is renormalized in each plot by the corresponding maximum field amplitude. Only every fifth arrow in θ and r is plotted in order to avoid congestion.

can be explained even with the decaying poloidal field. The time scale required for the formation of the tachocline varies directly with viscosity of the flow as the readjustments of the flow patterns can happen faster. Thus, in the real stars with low viscosity and low magnetic diffusivity, the tachocline will be formed early and will diffuse very slowly.

It can be concluded here that the magnetic field is not only important for the formation of the tachocline but also for maintaining it, at least in the case of the high magnetic diffusivity used in these simulations.

2.4.2 Varying the magnetic Prandtl number

Following Kippenhahn & Weigert (1994) and Stix & Skaley (1990), the solar value for the magnetic Prandtl number in the radiative zone is approximately 0.005. Although this value was not achieved, the simulations were performed for various values of Pm in the range of 0.05–1 whereas $\mathrm{Rm} = 10^4$ in all the cases.

In these simulations, it was observed that two cells of meridional flow were formed (see left panel of Figure 2.12). The low-latitude cell was smaller with clockwise (equatorwards) circulation and small radial extent. The other cell was spread throughout the radiative interior with anticlockwise (pole-wards) flow pattern. The maximum amplitudes of the meridional flow is found to be in the horizontal direction near the outer edge. The amplitudes of these flows are plotted in Figure 2.9(left). The horizontal component of the meridional flow (u_θ) generated is about 2% of u_ϕ at higher latitudes and is about 1% for lower latitudes. Similarly, the vertical component of the meridional flow (u_r) is about 0.5%. These ratios are nearly independent of the value of Pm. The radial component of the velocity remains much smaller than the latitudinal component especially for lower values of Pm, as can be seen in Figure 2.8. The figure also shows that strong latitudinal

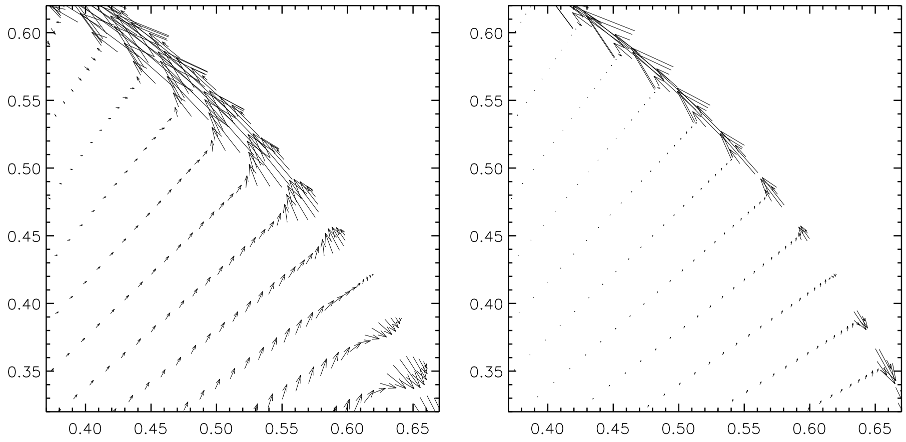

Figure 2.8: Results for the simulations with Pm = 1 (left) and 0.05 (right) showing a small section of the simulation domain with the components of the meridional circulation plotted. The arrow lengths are assigned in the same way as Figure 2.7. Only alternate points in the radial direction are plotted. Note that the area shown is not a complete quadrant but only a magnified region at outer boundary.

flows are expelled closer to the outer boundary for lower values of Pm. This is in line with the expectation as the lower viscosity (i.e. lower Pm) makes the coupling between different horizontal layers less effective thus enhancing the horizontal flow at the expense of the vertical flow. The tachocline, thus formed, is thinner[2] at the pole than at the equator. The thickness of the tachocline at the equator reduces marginally from $0.030R$ to $0.026R$ when Pm is changed from 1 to 0.05, whereas the thickness of the tachocline at the pole decreases considerably. It was also observed that the amplitude of the toroidal magnetic field remains smaller than that of the poloidal field and is almost independent of the choice of Pm.

2.4.3 Varying the magnetic Reynolds number

In this subsection, a constant Pm = 1 is used and Rm is varied. As the solar value of Rm is about 10^{12}, simulations are run for Rm larger than Rm = 10^4. The highest value of Rm in our simulations was 10^5.

In this set of simulations it was again noticed that the relative amplitudes of the meridional flow are nearly independent of the value of Rm as shown in Figure 2.9 (right). The thickness of the tachocline at the equator reduces from $0.030R$ to $0.015R$ when Rm is changed from 10^4 to 10^5, whereas the thickness of the tachocline at the pole goes down from $0.012R$ to $0.003R$. This may appear as drastic change in the tachocline thickness, but eventually tachocline would settle to certain minimum thickness as a Ekman boundary

---

[2] The thickness is defined as the distance between the outer boundary and the radius at which the rotation rate deviates by 1% from the rotation rate deep inside the core.

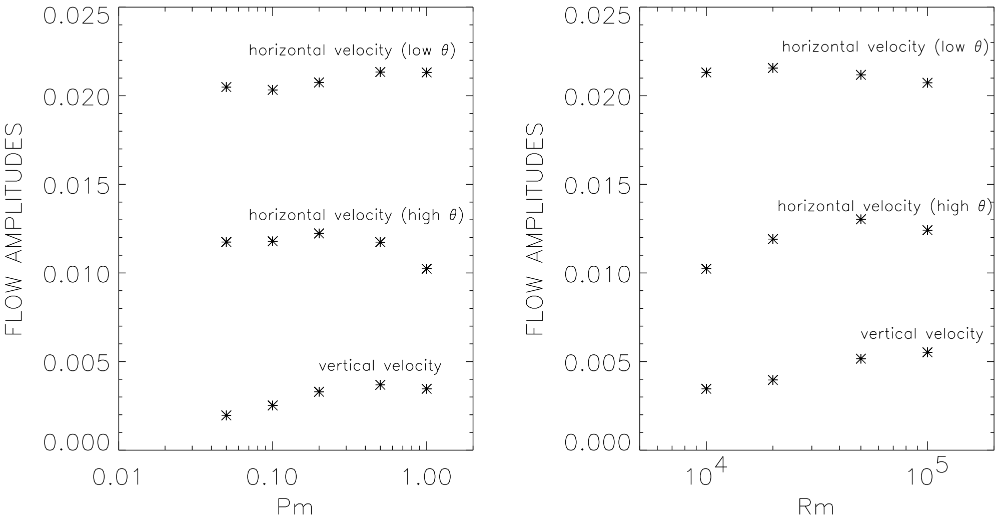

Figure 2.9: The amplitudes of the components of the meridional flow at different co-latitudes (θ), normalized to the rotational velocity at the equator, with varying Pm (left) and Rm (right). The two different data-sets for the horizontal velocity represent velocities in the two different cells produced.

layer. The values of tachocline thickness for Rm less than 10^4 are of little use for scaling as the system is too viscous. The Rm more than 10^5 could not be achieved in the simulations. Thus, the numerical value of this minimum thickness is difficult to estimate at this stage using the estimates for only one order of magnitude change. Correspondingly, the toroidal field (B_ϕ) in the tachocline region increases from $0.3B_0$ to $1.3B_0$.

As the relative meridional circulation amplitudes are independent of Rm, one can expect similar relative amplitudes of the meridional flow in case of the Sun. This would lead to flows up to 30 m/s. As the current heliosesimological techniques cannot measure the meridional flows in the tachocline, existence of such a flow cannot be confirmed or denied. As the Lundquist number increases much slowly than the Rm, both of which depend on the magnetic diffusivity, the physical value of the magnetic field would go down for the high Rm.

2.4.4 Effect on the Lundquist number

It will be worthwhile to place some emphasis on the choice of the poloidal field strength. In the simulations, it was seen that the choice of the amplitude of the seed field value is very critical. A small deviation in that amplitude of magnetic field which produces a solar-like tachocline either makes the iso-rotation curves similar to the non-magnetic case or the curves will comply with Ferraro's theorem, unable to produce a tachocline in both cases. This behavior was also seen in the work of Garaud (2001). At lower values of Pm, we require smaller seed fields as shown in Figure 2.10. The dotted line in the figure shows

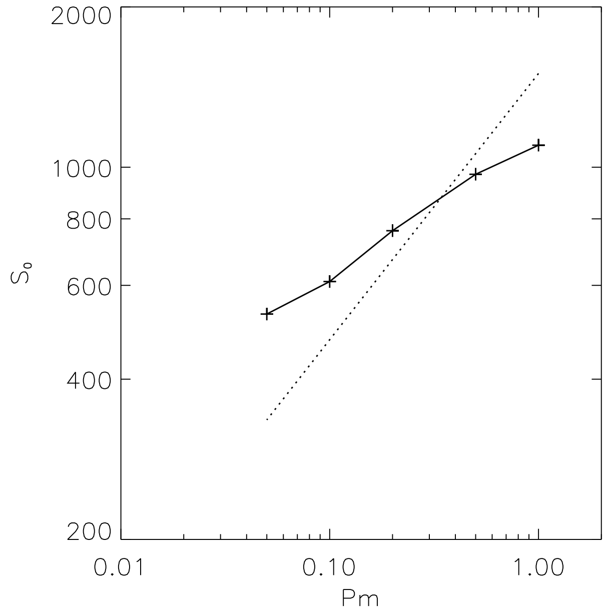

Figure 2.10: Variation of S_0 with varying Pm as a log-log plot, for an approximate tachocline thickness of $0.025R$. The dotted line represents a fixed Ha = 1500.

line for the fixed Hartmann number of 1500. This reference line clearly shows that smaller Hartmann number should be higher for lower values of Pm. The trend observed in this log-log plot is roughly linear and thus, one can express the relation as a power law. When calculated, S_0 varies roughly as $\sqrt[4]{\mathrm{Pm}}$.

Next, when Pm is kept constant at 1 and Rm is varied, one finds that at higher values of Rm, the required values of S_0 are higher (Figure 2.11). The points in this log-log plot show for very high Rm, the power law like extrapolation can be treated as limiting case on the higher side. The actual Lundquist number at the the solar value of Rm would be smaller than or equal to the value obtained by the power-law extrapolation. Adopting similar procedure to the Pm case, one finds that S_0 varies roughly as $\sqrt{\mathrm{Rm}}$.

Combining the two, an empirical law governing the variation of S_0 as a combined function of Pm and Rm can be deduced from these plots as

$$\mathrm{S}_0 \simeq 10\ \mathrm{Rm}^{0.5}\mathrm{Pm}^{0.25}. \tag{2.15}$$

This scaling is the main result of the computations. It means that

$$\frac{B_0}{\sqrt{\mu_0 \rho}} \simeq 10\sqrt[4]{\Omega^2 \nu \eta}, \tag{2.16}$$

which, of course, has the correct dimension of a velocity. The old estimate of Rüdiger & Kitchatinov (1997), without meridional flow, led to the quite different expression $B_0/\sqrt{\mu_0\rho} \simeq$

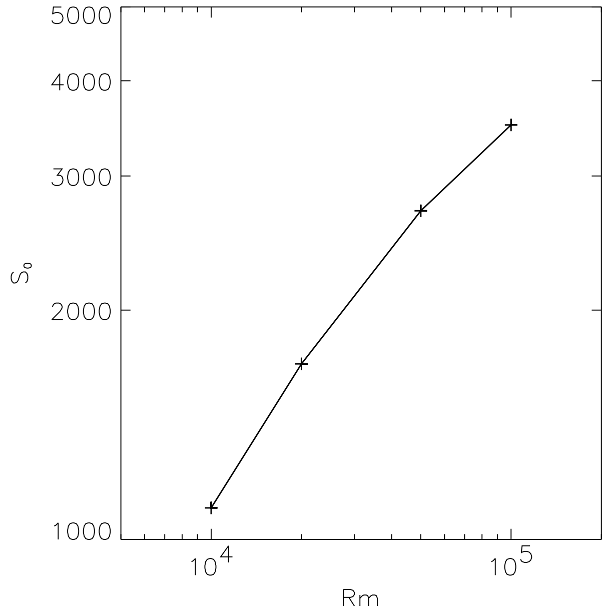

Figure 2.11: Variation of S_0 with varying Rm as a log-log plot, for an approximate tachocline thickness of $0.028R$.

$10^3\sqrt{\nu\eta}/R$ which is a very small value due to the appearance of the radius R. Eq. (2.16) yields

$$\frac{B_0}{\sqrt{\mu_0\rho}} \simeq 0.25\ \mathrm{cm/s}, \tag{2.17}$$

so that a maximum field amplitude of 0.5 Gauss results, for an average density of 0.25 g/cm^3. As the field amplitude is proportional to the square-root of the density, the results will not alter much for a slightly different choice of the average density. This is a much larger value than the milli-Gauss values for models without meridional flow, but it is not an unrealistic number. The scaling relation is now independent of the radius but depends on the square-root of the angular velocity. The dependence on the diffusivities is also weaker. Thus, it can be expected that wide ranges of parameter sets would eventually give similar field amplitudes. The different dependence of the scaling is a result of the readjustment of the meridional flow in the so-called Ekman layer near the outer boundary. Meridional circulations tend to readjust themselves along the magnetic field lines. As the meridional flow amplitudes always maintain a fix ratio with the amplitude of the angular velocity, a faster Ω would result in a faster meridional circulation. This would require a stronger magnetic field to re-align itself and this is reflected in dependence of the field amplitude on the angular velocity. In contrast to the old model, the toroidal field belts now have the same order of magnitude as the poloidal fields.

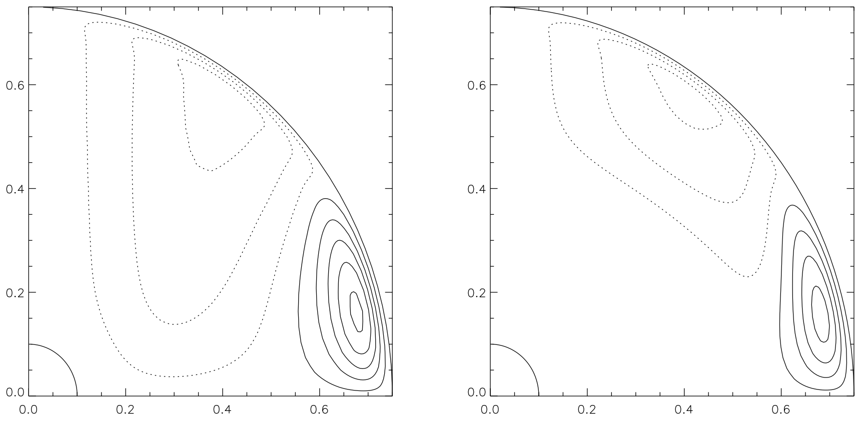

Figure 2.12: Results for the simulations excluding (left) and including (right) buoyancy. The solid and the dotted lines are clockwise and anti-clockwise meridional circulation, respectively. $\tilde{\mathrm{Ra}} = -2 \times 10^7$, $\mathrm{Rm} = 10^4$.

2.4.5 Effect of a temperature gradient

In the simulations discussed in the previous subsections, it was noted that the amplitude of the meridional circulation was nearly independent of the variation of Rm as well as Pm. In the lower latitudinal belt, which is more important for the solar activity, the amplitude of the horizontal velocity u_θ was always around 1% of u_ϕ, and the flow reached very deep layers of the shell. The lithium abundance, however, as discussed earlier, suggests that the meridional circulation should either be very shallow or very slow or both.

Therefore, the model is improved by including a given temperature gradient. The buoyancy force in the Eq. (1.33) now plays a stabilizing role . $\tilde{\mathrm{Ra}}$ is called magnetic Rayleigh number or modified Rayleigh number as ν in the standard definition of the Rayleigh number is replaced by η.

When the model is evolved from the initial state including the temperature equation, it takes much longer (in terms of magnetic diffusion times) to achieve a steady state solution than the simpler cases in the previous sections. This long settling time may again be due to the high diffusivities in the simulations and may not be true in the solar case. To save computational resources, the steady state solutions obtained in the previous sections are used as the initial condition for the simulations involving temperatures. It was verified that the solutions obtained in this manner are identical to the solutions obtained from the same buoyancy runs but starting with the hydrodynamic initial conditions employed in the previous subsections.

$\mathrm{Rm} = 10^4$ and $\mathrm{Pm} = 1$ were used for these sets of simulations. As the simulation domain is of radiative nature, we use negative values of $\tilde{\mathrm{Ra}}$, implying subadiabaticity. Simulations are performed with various values of $\tilde{\mathrm{Ra}}$. The results are presented in Figure 2.12. For the regime when $-\tilde{\mathrm{Ra}}/\mathrm{Rm}^2 \leq 0.01$, the buoyancy is unable to produce any major change

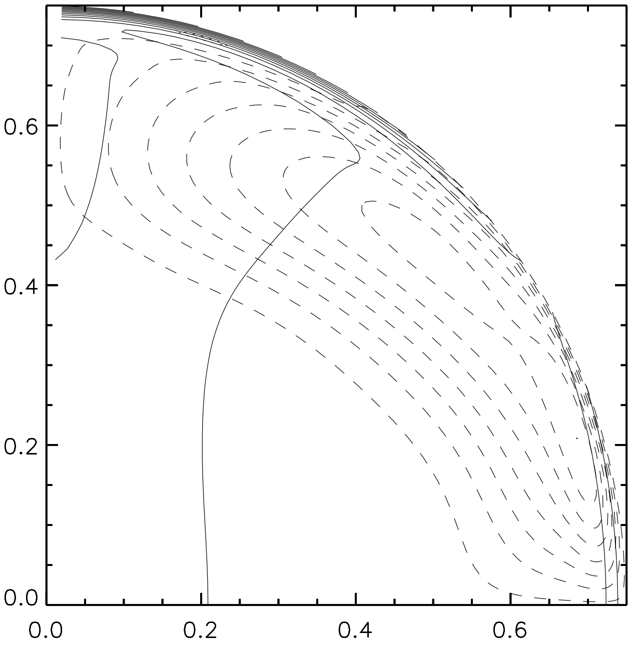

Figure 2.13: The contours of Ω and B_ϕ for one quadrant of the simulation domain, now including the effect of buoyancy. The solid lines are the iso-rotation curves, whereas the dashed and the dotted lines represent the contours of the positive and the negative toroidal field strength respectively. The time-invariant poloidal magnetic field is not shown. $\mathrm{S}_0 = 1100$, $\mathrm{Pm} = 1$, $\tilde{\mathrm{Ra}} = -2 \times 10^7$ and $\mathrm{Rm} = 10^4$.

in any of the velocity components in magnitude or in structure. For more negative $\tilde{\mathrm{Ra}}$, a gradual change in the structure of the meridional circulation is seen[3]. The circulation is then much shallower for higher latitudes (low θ), as desired to explain weak mixing into the interior. This effect is caused by the temperature gradient itself which acts against the vertical flow. It will be worthwhile to note that the equatorial cell shows clockwise circulation in both the figures, which is similar to the motion of the sunspots. However, one cannot pass judgement if this points to some physical connection or is just an coincidence. The magnitude of the flow also decreases but the change is not drastic; see Figure 2.14. For the lower latitudinal belt (high θ), the decrease is relatively stronger and the depth of the circulation is also clearly reduced. There is a marginal increase in the amplification of the toroidal field, probably because the field is not advected through the entire computational domain any longer. The structure of the toroidal field is thus changed as well, and it is shifted towards the outer parts of the shell. On the other hand, the rotation rate at higher latitudes, at large depth in the core, becomes slightly slower than that at the equator. But even this change is marginal and within the observational limits ($|1 - \Omega_{\mathrm{pole}}/\Omega_{\mathrm{equator}}| \leq 3$

---

[3] Note that $-\tilde{\mathrm{Ra}}/\mathrm{Rm}^2 \simeq \boldsymbol{g}/(\Omega^2 R)$, where $\boldsymbol{g}$ is the gravitational term, similar to Eq. (1.18), which absorbs the effects of the temperature gradient.

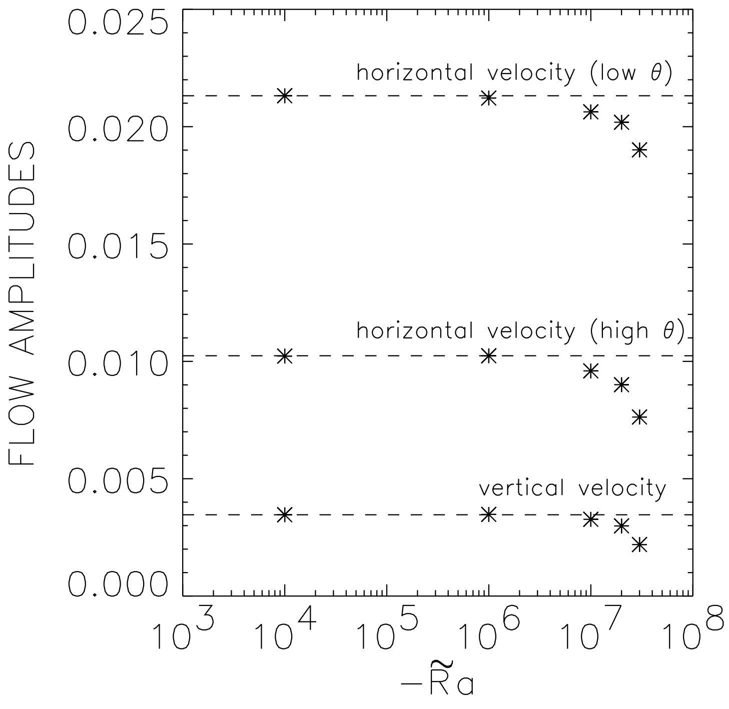

Figure 2.14: Plot of the amplitudes of the components of the meridional flow at different co-latitudes θ, normalized to the rotational velocity at the equator, with varying $\tilde{\mathrm{R}}\mathrm{a}$. The dashed lines represent the corresponding values without buoyancy effect. $\mathrm{Rm} = 10^4$, $\mathrm{Pm} = 1$. The two different data-sets for the horizontal velocity represent velocities in the two different cells produced.

% for $r \leq 0.65R$). Angular velocity and toroidal field belts are shown in Figure 2.13. We expect that even more negative $\tilde{\mathrm{R}}\mathrm{a}$ will further reduce the depth and amplitude of the meridional circulation.

2.5 Discussion

The numerical model presented in this Chapter is the first MHD model for the solar tachocline which self-consistently calculates the meridional circulation in a time-series evolution. The consideration of the meridional flow changes the shape, the structure and the characteristics of the tachocline radically. Hence, the meridional circulation cannot be neglected while modeling the solar tachocline. The thickness of the tachocline in the outer boundary layer near the equator will be determined by the gradient of the magnetic field near the boundary. Simulations show that the tachocline is thinner near the pole. However, it should be noted again that the physical conditions in the solar tachocline are much more complex than this simple model. As seen from the observational estimates, most of the tachocline in the polar regions may lie inside the convection zone and the overshoot layer which has a much higher viscosity (ν) and magnetic diffusivity (η) than their values in the radiative zone. But the simulation domain has uniform values of ν and η, hence it will be only fair to say that only part of the tachocline, which is inside the radiative zone, is simulated in this model. Hence, a definitive conclusion about the thickness of the tachocline in the polar region cannot be drawn from these simulations.

The tachocline is thinner at lower values of Pm as well as at higher values of Rm. The relative meridional circulation amplitude is nearly independent of the variation of Rm and Pm. The amplification of the toroidal magnetic field is naturally larger at higher values of Rm, whereas from Eq. (2.16) it is clear that the poloidal magnetic field amplitude required to produce a solar-like tachocline goes down with decreasing η, i.e. increasing Rm. The magnetic seed field required to produce a solar-like tachocline is a function of Rm as well as Pm. The value of the seed field is expected to be around 1 Gauss in the Sun, for an average density of 1 g/cm^3. Again a significant change is noted from the simulations without meridional flow where even a sub-mGauss field was enough to produce a solar-like tachocline. The scaling of the magnetic field as a function of the rotation rate, ν, and η is given in Eq. (2.16). In the simulations performed, the order of magnitude of the toroidal field was comparable to the poloidal magnetic field was the same but the toroidal field tended to be more and more amplified for higher Reynolds numbers. Thus, for the solar value of Reynolds number, the toroidal magnetic field is expected to be a at least 1–2 orders higher (i.e. 100 Gauss or higher) than the poloidal seed field.

When a stable temperature gradient is introduced across the shell, it makes the meridional circulation shallower as well as weaker for stronger stabilization (more negative Rayleigh number). This can explain why atleast some lithium can still survive till the present solar age even in a weakly turbulent tachocline. The toroidal magnetic field in this case is limited to a belt in the outer parts of the radiative zone.

The relations describing the variation of various parameters such as the Lundquist number required to form a solar-like tachocline, the amplification of the toroidal magnetic field, the amplitude of the meridional circulation etc. are based on the simulation results for a limited range of Rm and Pm. Although the verification of correctness of these relations closer to the solar values of Rm and Pm is desirable, it would be possible only with better computational resources.

The model has successfully shown that a weak poloidal field of strength of about a Gauss can achieve an extremely thin tachocline with a given differential rotation profile and may produce toroidal belts of a few hundred Gauss or higher in the real solar tachocline. As observationally it is known that most of the tachocline – at-least for the lower latitudes – is part of the radiative zone, one can independently constrain maximum strength of the toroidal field belt that can be sustained by the non-turbulent tachocline. This maximum strength of the poloidal fields sustained by the tachocline are also of interest for the models of solar dynamo. Thus, the discussion proceeds to the stability analysis of the tachocline. The next Chapter analyses the linear hydrodynamic stability of the solar tachocline.

Chapter 3

Hydrodynamic Stability

Spiegel & Zahn (1992) used a hydrodynamical tachocline model for its maintainance without the aid of magnetic fields and attempted to explain why it does not spread. However, the fact that an extremely thin tachocline exists in the present Sun and light elements, which are mixed throughout the convection zone, are yet to be found on the solar surface, implies that the tachocline is probably only weakly turbulent i.e. it would be very close to a stable configuration. It is, therefore, important to examine the stability limits of the tachocline.

The problem is adressed in small steps. We first examine the linear hydrodynamic stability of the tachocline for lower non–axisymmetric modes. Subsequently, we hope to include more effects such as addition of toroidal magnetic field and also the introduction of non–linearity.The analysis presented here should serve as an intermediate step to study stability of a simpler configuration.

Ideally, one would be expected to examine stability of the exact tachocline profile obtained in the previous Chapter. However, in order to introduce non–axisymmetric perturbations a very high resolution is needed in the boundary layer. Consequently, the previous configuration cannot be treated in our simplified analysis. Further, we realise that the tachocline obtained there is far from ideal and the real tachocline profile is beyond the computational limits. Thus, in this Chapter we choose a simple radial profile of the tachocline, which qualitatively mimics most of the observed features of the real tachocline. In a later section of this chapter, it is also shown that stability limits of a non–linear radial rotation profile [Eq. 3.12] eventually converge to the stability limits of this simplified profile. It is, of course, conceivable that the stability limit for this profile may vary from that of the one derived earlier. We wish to address this issue in the near future.

3.1 Lower Dimensional Models

The stability problem of a differentially rotating sphere was addressed by various authors from a physical point of view even before the existence of the tachocline in the Sun was known. Watson (1981) first studied shear instability of the differential rotation. The model was restricted to only a spherical surface with no radial extent. The latitudinal rotation profile chosen was

$$\Omega = \Omega_{\rm eq}(1 - \alpha_2 \cos^2\theta). \tag{3.1}$$

Ω is normalized to the equatorial angular velocity and α_2 is non dimensional differential rotation parameter. The equations were solved analytically for a slowly rotating star (i.e. $\Omega^2 r/g \ll 1$). It was further assumed that the fluid is inviscid ($\nu = 0$) and stably stratified (i.e. $\Omega^2/N^2 \ll 1$). The N is called buoyancy (Brunt-Väisälä) frequency,

$$N^2 = -g\left[\frac{1}{\rho_0}\frac{\partial\rho_0}{\partial r} - \frac{1}{c_0^2\rho_0}\frac{\partial p_0}{\partial r}\right]. \tag{3.2}$$

The critical value of differential rotation was obtained as a stability criterion. It was found that the first non-axisymmetric azimuthal mode gets unstable for a differential rotation of $\alpha_2 = 2/7$ or roughly 29% (Watson 1981). For the $m = 2$ mode, the system is found to be stable between $\alpha_2 = -8/7$ and $\alpha_2 = 2/5$. The negative value of α_2 denotes anti-solar differential rotation (pole is rotating faster than equator). As the latter is higher than the stability limit of the $m = 1$ mode, in the solar case, the first non-axisymmetric azimuthal mode turns out to be the most important here. In short, Watson concluded that a differentially rotating star is stable if,

$$\frac{5}{7} \le \frac{\Omega_{\rm pole}}{\Omega_{\rm equator}} \le 2.14. \tag{3.3}$$

Dziembowski & Kosovichev (1987) extend the analysis to a rotation profile containing an additional α_4 term as given by Eq. (1.6). The analytical solutions indicated that the necessary condition for instability is

$$5\alpha_2 + 9\alpha_4 > 1. \tag{3.4}$$

The equation would effectively mean that the tachocline cannot be unstable for $\alpha_2 < 0.2$ in the absence of α_4. If $\alpha_4 > 0$, then the critical combined differential rotation ($\alpha_2 + \alpha_4$) should be above 11% or higher depending on the choice of the two parameters. The sufficient condition showed that the tachocline is likely to get unstable for a combination of α_2 and α_4 at half of the observed value. Charbonneau et al. (1999b) tested the results of Dziembowski & Kosovichev (1987) for a range of parameters including different depths from the solar surface. Instead of choosing a fixed value of differential rotation parameters, they used the helioseismological data available to them to adopt suitable values of α_2 and α_4 at various values of fractional solar radii. Their results confirmed that $m = 1$ is the most important mode for the instability and also the earlier result that when a combination of α_2 and α_4 is used, the differential rotation can get unstable for much less than the tachocline values inferred from the helioseismology.

Garaud (2001) investigated the weakly non-linear behavior of this horizontal instability and found the over-critical system developing into a marginal state very close to the observed rotational profile. In a step towards the three-dimensional stability of the tachocline, Dikpati & Gilman (2001) studied the two-dimensional system allowing for deformations in the third – the radial – dimension. As a result, the critical differential rotation for instability was reduced to 11% in the overshoot part of the tachocline.

With all the lower dimensional models indicating the solar tachocline to be unstable, the premise of coupling of the tachocline with the radiative zone is challenged. Tachocline is the layer where latitudinal and radial shears meet. Thus, radial gradients should not be ignored in the stability analysis of the tachocline and the stability of the full three-dimensional rotation profile needs to be investigated. Although it is very reasonable to assume that radial flows will be weak, the variation of the latitudinal differential rotation with radius across weakly coupled spherical layers could provide different results for the stability of the tachocline.

3.2 The Model

The rotational profile depends on both latitude and radius in this study. Between the inner and outer radius of the tachocline, $R_{\text{in}} = 0.65$ and $R_{\text{out}} = 0.7$, respectively, the angular velocity is defined by,

$$\Omega(r,\theta) = \Omega_{\text{eq}}\left[1 - \alpha_2 \cos^2\theta - \alpha_2 \left(\frac{1}{4} - \cos^2\theta\right) \frac{R_{\text{out}} - r}{R_{\text{out}} - R_{\text{in}}}\right], \tag{3.5}$$

where θ denotes the colatitude in the spherical shell, r the radial coordinate, and Ω_{eq} the equatorial angular velocity. The profile implies that the rotation velocity at the inner boundary of the computational domain, $r = R_{\text{in}}$, is the one at $\theta = 60°$ (or 30° heliographic latitude). This appears to be a valid assumption in agreement with various helioseismological inversions (recently e.g. Schou et al. (2002)), whereas core rotation may be adopted at larger latitudes higher up in the convection zone. The formation of the tachocline rotation profile is supposed to be caused both by rotating convection on top of it and by reduction of differential rotation by magnetic fields in the solar core at the bottom. As shown in the previous Chapter, such a profile causes a meridional circulation reaching steady-state in competition with the aforementioned (or other tachocline-forming) effects. In our linear analysis, this flow has no effect on the stability of the non-axisymmetric modes investigated in this Chapter.

The incompressible, viscous Navier-Stokes equation is employed and the problem is linearized. The axisymmetric background rotation $\boldsymbol{U}$ can then be separated from the non-axisymmetric flow $\boldsymbol{u}$. The latter is evolved by numerical computations. The linearized form of the Eq. (1.33) reads

$$\frac{\partial \boldsymbol{u}}{\partial t} = \boldsymbol{u} \times \nabla \times \boldsymbol{U} + \boldsymbol{U} \times \nabla \times \boldsymbol{u} - \nabla P - \nabla(\boldsymbol{u} \cdot \boldsymbol{U}) + \triangle \boldsymbol{u}, \tag{3.6}$$

and the continuity equation $\nabla \cdot \boldsymbol{u} = 0$ holds. When the problem is linearized, the subcritical configurations give exponentially decaying solutions and supercritical configurations give exponentially growing solutions. In order to find the critical differential rotation α_2, the

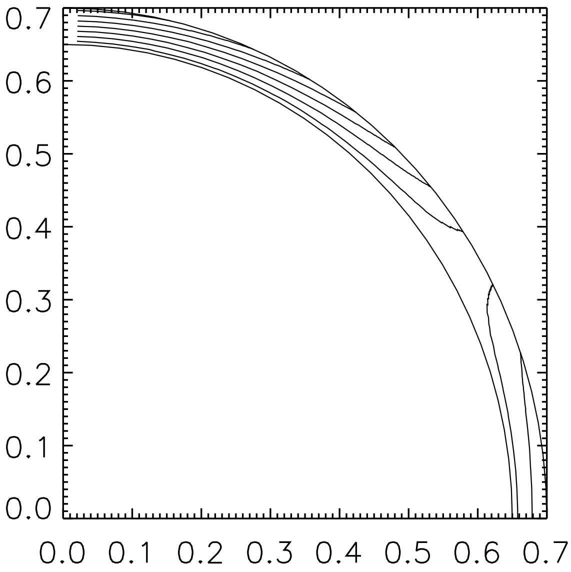

Figure 3.1: Vertical cross-section through the solar tachocline with contours of the assumed angular velocity depending on radius and latitude as given by Eq. (3.5). The highest angular velocity is at the equator (bottom right), and radially constant rotation occurs at a heliographic latitude of 30°.

marginal case with zero growth rate is sought. The linear (viscous) part of the full equation of motion is evolved implicitly, while the nonlinear parts are integrated explicitly with the advection term and the forces being computed in real space. This splitting in the original code is maintained as it is even in the linearized problem, since a fully implicit scheme would have required a substantial modification of the code. The $\triangle \boldsymbol{u}$ is thus treated implicitly, the other R.H.S. terms (two remaining after curling) are computed in real space and are used for a second-order Runge-Kutta integration.

The viscous Reynolds number (Re) will be used in this Chapter instead of the magnetic Reynolds number given by Eq. (1.29) as a free parameter. Similar to Rm, the viscous Reynolds number is essentially a variation of the viscosity ν since radius and Ω_{eq} are sufficiently well known

$$\mathrm{Re} = \frac{R_{\mathrm{out}}^2 \Omega_{\mathrm{eq}}}{\nu}. \tag{3.7}$$

The solar Reynolds number in the tachocline is – in terms of the definition of Eq. (3.7) – about 10^{14}. In practice, the time series evolution for modest $\mathrm{Re} > 10^4$ was found to be numerically demanding. By comparison with known results from inviscid two-dimensional analyses, it was found that the critical viscous differential rotation at $\mathrm{Re} > 10^3$ or 10^4 is already sufficiently close to the inviscid value.

Only the non-axisymmetric velocity is decomposed into toroidal and poloidal potentials, as in Eq. (1.23). Since it is potentials being evolved, the continuity equation is

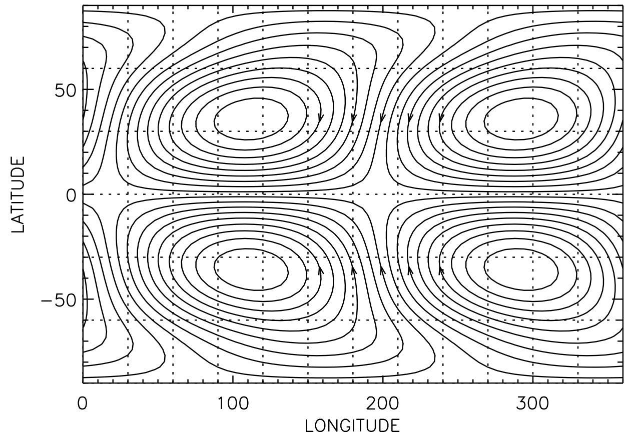

Figure 3.2: Streamlines of the symmetric Eigen-function of the computation with a three-dimensional profile $\Omega(r, \theta)$ on the surface of the tachocline at $r = 0.7$. Two circulation cells are found on each hemisphere.

fulfilled automatically. The density is constant throughout the computational domain. As the simulation domain is a thin shell of about 5% of the solar radius, constant density throughout the domain is a reasonably good approximation of the true situation. Any static or dynamic deformations of the tachocline are ignored. Thus, prolateness of the tachocline and its uneven thickness is assumed to have negligible effect on the results.

The radial boundary conditions for the velocity perturbations are stress-free at both R_{in} and R_{out}. At Reynolds numbers of $\text{Re} > 10^4$, high spectral resolution was necessary to obtain reliable results. Up to 80 Chebyshev and 80 Legendre polynomials were used to resolve the flow properly.

The azimuthal modes of the problem described by Eq. (3.6) are decoupled, and the stability of individual m-modes can be studied separately. Moreover, even and odd latitudinal modes (symmetric and antisymmetric modes with respect to the equator) decouple, and the critical differential rotation for the excitation of instability of the two kinds needs to be examined separately. The radial modes all couple and do not provide results on the stability of individual radial wavelengths.

3.3 Results

3.3.1 Stability of various solutions

In a set of fiducial computations, a purely latitudinal profile of the angular velocity was applied to the simulation domain. An $m = 1$ mode is evolved with the profile of Eq. (1.6), where $\alpha_4 = 0$ and α_2 is varied. Since it is a viscous problem, the critical differential rotation, α_2^{crit}, depends on the Reynolds number. The result is already very close to Watson's inviscid result for $\text{Re} \geq 1000$. This is a good reason to assume that the numerical solutions reaching $\text{Re} \sim 30\,000$ are suitable approximations for the solar plasma.

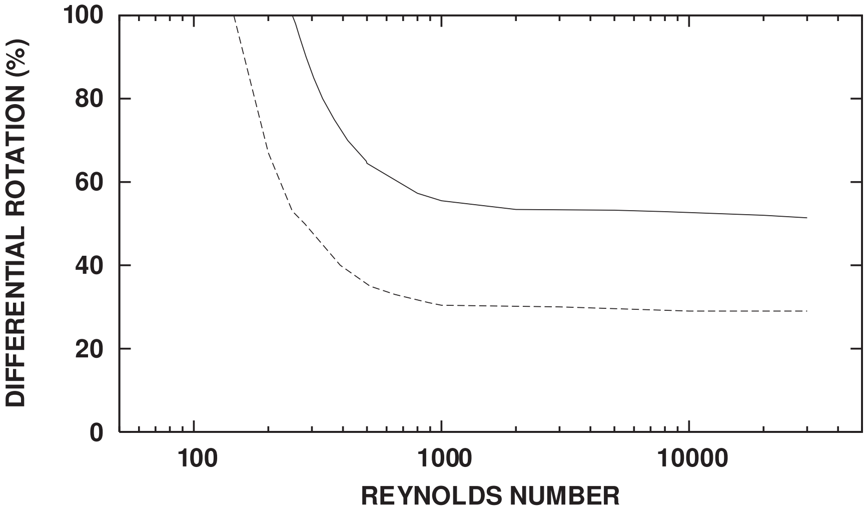

Figure 3.3: Lines of marginal stability for the combined latitudinal and radial shear (solid line) and the purely latitudinal shear (dashed line). Differential rotation denotes the percentage by which the pole's angular velocity is slower compared with the equatorial one. It is expressed by α_2 from Eq. (1.6) and Eq. (3.5) here.

Despite allowing for radial motions, the evolution provides solutions which are nearly toroidal and do not show significant radial flows. They are surface flows forming two cells on each hemisphere with stream lines through the poles. Figure 3.2 shows a representation of the flow in the spherical surface. The graph has to assume that the poloidal component of the velocity is zero, though, which is not entirely true.

The second step involved the rotation profile of Eq. (3.5), for which the critical steepness of the differential rotation, $\alpha_2^{\rm crit}$, is again sought for various Reynolds numbers. Figure 3.3 shows the lines of marginal stability, i.e. the critical differential rotation, versus Reynolds number for the symmetric $m = 1$ mode. The solid line refers to profile Eq. (3.5), and the dashed line is the latitudinal profile and converges to the result by Watson (1981) for $\mathrm{Re} \to \infty$.

The most easily excited patterns of $m = 1$ are always symmetric with respect to the equator. The lines of marginal stability of antisymmetric patterns are presented in left panel of Figure 3.4. They are stabler than the symmetric configurations with an $\Omega(r, \theta)$ profile. The antisymmetric solutions from the $\Omega(\theta)$ profile have also higher critical differential rotation values than their symmetric counterparts.

Modes with higher azimuthal wave numbers require significantly higher differential rotation for instability. The antisymmetric $m = 2$ mode, which is symmetric with respect to the equator, was found to be stable even in the entire parameter range covered by Figure 3.3. This is in agreement with the inviscid, two-dimensional stability analysis by Charbonneau et al. (1999a). The stability lines for the antisymmetric $m = 2$ mode are shown in the right panel of the Figure 3.4. No instability for any $m = 3$ mode in the range covered by Figure 3.3 was detected.

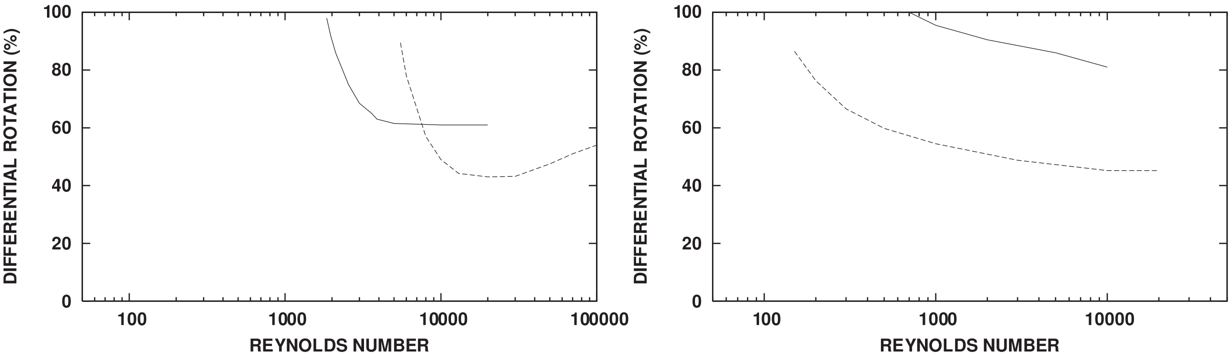

Figure 3.4: Lines of marginal stability for the antisymmetric $m = 1$ solutions (left) and antisymmetric $m = 2$ solutions (right) caused by the combined latitudinal and radial shear (solid line) and the purely latitudinal shear (dashed line).

The flow patterns drift with a certain velocity in azimuthal direction around the solar axis. Since the equations hold for the non-rotating system, the pattern rotation can be directly converted into physical times. The pattern rotation periods for the 2D and the 3D profiles of Ω are shown in Figure 3.5 by a dashed and a solid line, respectively. The actual solar rotation periods are also plotted. The reference equatorial period of 25.44 d ($\Omega_{\rm eq}$ = 455 nHz) is given as dash-dot line. The pattern rotation periods are determined at marginal stability. Since the marginal case gives us a value for the differential rotation, we also plot the polar rotation period $P_{\rm pole}$ versus Re. The short-dash line is for the two-dimensional $\Omega(\theta)$ profile, and the dotted line for the three-dimensional case described by Eq. (3.5).

The pattern rotation periods are always between the equatorial and polar rotation periods, in agreement with the 2D results by Charbonneau et al. (1999a). While the patterns from the 2D-Ω profile are close to the polar rotation period, the patterns for the 3D profile rotate with nearly the average rotation period between the polar and equatorial ones.

We can compute the time after which the pattern is passed by a given point on the equator. This time is often called lap time. Assuming an equatorial rotation period of 25.44 d ($\Omega_{\rm eq}$ = 455 nHz), we find a lap time of 91 d for the 2D case and a lap time of 78 d for the 3D case.

3.3.2 Effects of buoyancy

Little influence is expected from the stable temperature gradient in the tachocline. To prove the point, the effect of a negative buoyancy force on the stability of the differential rotation is demonstrated in this subsection. The Navier-Stokes Eq. (3.6) is extended by

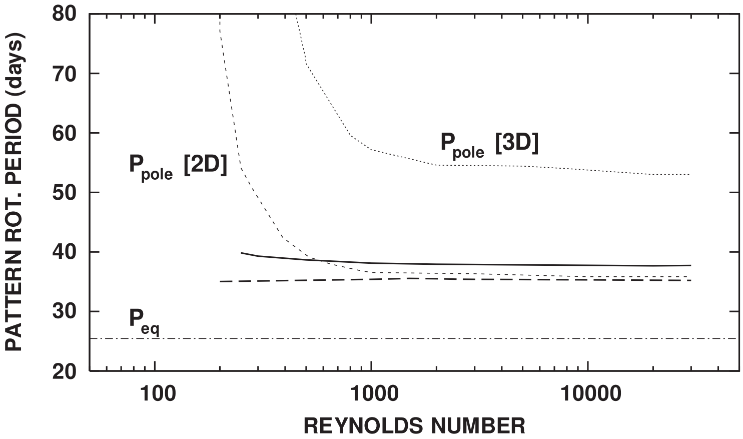

Figure 3.5: Rotation period of the flow pattern for the two-dimensional (long-dashed) and the three-dimensional (solid) rotation profile. The numbers are computed assuming an equatorial rotation period of 25.44 d ($\Omega_{\rm eq} = 455$ nHz) plotted with a dash-dot line. Periods are computed at marginal stability; the polar rotation period for this critical differential rotation is plotted as short-dashed and dotted lines for the 2D and 3D cases, respectively.

the buoyancy force and reads as

$$\begin{aligned}\frac{\partial \boldsymbol{u}}{\partial t} &= \boldsymbol{u} \times \nabla \times \boldsymbol{U} + \boldsymbol{U} \times \nabla \times \boldsymbol{u} + \mathrm{Ra}\Theta \boldsymbol{r} - \nabla P - \nabla(\boldsymbol{u} \cdot \boldsymbol{U}) + \triangle \boldsymbol{u}, &(3.8)\\ \frac{\partial \Theta}{\partial t} &= -\boldsymbol{U} \cdot \nabla\Theta - \boldsymbol{u} \cdot \nabla T_0 + \frac{1}{\mathrm{Pr}}\triangle\Theta, &(3.9)\end{aligned}$$

with a background temperature profile same as Eq. (1.27). The Rayleigh number in Eq. (3.8) is also non-magnetic as compared to Eq. (1.31) and takes the form

$$\mathrm{Ra} = \frac{g\alpha(T_{\rm in} - T_{\rm out})R_{\rm out}^3}{\nu^2}, \tag{3.10}$$

where $T_{\rm in}$ and $T_{\rm out}$ are the temperatures at the two boundaries. Like in the previous Chapter, in the Boussinesq formulation used here, the presence of a sub-adiabatic temperature gradient actually translates into a negative value of Ra. The Rayleigh number is set to a value as small ("as negative") as $\mathrm{Ra} = -10^8$ in order to see any notable effect on the flow. The Prandtl number is set to unity.

The critical differential rotation for a growing symmetric $m = 1$ mode at $\mathrm{Re} = 10^4$ increases slightly to 53.3%, as compared with the non-buoyant value of 52%. This is in line with the fact that the solutions contain nearly horizontal motions.

3.3.3 Effects of higher-degree terms

The differential rotation has been expressed by a $\cos^2\theta$ dependence in latitude and a linear r dependence over radius. We are studying the stability of the three-dimensional tachocline setup with higher-degree dependences in this section, such as the $\cos^4\theta$ term and a nonlinear radial dependence of Ω.

Including the $\cos^4\theta$ term in Eq. (3.5) yields an angular velocity profile of the form

$$\begin{aligned}\Omega(r,\theta) &= \Omega_{\mathrm{eq}}\Bigg\{1-\alpha_2\cos^2\theta-\alpha_4\cos^4\theta \qquad (3.11)\\ &\quad -\left(\frac{R_{\mathrm{out}}-r}{R_{\mathrm{out}}-R_{\mathrm{in}}}\right)\left[\alpha_2\left(\frac{1}{4}-\cos^2\theta\right)+\alpha_4\left(\frac{1}{16}-\cos^4\theta\right)\right]\Bigg\}\end{aligned}$$

The computations for the full profile could not be easily extended beyond Re = 5000, but the results for the possible Re and for the easier two-dimensional $\Omega(\theta)$ show no decreased critical differential rotation when the $\cos^4\theta$ term is included. This also holds for the extreme case of α_4 carrying the shear alone ($\alpha_2 = 0$). In some cases, the total critical differential rotation ($\alpha_2+\alpha_4$) in-fact increased after inclusion of the α_4 term, the effect being more prominent for higher $\alpha_4-\alpha_2$.

Starting from Eq. (3.5), a modified Ω-profile was constructed in order to find any influence of the particular radial dependence of the latitudinal shear on the results. We used

$$\Omega(r,\theta)=\Omega_{\mathrm{eq}}\left\{1-\alpha_2\cos^2\theta-\alpha_2\left(\frac{1}{4}-\cos^2\theta\right)\frac{1}{2}\left[1-\cos\left(\frac{R_{\mathrm{out}}-r}{R_{\mathrm{out}}-R_{\mathrm{in}}}\pi\right)\right]\right\}. \qquad (3.12)$$

The radial profile introduces an inflection point. It does not apply the usual error function for the radial Ω-step in order to obtain an exact $\partial\Omega/\partial r = 0$ at both inner and outer boundaries. A graphic representation is shown in Figure 3.6.

The critical differential rotation for instability is shown versus Reynolds number in Figure 3.7. Unlike the earlier simulations, a Reynolds number of 10^5 could be achieved, probably because of the vanishing $\partial\Omega/\partial r$ at the boundaries. Instability does not occur at reduced differential rotation, and the line of marginal stability actually converges to the simpler profile Eq. (3.5) for high Re. The additional effect of buoyancy on the stability of the profile Eq. (3.12) with an inflection point is also shown as a dashed line.

3.4 Discussion

A fully three-dimensional, linear analysis of the stability of the solar tachocline was carried out in this Chapter. If radial variation of the angular velocity is included in the model, the maximum pole-equator difference of the angular velocity can be as large as 52% for a symmetric $m = 1$ mode before instability sets in. Two-dimensional analyses have delivered much lower critical values. The difference between 3D and 2D is not radial flows emerging from the extension in the third dimension, but it is the changed stability conditions emerging from the radial shear and radial dependence of the differential rotation.

Other modes, such as higher m or different flow symmetries, do not get unstable at lower critical differential rotation values under the influence of a three-dimensional rotation profile.

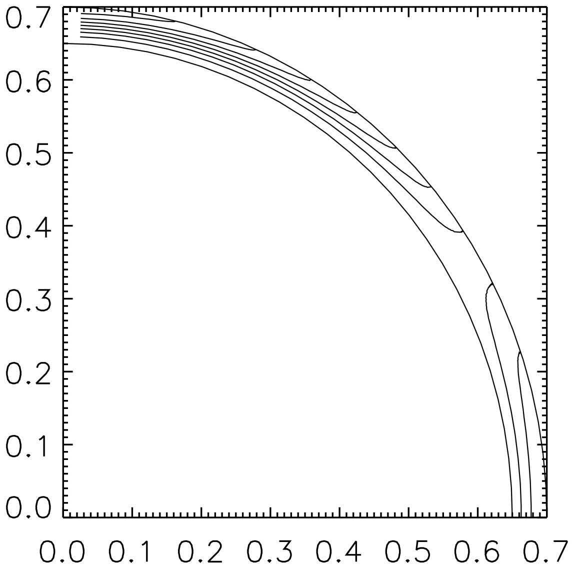

Figure 3.6: Contours of the assumed angular velocity with a radial dependence as in Eq. (3.12). The highest angular velocity is again at the equator (bottom right), and radially constant rotation occurs at a heliographic latitude of 30°.

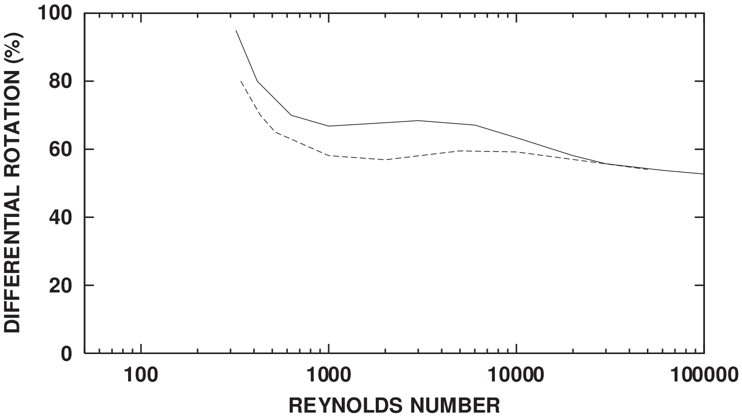

Figure 3.7: Lines of marginal stability for an angular velocity profile given by Eq. (3.12) having an inflection point over radius. The solid line refers to the non-buoyant case, Ra = 0; the dashed line has Ra $= -10^8$.

The stabilizing effect of the temperature gradient has been added, but since all the unstable modes are almost horizontal, the influence is small. The assumption that horizontal motions dominate is valid even without a stabilizing temperature gradient. However the assumption that spherical shells of infinitesimal thickness do not interact with each other is not applicable, according to these results. One may argue that the viscosity in these computer simulations is much too high, but the variation of the results is small at $\mathrm{Re} > 1000$. This is an indication that computations with $\mathrm{Re} = 10^4$ or higher are a good approximation of the near-inviscid solar case. It can be concluded that all parts of the tachocline not affected by convective overshooting are stable in the hydrodynamic case.

However, these stability conditions can be expected to change, owing to the Lorentz stresses when toroidal magnetic field belts are included. This case is more relevant for the Sun as most solar dynamo models include such high toroidal magnetic field in the region. An MHD stability analysis will be presented in the next Chapter.

Chapter 4

MHD stability of the tachocline

As shown in the previous Chapter, the tachocline is hydrodynamically stable. In reality, however, it is believed that the tachocline is the seat of high amplitude toroidal field belts. This Chapter examines the effect of such fields on the tachocline.

Tayler (1973) was the first one to examine stability of the purely toroidal fields. He showed that any purely toroidal field should be unstable to instabilities on the magnetic axis of the star. These are pinch-type instabilities, under the influence of the strongly stabilizing stratification in a radiative stellar interior. They are called Tayler Instabilities. The toroidal magnetic field in the tachocline is also subject to other instabilities like magnetic buoyancy (Parker 1955; Gilman 1970; Acheson 1978) or magnetic shear instabilities (Velikhov 1959; Acheson 1978; Balbus & Hawley 1992). All these instabilities, except the Tayler instability, have a stabilizing effect in the stratified interior. On the other hand, the Tayler instabilities occur on the magnetic axis, where the magnetic field is perpendicular to gravity and displacements caused by the instability are also perpendicular to gravity. Thus, as shown by Spruit (1999), the Tayler instability will be the first to appear as the strength of the toroidal field is increased.

The shape of the unstable displacements is shown in Figure 4.1, for modes with $m = 0, 1, 2$. The $m = 1$ mode is called kink instability and sets in once the magnetic field component along the flux falls below some critical value in relation to the toroidal component. It is predicted, in a cylindrical system, for instability to occur, the following conditions need to be satisfied (Tayler 1973).

$$\frac{\partial \ln B}{\partial \ln r} > \frac{m^2}{2} - 1 \quad (m \neq 0) \quad \text{and} \quad \frac{\partial \ln B}{\partial \ln r} > 1 \quad (m = 0). \tag{4.1}$$

The growth rates of these instabilities are expected to be of the order of a few years or smaller, given by

$$\gamma = \frac{B^2}{\mu_0 \rho r^2 \Omega} = \frac{\omega_A^2}{\Omega}, \tag{4.2}$$

where γ is the growth rate of the instability and ω_A is the Alfvén frequency (Pitts & Tayler 1986; Spruit 1999). The equation holds true when the Alfvén frequency is much smaller

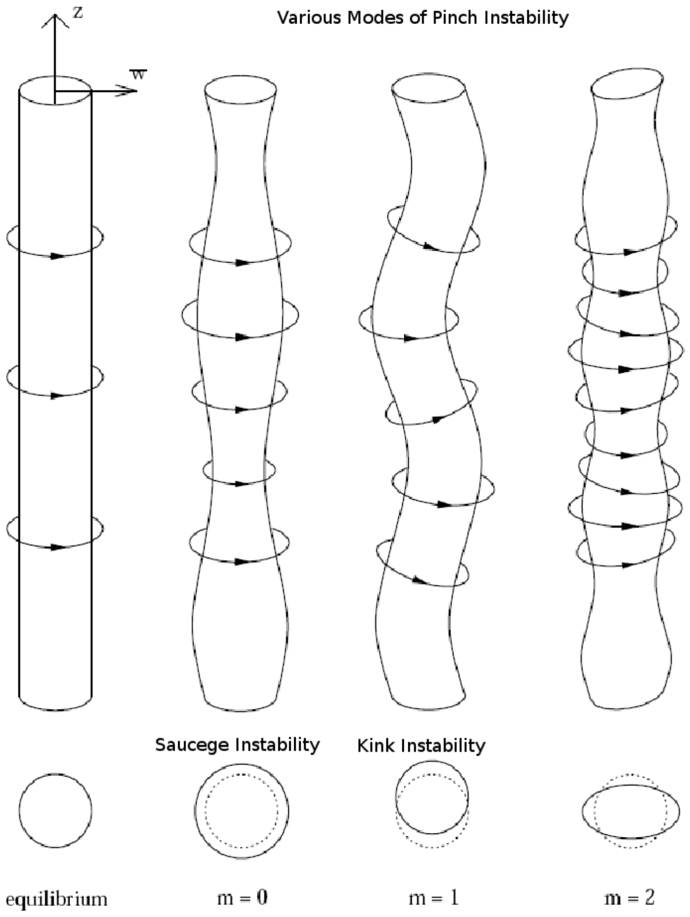

Figure 4.1: A cartoon showing the physical form of the Tayler instability, for modes $m = 0, 1, 2$. Above co-moving surfaces are drawn with the magnetic field represented by lines with arrows. Gravity acts along the magnetic axis (Z). Cross-sections of these surfaces are plotted below with dotted circles representing the equilibrium state. Source: Braithwaite (2006).

than the rotational rate (Ω), which in turn should be much smaller than the buoyancy frequency.

In case of the solar tachocline, this instability is expected to be present and many authors have attempted to address this problem in the past.

4.1 Lower Dimensional Models

The earliest stability analysis of toroidal magnetic fields in the solar case was done by Caligari et al. (1995) and was followed up by Ferriz-Mas & Schüssler (1996). They used a one-dimensional flux tube approximation and concluded that the stability limit is in excess of 10^4G in the tachocline as well as the lower convection zone. Gilman & Fox (1997) studied the effect of toroidal magnetic field on latitudinal differential rotation in the solar tachocline. The model used was similar to Watson (1981), i.e. only a spherical surface was considered but the magnetic fields were included on this differentially rotating surface. They found that the toroidal magnetic field belts can make the tachocline unstable for virtually all values of magnetic field amplitude and differential rotation. They found the peak instabilities have e-folding times corresponding to just a few months. Two clearly distinct regimes of instability were identified in this study. It was found that at low B the instability is driven by the differential rotation (hydrodynamic instability) and at high B it is driven by the toroidal field (magnetic instability).

The model of Gilman & Fox (1997) was followed by a series of papers. Dikpati & Gilman (1999) studied the dependence of the instability on the width of the toroidal field band with the peak of the profile always located at a latitude of 45. Symmetric latitudinal modes were found to be more unstable than antisymmetric ones with stronger fields being more unstable. The system is most unstable for an intermediate width of toroidal field belts $(10 - 20)$. Both narrow and widely spread belts are more stable than this configuration with very narrow bands (3 or smaller) showing no instability at all. For weaker magnetic fields, the $m = 2$ mode was found to be more unstable than the $m = 1$ which dominates at stronger magnetic fields. In a subsequent paper, Gilman & Dikpati (2000) examined the stability of fixed-width toroidal fields placed at different latitudes. It was found that belts placed at high latitudes become unstable for fields of even a few hundred Gauss but lower latitude belts remain stable unless fields exceed 10^4G. The numerical scheme adopted in this work prevented the authors from searching for critical value of magnetic fields but it was reported that instabilities can have e-folding times[1] of the order of a few months. The widths of the latitudinal belts were chosen as 10, 6 and 4 in these simulations. When the belt was placed at mid-latitudes, comparatively higher azimuthal modes $(m = 4 - 7)$ turned out to be the most unstable ones, whereas the lower azimuthal modes $(m = 1 - 2)$ were the most unstable at the lower as well as higher latitudes. For very strong magnetic field no instability was observed (growth rates going to zero).

Cally (2003) used a 3-dimensional inviscid spectral code, but his model ignored radial shear as well as radial magnetic field gradients. He found two regimes of instability corresponding to $V_\mathrm{A} > V_\mathrm{rot}$ and $V_\mathrm{A} < V_\mathrm{rot}$, with V_A and V_rot corresponding to Alfvén and rotational velocity respectively[2]. In the former case, the $m = 1$ polar kink instability is the dominant one with e-folding times of a few months and in the latter case instability is primarily restricted to very short radial length scales. The 2-dimensional surface model of Gilman & Fox (1997) was extended to include magnetic diffusivity and kinematic viscosity by Dikpati et al. (2004). Instability was found to exist for a wide range of ν and η for a toroidal field of 10^5G. Zhang et al. (2003) considered the case of non-axisymmetric instabilities for a specific magnetic field profile. Braithwaite (2006) examined the 3D stability of a rigidly rotating star using a box grid MHD code. Very recently, Brun & Zahn (2006), in their examination of the magnetic confinement of the solar tachocline, found the tachocline becoming unstable with a dominant $m = 1$ mode close to the pole and higher m modes at slightly lower latitudes, for a toroidal field of roughly a few hundred Gauss.

---

[1] e-folding time is the time taken by the instability to grow by a factor of e in amplitude.

[2] The same criteria can be rewritten as "$\mathrm{S} > \mathrm{Rm}$ and $\mathrm{S} < \mathrm{Rm}$" or roughly "$B > R\Omega$ and $B < R\Omega$".

4.2 The Model

Since the study aims at the stability of a given background state against small non-axisymmetric perturbations, the problem is formulated by linearized equations, similar to the previous Chapter. As mentioned in the last Chapter, the buoyancy force does not drastically change the stability criterion; hence the buoyancy term is neglected here. As before, after linearization, we can separate the axisymmetric background rotation $\boldsymbol{U} = (0, 0, r \sin\theta\Omega)$ from the non-axisymmetric flow $\boldsymbol{u}$, with Ω being a normalized angular velocity. An imposed axisymmetric toroidal magnetic field $\boldsymbol{B} = (0, 0, B_\phi)$ is also separated from the perturbations $\boldsymbol{b}$. The background poloidal field is ignored in this analysis as in the Sun, it is expected to be atleast 2-3 orders smaller than the toroidal field[3]. The lower-case quantities are evolved by numerical computations. The upper-case quantities may depend on r and θ, but not on ϕ. The Navier-Stokes equation is similar to Eq. (3.6) and the induction equation given by Eq. (1.34) is normalized as well.

$$
\begin{aligned}
\frac{\partial \boldsymbol{u}}{\partial t} &= [\boldsymbol{u} \times (\nabla \times \boldsymbol{U}) + \boldsymbol{U} \times (\nabla \times \boldsymbol{u}) - \nabla(\boldsymbol{u} \cdot \boldsymbol{U})] + [(\nabla \times \boldsymbol{b}) \times \boldsymbol{B} + (\nabla \times \boldsymbol{B}) \times \boldsymbol{b}] \\
&\quad -\nabla P + \mathrm{Pm}\triangle \boldsymbol{u}, \qquad (4.3) \\
\frac{\partial \boldsymbol{b}}{\partial t} &= \nabla \times (\boldsymbol{U} \times \boldsymbol{b} + \boldsymbol{u} \times \boldsymbol{B}) - \triangle \boldsymbol{b}. \qquad (4.4)
\end{aligned}
$$

All symbols have their standard meaning. As in the previous Chapter, exponentially decaying or growing solutions should be sought in order to find the critical magnetic background field strength B_ϕ of the marginal case. The viscous part of the equation of motion is evolved implicitly, while the other parts are integrated explicitly with the advection term and forces being computed in real space. This splitting is maintained as it is even in the linearized problem, since a fully implicit scheme would have required a substantial modification of the code. The $\triangle \boldsymbol{u}$ is thus treated implicitly, the other RHS terms (four remaining after curling) are computed in real space.

In the normalized units, the computational domain covers the radial extent from $R_\mathrm{i} = 0.5$ to $R_\mathrm{o} = 0.7$. The outer radius is thought of as the radius at which the high turbulent viscosity and diffusivity turn into nearly microscopic values at the bottom of the convection zone. It is not important for the findings at which radius this happens precisely in reality. The inner radius is not meant to have a physical meaning. It is chosen far enough from the radii at which the interesting features of the background state, such as magnetic fields and differential rotation will be placed, that it is unimportant for the results. Since the

---

[3] It should be noted that, as argued in Malkus (1968), the stability criteria after inclusion of the poloidal field may differ from the model. The models with both poloidal and toroidal background magnetic field are beyond scope of this work

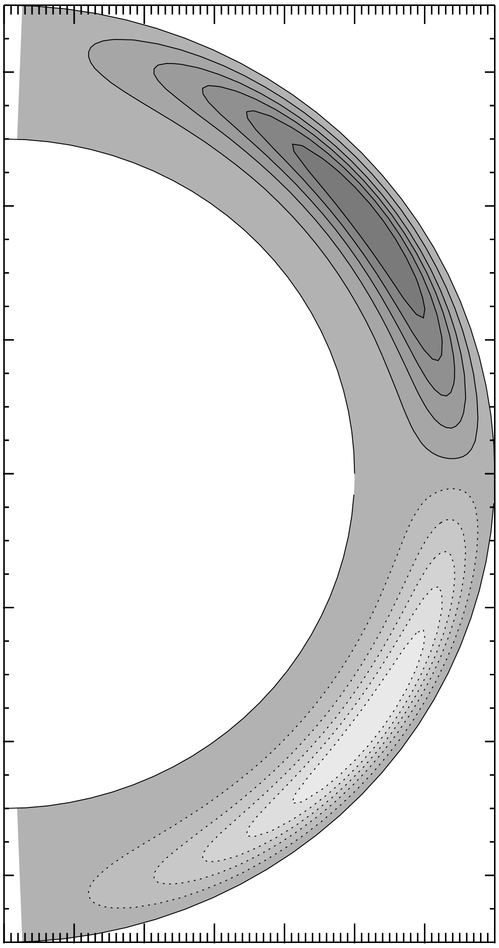

Figure 4.2: Contour lines of the toroidal magnetic field strength of the imposed axisymmetric magnetic field if $n = 2$, $p = 2$ and $q = 1$ with a positive B_ϕ in the northern hemisphere and a negative one in the southern hemisphere.

linearized equations decouple for azimuthal Fourier modes m, instability limits for each m-mode are sought individually.

The background magnetic field is purely toroidal and is distributed by,

$$B_\phi = \sin^p \theta \cos^q \theta \sin^2 \left[\pi \left(\frac{r - R_\mathrm{i}}{R_\mathrm{o} - R_\mathrm{i}} \right)^n \right], \tag{4.5}$$

where p, q and n are the free exponents controlling the latitudinal placement and the radial thickness of the toroidal field belt. p and n take even values and q takes odd values. In the next Section, mostly $n = 2$ is used, giving a thickness of about 0.1 solar radii. Figure 4.2 illustrates the configuration. The maximum B_ϕ sits at a radius of $r = 0.641$ and a colatitude of $\theta = 55$ in the northern hemisphere. If $n = 4$, the maximum is at $r = 0.668$. The full radial widths at half-maximum of these profiles are $d = 0.073$, $d = 0.044$, and

$d = 0.025$ for $n = 2$, 4, and 8, respectively. For most of the cases, $p = 2$ and $q = 1$ are chosen. This means the "eye" of the toroidal field belt is located at a latitude of 35. The particular profile is chosen as it qualitatively resembles the profile of magnetic field obtained in section 2.4.5. The resemblance is evident when Figure 2.13 and Figure 4.2 are compared.

As said before, the solar magnetic Reynolds number in the tachocline is about 10^{12}. In reality, one tries to achieve time series for numerically demanding $\mathrm{Rm} = 2 \cdot 10^4$ and slightly above. Magnetic-field belts with $n = 2$ can be treated with relatively low resolution, such as 20 Chebyshev and 40 Legendre modes for the decomposition of the meridional structure. Thinner field belts obtained with $n = 4$ require significantly higher resolution. A decomposition into 40 Chebyshev and 80 Legendre modes was necessary to achieve numerical stability.

The boundary conditions for the magnetic field $\boldsymbol{b}$ are vacuum for both radial boundaries. The turbulent convection zone on top may easily provide vacuum-like conditions. The inner boundary is actually conducting. However, the conductivity is nearly constant across the inner boundary. In the context of a finite conductivity in the computational domain, this is far from ideally conducting. In order to prevent artificially strong magnetic fields near the boundary, we chose vacuum conditions also for the inner boundary. The boundary conditions for the $m \geq 1$ flow are always stress-free, whereas an axisymmetric background velocity is prescribed in the models. The velocity fluctuations $\boldsymbol{u}$ do not of course change the average rotation velocity of the surfaces of the spherical shell. The boundary conditions also mean that there will be no boundary layers of strong shear near the inner or outer surfaces.

4.3 $m = 1$ Mode Stability Analysis

4.3.1 Rigid rotation

In order to understand the influence of toroidal magnetic fields and differential rotation separately, one has to first start with a rigidly rotating spherical shell, i.e. $\Omega(r, \theta) = \Omega_{\mathrm{eq}}$.

Symmetric and antisymmetric solutions with respect to the equator are also decoupled in the linearized system investigated here. At a given Rm, the critical Lundquist number is sought at which the growth rate of the perturbation excited is zero. The critical Lundquist numbers for an $m = 1$ mode in the range of $\mathrm{Rm} = 10$ to $20\,000$ is shown in Figure 4.3 (left). The magnetic Prandtl number was $\mathrm{Pm} = 1$ in these runs. The dotted line was obtained for the solution with a velocity field which is antisymmetric with respect to the equator, the solid line is for the solution with a symmetric velocity field. There is a magnetic instability also without rotation. It occurs at $\mathrm{S} = 155$ for the symmetric $m = 1$ mode and at $\mathrm{S} = 132$ for the antisymmetric mode. For high magnetic Reynolds numbers, it appears that the symmetric mode is dominating. This study will thus focus on the stability limits of the symmetric mode below, as it is likely to be the interesting one for solar tachocline applications.

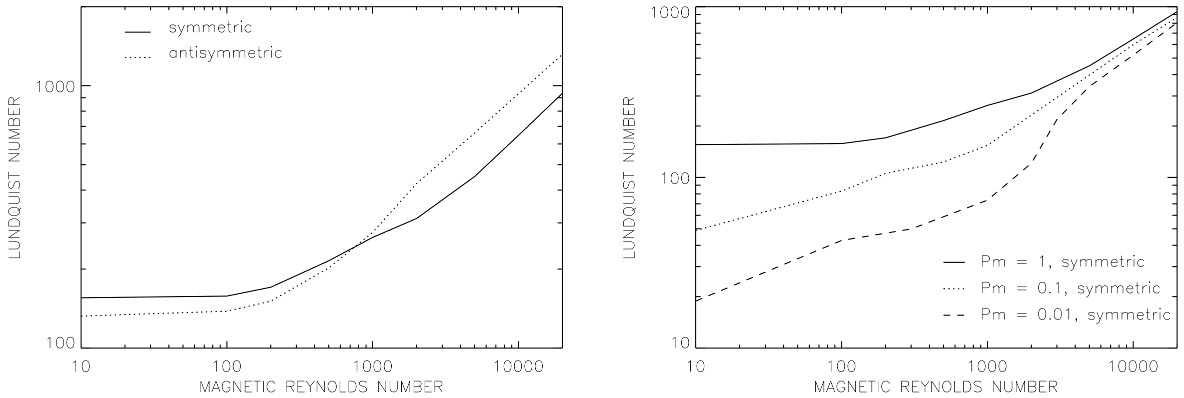

Figure 4.3: (left) Lines of marginal stability in a rigidly rotating sphere for different symmetries of the $m = 1$ mode with respect to the equator. The solid line is for the solution with a symmetric velocity field; the dotted line is for the antisymmetric velocity field. The magnetic Prandtl number was unity. (right) Lines of marginal stability in a rigidly rotating sphere for various values of the magnetic Prandtl number Pm.

The magnetic Prandtl number is much lower than unity in the solar tachocline. The stability analysis was repeated for $\mathrm{Pm} = 0.1$ and $\mathrm{Pm} = 0.01$ assuming that the symmetric mode is the most interesting one for solar applications. The lines of marginal stability are shown in Figure 4.3 (right). With an antisymmetric background magnetic field as described by Eq. (4.5), an antisymmetric $m = 1$ mode is obtained for the magnetic field $\boldsymbol{b}$, too. A vertical cross-section of a growing mode is shown in Figure 4.4. Note that the picture changes if one goes to other longitudes of the computational domain.

As stated before, one cannot access solar magnetic Reynolds numbers in the numerical model. However, the dependence of the critical Lundquist number on Rm may give us a scaling relation for the extrapolation to a solar magnetic Reynolds number. The stability lines in Figure 4.3 (right) indicate a convergence to a common slope for all three Pm. Such a common slope occurs for magnetic Reynolds numbers of 5000–20 000. Higher Reynolds numbers have not yet been accessible by the numerics so far. Assuming that the slopes remain constant for higher Rm, the scaling can be expressed as,

$$\mathrm{S}_{\mathrm{crit}} = \hat{\mathrm{S}}\,\mathrm{Rm}^{\beta}\,, \tag{4.6}$$

where β is the slope in a log-log plot and $\hat{\mathrm{S}}$ is the amplitude of the fit curve. In the particular case shown in Figure 4.3 (right), a scaling of,

$$\mathrm{S}_{\mathrm{crit}} = 1.6\ \mathrm{Rm}^{0.63}, \tag{4.7}$$

is found for the high-Rm part of the $\mathrm{Pm} = 0.01$ line. Because both S and Rm depend on

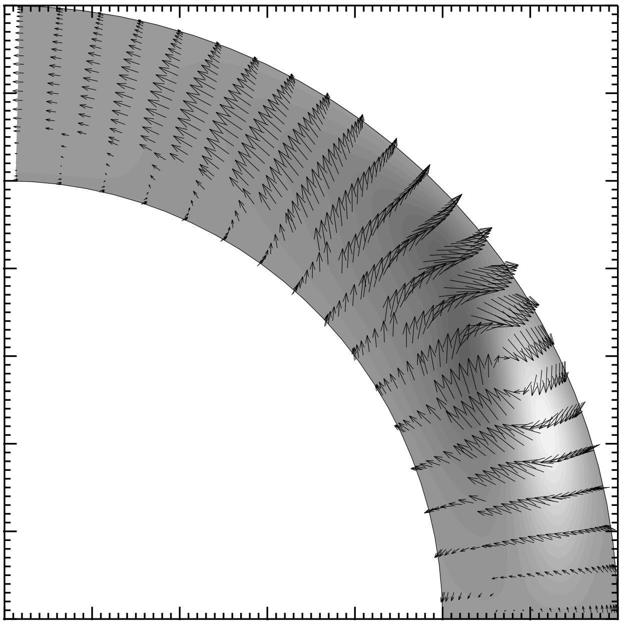

Figure 4.4: Magnetic-field perturbation growing in a rigidly rotating sphere at a magnetic Reynolds number of Rm = 10 000 and a (supercritical) Lundquist number of S = 2000. The grey scaling represents b_ϕ (without the background profile B_ϕ of Eq. (4.5)), and the arrows are the field vectors projected on the meridional section.

the magnetic diffusivity η, it is helpful to replace them by their definitions, leading to,

$$\begin{aligned} B_{\rm crit} &= \frac{\hat{\rm S}\sqrt{\mu\rho}}{R}\left(R^2\Omega_{\rm eq}\right)^\beta \, \eta^{(1-\beta)} \\ &= Q(\beta)\,\eta^{(1-\beta)}. \end{aligned} \qquad (4.8)$$

When scaled to a solar tachocline diffusivity of $\eta = 3000$ cm^2/s (Stix & Skaley 1990), a critical strength of the toroidal magnetic field of $B_{\rm crit} \approx 12$ Gauss is obtained. The density was taken to be $\rho = 0.25$ g/cm^3 for the tachocline (Guenther et al. 1992). It must be noted how sensitive Q is towards β which is derived from the curves in Figure 4.3 (right) at high magnetic Reynolds numbers. There is a factor of 10 change in Q, if β is changed by 0.05. This is in fact roughly the uncertainty of the determination of β.

Since the tachocline is to a large extent stably stratified, the computations were repeated without the development of a poloidal flow. Preventing radial motions entirely corresponds to the case of extremely stable stratifications. Since the numerical scheme solves the toroidal and poloidal potentials of the flow and the field separately, it is as easy as dropping one of the equations to imitate the stable stratification.

The stability limits resulting from these calculations with purely horizontal flows are shown in Figure 4.5. The β derived from the slopes of the curves for Pm = 0.1 and 0.01 are close to the above value for the full flow. The horizontal flow yields $\beta = 0.59$, but a somewhat larger $\hat{S}$. Eq. (4.8) gives a critical strength of the toroidal magnetic field of

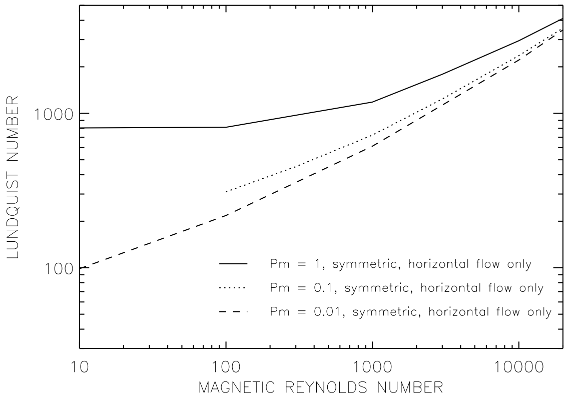

Figure 4.5: Lines of marginal stability in a rigidly rotating sphere as in Figure 4.3, but with the flow restricted to toroidal motions.

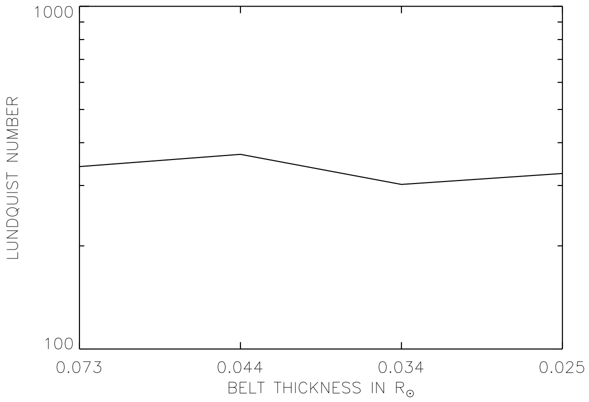

Figure 4.6: Critical magnetic-field strengths as a function of the thickness of the field belts. The values were derived for the symmetric $m = 1$ mode at Rm = 5000 and Pm = 1.

20 G, again assuming a diffusivity of $\eta = 3000$ cm^2/s. This value is practically the same as for the full flow, keeping in mind the general uncertainty of the extrapolation.

4.3.2 Thickness of field belts

The exponent $n = 2$ in the definition Eq. (4.5) of the magnetic-field belts yields a radial thickness of the magnetic structure of roughly 7% of the solar radius. Higher n produce slimmer belts, and the change in stability can be investigated. In order to achieve numerical stability for very thin belts, we chose a moderate magnetic Reynolds number of Rm = 5000 for this test. The full meridional flow was permitted in the calculations.

The dependence of the critical magnetic field in terms of Lundquist numbers on the thickness of the B_ϕ-belts is plotted in Figure 4.6. There is no significant trend toward lower or higher stability limits when going to very thin belt thicknesses. The computations may show whether there is a smooth transition to the results of two-dimensional computations on spherical surfaces or to flux-tube simulations. These led to maximum field strengths of 10^4–10^5 Gauss. One has to conclude that calculations with no radial gradients and/or no radial extent may not be able to give full account of the instability of strong magnetic toroidal fields.

4.3.3 Latitudinal differential rotation

The next step consists of adding a differential rotation to the spherical shell. The angular velocity Ω should depend only on the latitude for the moment,

$$\Omega = \Omega_{\rm eq}(1 - \alpha \cos^2 \theta), \tag{4.9}$$

where θ and α have their usual meaning. At $\alpha = 1$, the pole is at rest.

As seen in the previous Chapter, a purely latitudinal differential rotation is hydrodynamically unstable for $\alpha > 0.28$ (Watson 1981). In the real solar tachocline, however, the differential rotation is accompanied by toroidal magnetic field belts, caused by the latitudinal differential rotation with the presence of poloidal magnetic seed field. The location of these belts is not known with any certainty but the emergence of the sun-spots at the solar surface require them to be present. As the active regions of the Sun are near the equatorial latitudes, one can expect the toroidal field belts also to be located there. In other stars, where big polar spots are observed, the toroidal field belts, if they indeed are related to surface activity, should also be at higher latitudes. Now, these toroidal field belts of Eq. (4.5) are added to the differential rotation. The resulting areas of stability are shown in Figure 4.7 (left) for two magnetic Reynolds numbers, Rm = 1000 and 10 000. The horizontal axis is the ratio of the Lundquist number to the magnetic Reynolds number. This is a useful choice as it does not contain the only unknown in the normalization, the magnetic diffusivity. The ratio is in fact a measure for the ratio of the Alfvén velocity to the rotational velocity at the equator.

At the lower Reynolds number of the two, viscosity is still large enough to increase the limit for hydrodynamic instability (intersection with vertical axis) to about 55% differential rotation. The two solid lines in the upper left and lower right corner are the stability limits. The area in between the two is the stable region.

At Rm = 1000 the latitudinal differential rotation is stabilized by a relatively weak magnetic field. There is actually a certain magnetic field strength for which even 100% differential rotation (resting pole) is stable. However, very strong magnetic fields destabilize the rotation profile as a consequence of what can be identified as Tayler instability. Starting from the purely magnetic instability on the horizontal axis of the graph, it is found that differential rotation stabilizes the Tayler branch. There is no instability at all for the ratios S/Rm of 1.8 to 2.6.

At Rm = 10 000 the totally stable region disappears. There is no stability at ratios of Lundquist number to magnetic Reynolds number higher than 0.14. However, the stabilizing

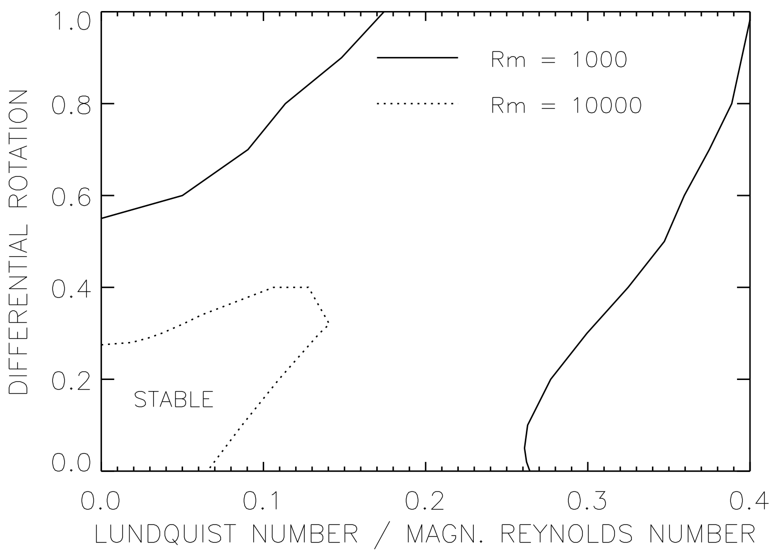

Figure 4.7: Lines of marginal stability for toroidal magnetic field belts in a differentially rotating spherical shell with $\Omega \sim (1 - \alpha \cos^2 \theta)$. The value of α is given on the vertical axis. The magnetic Reynolds number of these computations was fixed at $\mathrm{Rm} = 1000$ for the solid line and at $\mathrm{Rm} = 10000$ for the dotted line.

effect of a weak magnetic field on the hydrodynamic instability as well as the stabilizing effect of a weak differential rotation on the magnetic instability are still evident.

4.3.4 Full differential rotation

The next step is to consider a differential rotation profile which depends on both latitude and radius. The hydrodynamic instability of such a rotation profile emerges at stronger differential rotation than for purely latitudinal differential rotation (see Figure 3.3).

In parallel to Eq. (3.5) the full differential rotation profile is now,

$$\Omega = \begin{cases} \Omega_{\mathrm{eq}} \left[1 - \alpha \cos^2 \theta - \alpha \left(\frac{1}{4} - \cos^2 \theta \right) \frac{R_{\mathrm{o}} - r}{R_{\mathrm{o}} - R_{\mathrm{t}}} \right] & \text{if } r > R_{\mathrm{t}} \\ \Omega_{\mathrm{eq}} \left[1 - \frac{\alpha}{4} \right] & \text{if } r \leq R_{\mathrm{t}}, \end{cases} \tag{4.10}$$

where R_{t} is the radius of the bottom of the tachocline below which no differential rotation is prescribed. This is different from the configuration of the model described in the previous Chapter as there is an extended radial zone now below the differentially rotating shell in which the angular velocity is constant. The value of the tachocline radius was set to $R_{\mathrm{t}} = 0.6$ for the relatively thick magnetic-field belts constructed by $n = 2$ in Eq. (4.5), and was set to $R_{\mathrm{t}} = 0.65$ for the $n = 4$ case.

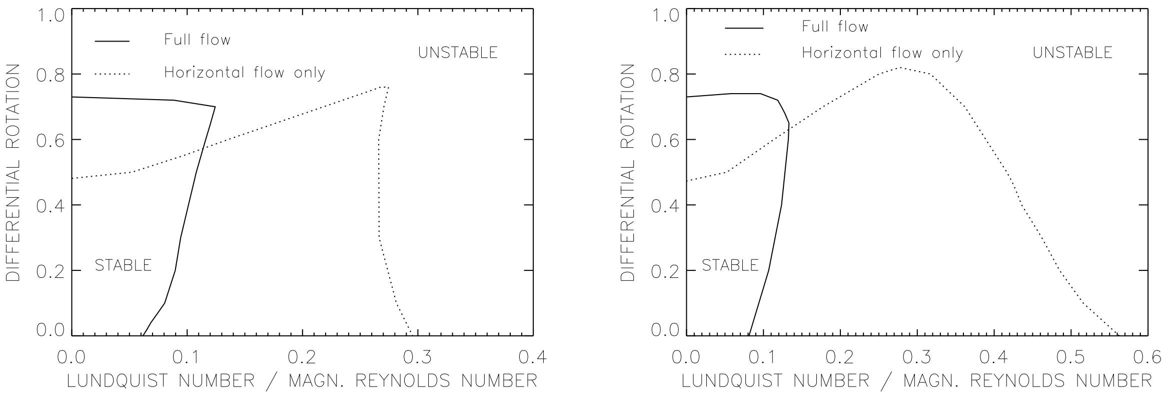

Figure 4.8: Lines of marginal stability for toroidal magnetic field belts with $n = 2$ (left) and $n = 4$ (right) in a differentially rotating spherical shell at a magnetic Reynolds number of $\mathrm{Rm} = 10\,000$. The values at the vertical axis are α from Eq. (4.10). The dashed line shows the marginal stability of a horizontal flow, whereas the solid line is the stability limit for full toroidal and poloidal flow.

The stability diagrams in Figure 4.8 showing the amplitude of differential rotation versus magnetic field strength illustrates the two regimes of the hydrodynamic and magnetic instabilities. The lines of marginal stability for a magnetic Reynolds number of $\mathrm{Rm} = 10\,000$ are plotted in terms of the surface differential rotation parameter α versus the ratio of Lundquist number to Reynolds number (with the latter being fixed). The solid line gives the marginal stability for computations with a full flow, as it would be expected in an unstratified sphere. The dashed line is for a flow restricted to horizontal motions or, in technical terms, without poloidal flow.

Figure 4.8 (left) shows that there is a clear separation of the two instabilities. If the magnetic field is small, the hydrodynamic instability (Watson instability) is nearly unaffected as indicated by the horizontal branch of the stability line. The field strength necessary for the magnetic instability (Tayler instability) alone is found on the horizontal axis of the diagram. This minimum magnetic field does not change significantly if differential rotation is added. This is the vertical branch of the stability line. In case of a purely horizontal flow, a stabilizing effect by weak magnetic fields is observed which slightly suppresses the Watson instability at not too large magnetic field strengths. This effect, however, becomes smaller when one goes to larger magnetic Reynolds numbers whence smaller magnetic diffusivities. The marginal line with a slightly positive slope merges with the line of marginal stability coming from the purely magnetic part of the diagram at $\alpha = 0$. There is no stability at all for $S/\mathrm{Rm} > 0.30$.

The thickness of the magnetic-field belts has been roughly 7% of the solar diameter in most of the results shown up to this point, except in Section 4.3.2. The same computations have been repeated with $n = 4$ in Eq. (4.5). This exponent results in a thickness of about 0.04 solar radii. The lines of marginal stability are shown in Figure 4.8(right). The left

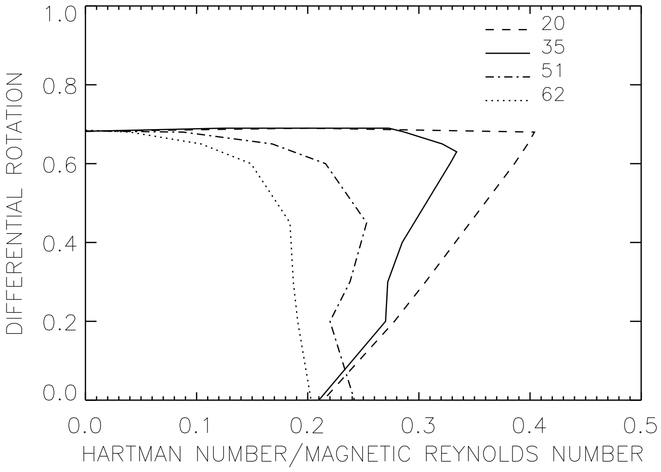

Figure 4.9: Lines of marginal stability for toroidal magnetic field belts when the eye of the toroidal field belt is placed at various latitudes. The dashed, solid, dot-dashed and dotted lines represent latitudes of 20, 35, 51 and 62 respectively. Rm = 10000 and Pm = 1.

part of the diagram shows little change. The full-flow stability line is nearly identical to the one for $n = 2$. Also the slight stabilization of differential rotation with magnetic fields occurs again in the analysis of purely horizontal flows. The strongest magnetic field is larger, however, and may reach $S/\mathrm{Rm} = 0.56$ for rigid rotation ($\alpha = 0$).

Finally, the effect of the latitudinal positions of the eye of the toroidal field belt on the instability is explored. The eye of the belt can be shifted in latitude by appropriate choice of p and q in Eq. (4.5). Here four case are chosen with the eye of the belt placed at 20 ($p = 8$, $q = 1$), 35 ($p = 2$, $q = 1$), 51 ($p = 2$, $q = 3$) and 62 ($p = 2$, $q = 7$). The results are shown in Figure 4.9. A gradual transition towards increased stability is seen in the diagram as the eye of the field belt approaches the equator. At high latitudes, the hydrodynamic stability limit is reduced as the magnetic field is increased. The critical limit of hydrodynamic stability in absence of the magnetic field is independent of the latitudinal position of the belt. The magnetic stability limit (vertical branch of the stability line) decreases slightly with stronger differential rotation for high latitudes but increases with stronger differential rotation when the belt is placed close to the equator. The magnetic stability limit in the absence of differential rotation is nearly independent of the latitudinal position of the belt, but there is a hint to increased stability at mid-latitudes. The evolution of the stability limits as a function of latitude seems to be continuous and it can be concluded that the underlying physical effects will be similar for all latitudes. Thus, the computations performed for a fixed value of differential rotation and a fixed position of the toroidal field can be taken as a representative sample of the parameter space.

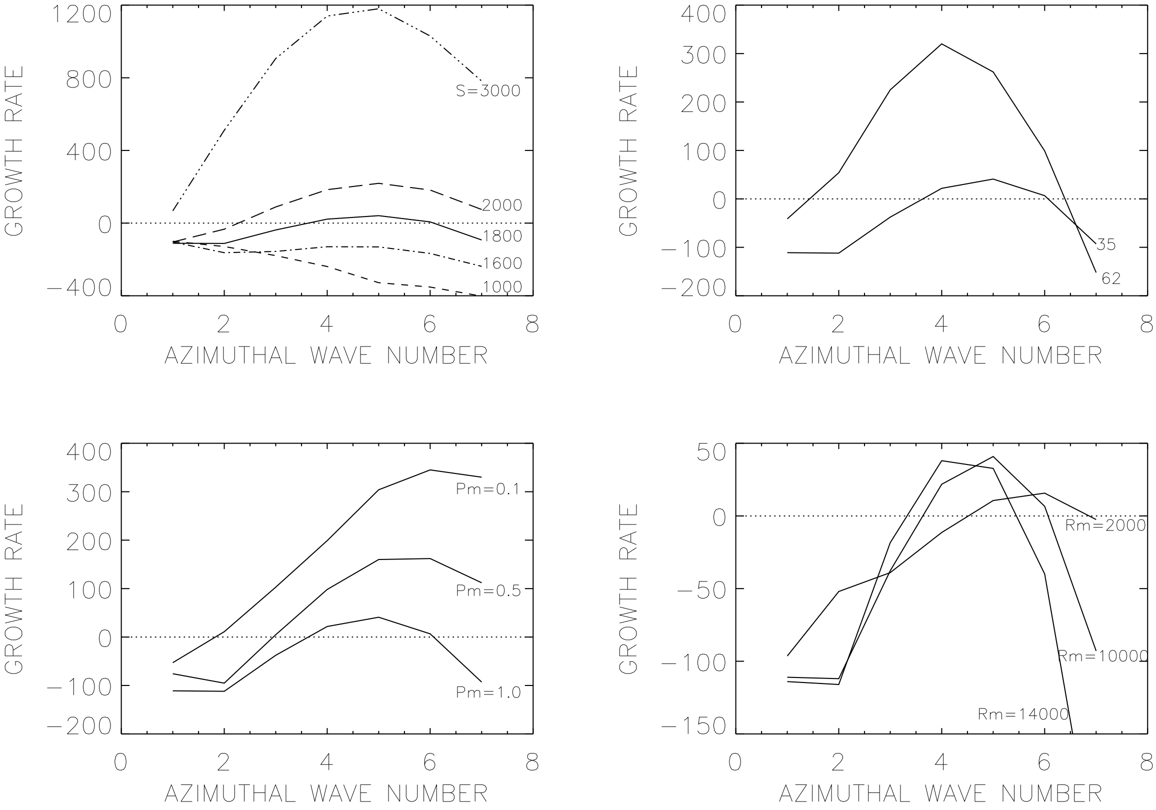

Figure 4.10: Growth rates of instabilities for higher azimuthal modes for various Lundquist numbers (top-left), different latitudes (top-right), magnetic Prandtl numbers (bottom-left) and magnetic Reynolds numbers (bottom-right). The negative growth rates indicate decay of the perturbation, i.e. stable case, and zero growth rate indicates marginal stability.

4.4 Higher Azimuthal Modes: Linear simulations

To gain further insight on the nature of the instability produced in the magnetic tachocline, it will be necessary to extend the linear computations to higher azimuthal modes. The key results from these computations are presented in this Section.

The numerical setup is unchanged from the preceding Section. Differential rotation (α_2) is fixed at 20%. This value is close to the actual differential rotation in the tachocline and as was shown in the preceding Section, the results do not change drastically for a small change in α_2 from the chosen value. Higher azimuthal modes are each excited in a different simulation to perform a linear stability analysis. The time taken for each simulation scales linearly with the azimuthal mode number, as number of azimuthal grid points increase correspondingly. Thus, to save the computational time, the growth rates of instability are measured instead of a manual search for the critical parameters of marginal stability. The growth rate here is defined as the inverse of the e-folding time of the instability,

$$\gamma = \frac{d \ln E_l}{dt} = \frac{1}{\tau_e}. \tag{4.11}$$

The time t is measured in terms of diffusion times and E_l is the kinematic energy in each latitudinal mode. It is necessary to convert this time-scale to physical times to compare them with observable physical phenomena. Using the definition of the diffusion time τ_{diff}, the e-folding time (τ_e) can be scaled in terms of the number of solar rotations or physical years.

$$t_{\text{phy}} = \tau_e \tau_{\text{diff}} = \frac{\tau_e \, \text{Rm}}{2\pi} \tau_{\text{rot}}, \tag{4.12}$$

where τ_{rot} is the rotational period of the Sun. Thus the physical e-folding time (τ_{phy}) will be

$$\tau_{\text{phy}} \approx \frac{0.1592\text{Rm}}{\gamma} \text{ rotations } \approx \frac{0.01122\text{Rm}}{\gamma} \text{ years.} \tag{4.13}$$

Thus, for example, a growth rate of 100 units for Rm of 10000 would correspond e-folding time of roughly 16 rotations or 1.1 years. The same definition of the growth rate is used in Figure 4.10. The default parameters for the simulations are Rm = 10000, $\theta = 35$ (latitude of the eye of the field belt) and Pm = 1. In the top-left panel, the growth rates for different azimuthal modes are plotted for various Lundquist numbers (S). The most striking feature of the plot is the fact that $m = 5$ is the most unstable mode of this instability. In particular, for S = 1800, where $m = 1, 2, 3$ are stable, $m = 5$ is unstable. This is in concurrence with other authors (Dikpati & Gilman 1999; Brun & Zahn 2006) who also observed smaller scale structures dominating at mid-latitude bands. The same plot shows that the choice of the most unstable mode is completely independent of the choice of the Lundquist number i.e. the strength of the magnetic field, for the Lundquist numbers close to the marginal stability and above. It can also be noted that for the $m = 1$ mode the decay rate is constant for low magnetic fields. This may happen as the strong viscosity in the simulations would require a minimum time to redistribute the angular momentum. Thus, one expects that with the lower viscosity (i.e. higher Rm) the terminal decay rate for $m = 1$ mode would be higher (more negative growth rate). This is indeed observed. The e-folding decay time scale for Rm = 14000 corresponds to 1.36 years (about 19 rotations) but seems to rise linearly with Rm as far as one can check in the simulations (Rm up to 50000). This extraordinarily high Rm could be achieved as very weak magnetic fields are sufficient to obtain the terminal decay rate of the $m = 1$ mode.

The top-right plot shows that higher azimuthal modes are unstable for only mid-latitudes in concurrence with Gilman & Dikpati (2000). When the magnetic field is placed at high latitudes, $m = 4$ is the most unstable mode rather than $m = 5$. A similar trend was observed for the magnetic field at low latitudes. The lower-left panel shows that at mid-latitudes higher azimuthal modes get unstable if the magnetic Prandtl number is lowered. However, for the Sun Pm ≈ 0.005 (Stix & Skaley 1990) and the most unstable mode changes from $m = 5$ to $m = 6$ only when Pm is changed from 1 to 0.1. Thus, even at the solar value, the most unstable azimuthal mode is not likely to be higher than $m = 10$. The

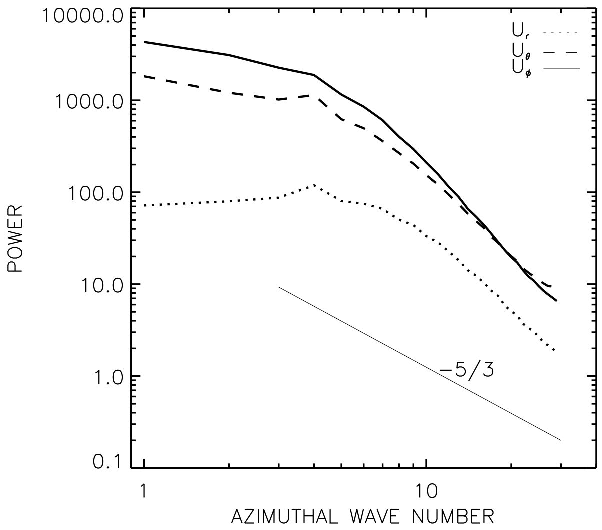

Figure 4.11: Fourier transform of the velocity fields in the non-linear simulation. The velocities $\boldsymbol{u}_r$ (dotted), $\boldsymbol{u}_\theta$ (dashed) and $\boldsymbol{u}_\phi$ (solid) are integrated over the entire computational domain and averaged over a long time-scale ($0.002\tau_{\rm diff}$ to $0.009\tau_{\rm diff}$). The Kolmogorov spectrum for hydrodynamic turbulence is plotted (slope $= -5/3$) for comparison.

last panel shows that lower azimuthal modes turn out to be the most unstable ones as Rm is increased. Thus at the solar values, the most unstable mode is likely to be $m = 1$. As a relevant node, the choice of the most unstable mode depends on the absolute difference between angular velocities of pole and equator[4]. Thus, for both configurations, Rm $= 14000$ with $\alpha_2 = 0.20$ and Rm $= 10000$ with $\alpha_2 = 0.28$, $m = 4$ is the most dominant mode of the instability. It was observed that the meridional flows caused by the instabilities at the outer surface radially penetrate for some distance, even below the layer of differential rotation. The radial flows avoid the eye of the toroidal field belts and are most dominant in the polar latitudes.

4.5 Non-linear Simulation

For the non-linear simulation, all the non-axisymmetric modes are evolved together with the axisymmetric mode. The background magnetic field given by Eq. (4.5) is merely an initial condition for this simulation. Thus, the distinction between $\boldsymbol{B}$ and $\boldsymbol{b}$ doesn't exist anymore. However, as a driving force for the flow and to maintain the tachocline thickness, $\boldsymbol{U}$ is still maintained separately from $\boldsymbol{u}$. The $\boldsymbol{u}$ now also includes axisymmetric flows forming under the influence of $\boldsymbol{U}$. The changed Eq. (4.3) & (4.4) take the form,

---

[4] $\Delta\Omega = \alpha_2 \cdot \mathrm{Rm}$

$$\begin{aligned} \frac{\partial \boldsymbol{u}}{\partial t} &= \mathrm{Rm}\big[\boldsymbol{u}\times\nabla\times\boldsymbol{U}+\boldsymbol{U}\times\nabla\times\boldsymbol{u}-\nabla(\boldsymbol{u}\cdot\boldsymbol{U})\big]+ \\ &\quad \mathrm{Rm}^2\big[\boldsymbol{U}\times\nabla\times\boldsymbol{U}-\nabla\boldsymbol{U}^2\big]+\boldsymbol{u}\times\nabla\times\boldsymbol{u}- \\ &\quad \nabla\boldsymbol{u}^2+(\nabla\times\boldsymbol{b})\times\boldsymbol{b}\ -\nabla p+\mathrm{Pm}\triangle\boldsymbol{u}, \qquad (4.14) \\ \frac{\partial \boldsymbol{b}}{\partial t} &= \nabla\times(\mathrm{Rm}\,\boldsymbol{U}\times\boldsymbol{b}+\ \boldsymbol{u}\times\boldsymbol{b})-\triangle\boldsymbol{b} \qquad (4.15) \end{aligned}$$

The set-up uses Rm = 10000 , Pm = 1, $\alpha_2 = 0.2$ and S = 2700. Here S only denotes the initial strength of the magnetic field and is chosen to be highly super-critical for linear simulations with identical parameters. Due to high magnetic diffusivity, the magnetic field decays fast leaving not much possibility to see an instability coming up in the simulation. Yet, Fourier spectrum of the velocities in the terminal configuration gives indication that the setup is prone to instabilities. The Figure 4.11, shows Fourier spectrum of velocities integrated over the entire computational domain and averaged over a sufficiently long time interval after the initial readjustments. The slope of this Fourier spectrum tends to be close to $-5/3$ at the higher azimuthal modes, indicating Kolmogorov type turbulence[5]. We can interpret this as a clear sign of turbulent processes in the tachocline. Further, all the three spectra show a clear jump at the $m = 4$ mode, meaning there is inherent preference for instability in that mode. This re-confirm results in the previous section that moderately higher azimuthal modes need to be examined for complete understanding of tachocline instabilities. The surface plots of the velocity flows shown in Figure 4.12, are plotted close to the outer boundary of the simulation domain. The background rotation is subtracted from the horizontal flows to reveal the non-axisymmetric structure. These plots show superimposition of first few azimuthal modes in the flow with additional preference for $m = 4$ mode (the rightmost plot). The flows shown are few orders smaller in magnitude than the rotational velocities. In a less diffusive tachocline, the non-axisymmetric instabilities might overpower the rotational velocities.

4.6 Discussion

This Chapter examined the stability of toroidal magnetic fields in spherical geometry. Four steps were taken in understanding the stability. Belts of toroidal magnetic fields were first placed in a rigidly rotating spherical shell. A latitudinal differential rotation was then added to the configuration. The next step involved tests for a solar-like differential rotation with Ω depending on r and θ combined with the toroidal field belts and in the final step, the stability of other azimuthal modes, higher than $m = 1$, was explored.

A good estimate for the maximum possible toroidal magnetic field is already given by the calculations of a rigidly rotating sphere. Higher magnetic Reynolds numbers are accessible in that simpler setup. The dependence of the critical field strength on the Reynolds

---

[5] It means turbulence transporting energies to smaller length scales (higher wave numbers) through energy cascade.

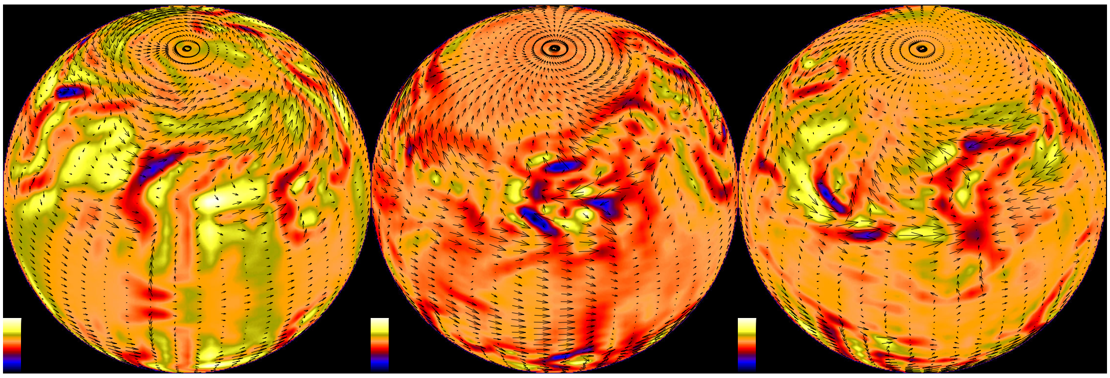

Figure 4.12: The time series evolution at the outer surface of the computational domain at, $0.003\tau_{\rm diff}$ (left), $0.006\tau_{\rm diff}$ (center) and $0.009\tau_{\rm diff}$ (right). The colors represent inwards (blue) / outwards (white) radial flows and the arrows show horizontal flows in the rotating frame of reference.

number appears to be a power-law. The extrapolation to the microscopic solar diffusivity in the tachocline leads to maximum stable magnetic fields of the order of 10 Gauss.

The hydrodynamic stability of the tachocline in a 3D setup was explored in an earlier Chapter. Starting from that point with $S = 0$, it was found that the hydrodynamic limit is weakly influenced by additional, small toroidal magnetic fields. If the fields are strong enough to excite a magnetic instability, this in turn is again weakly influenced by the amplitude of the differential rotation. In other words, the addition of differential rotation to the magnetic instability does not change the critical field strengths dramatically. This is best demonstrated in Figure 4.8.

The investigation of the lithium depletion problem showed that the microscopic magnetic diffusivity may not be sufficient to explain the observed values. A slightly turbulent state with a viscosity 10 times above the microscopic value is more likely (Vauclair 1978; Lebreton & Maeder 1987). If this factor is applied also to the magnetic diffusivity, it increases the maximum stable field strength to a slight degree. The change of critical magnetic field strengths is given by $\eta^{0.4}$ and is thus not more than one order of magnitude due to the suggested weak tachocline turbulence.

Maximum stable magnetic fields of roughly 10 Gauss are found with little dependence on the actual rotation profile used. Even though the precise limit for the toroidal magnetic field may be different by one order of magnitude from the one derived here, stable fields of 10^5 G appear unlikely. The fact that the tachocline is stably stratified does not add considerably to the stability of the magnetic fields. A decrease of the radial thickness of the magnetic-field belts does not deliver increasing critical magnetic fields. 1D or 2D computations may thus give inadequate results for the stability of magnetic fields in the solar tachocline.

The instability of fields of 10^5 G will have consequences for the dynamo process causing the 22-yr cycle of the solar magnetic field. The tachocline will then not be a location where very strong magnetic fields can be accumulated and stored. The possibility of a dynamo distributed over the convection zone, or even restricted to its upper part, was recently revived by Brandenburg (2005). This idea earns support from results produced here as only moderate magnetic fields are stable in the solar tachocline. A dynamo much closer to the surface also generates toroidal magnetic fields, and one can estimate the stability of such large-scale fields using turbulent values for the magnetic Reynolds number and the magnetic Prandtl number. The former, Rm_t, is about 1000–2000 whereas Pm_t is unity or a bit less than that (Yousef et al. 2003). The maximum stable Lundquist number is 200–300 as read from Figure 4.3 and the solid line at 30% differential rotation in Figure 4.7. With a density of about 0.01 g/cm^3 and a turbulent diffusivity of $\eta_\mathrm{t} \sim 10^{12}$ cm^2/s, these values convert to 1000–1500 Gauss which is enough to permit the fields of the suggested surface dynamo (large-scale field of a few hundred Gauss).

The positioning of the magnetic field belt at different latitudes does not dramatically change the results of the stability limits. Near equatorial latitudes, however, the magnetic stability limit is increased by the inclusion of differential rotation. The hydrodynamic stability limit is not affected by the position of the field belt.

The analysis of the plots in Figure 4.10, as presented in a preceding Section, gives indication that the $m = 1$ mode is likely to be the most unstable mode for the solar values. However, at small Rm as in the simulations, moderately higher azimuthal modes (around $m = 5$) are the most dominant ones. It will be important to reemphasise that most high latitude star-spots tend to be large indicating low azimuthal modes. On the other hand, the conventional Taylor instability clearly singles out $m = 1$ as the most dominant mode and these findings may have implications for our understanding of magnetic instabilities of toroidal fields coupled with differential rotation. Similar to dynamo processes, the choice of most unstable mode depends on absolute difference between angular velocities of the pole and equator.

The non-linear simulation re-confirms preference to moderately higher azimuthal modes over the $m = 1$ mode for the given magnetic Reynolds number. The Fourier spectrum of the velocities in the non-linear simulation indicates presence of Kolmogorov turbulence.

The idea of a tachocline formation from an internal fossil magnetic field is not affected by the instability studied here. Keeping a weak turbulent diffusion in the tachocline in mind, a critical field strength of few 100 Gauss appears roughly compatible with what has been found to be the maximum stable toroidal fields in the tachocline.

Chapter 5

Summary

Before closing, the key findings of this work are listed here.

- This work employs the idea of Rüdiger & Kitchatinov (1997) that the tachocline is formed due to a fossil poloidal magnetic field trapped in the solar interior.
- For the first time it is conclusively shown that meridional circulation changes the shape, the structure and the characteristics of the tachocline radically.
- It is found that the The tachocline is thinner at the lower values of the magnetic Prandtl number as well as at the higher values of the magnetic Reynolds number.
- It is predicted that a dipolar poloidal field of 1 Gauss would be sufficient to produce the solar tachocline.
- A scaling for the toroidal field amplitude in the solar case is derived implying it to be a few orders higher than the poloidal seed field.
- A stable temperature gradient across the shell, makes the meridional circulation shallower as well as weaker for a stronger stabilization. This can prevent lithium from reaching excessive temperatures just below the tachocline.
- A fully three-dimensional, linear hydrodynamic stability analysis of the solar tachocline shows it to be stable for the pole-equator angular velocity difference of as large as 52% for a symmetric $m = 1$ mode.
- The 3D models differ from the 2D models considering only a surface of infinitesimal thickness not in the radial flows emerging from the extension in the third dimension, but in the changed stability conditions emerging from the radial shear and the radial dependence of the differential rotation.
- The other modes, such as higher m or the different flow symmetries, have even higher stability.

- As all the meridional flows are almost horizontal, the influence of the temperature gradient across the shell is small.

- The simulations with Re > 10000 can be treated as a good approximation for the solar case for the purpose of hydrodynamic stability analysis.

- The linear MHD stability of the 3D tachocline is examined in the presence of toroidal magnetic field belts.

- The rigid sphere simulations already give a good indication of the possible magnetic instabilities produced by the toroidal magnetic field.

- The dependence of the critical field strength on the Reynolds number appears to be a power-law. The extrapolation to the microscopic solar diffusivity in the tachocline leads to a maximum stable magnetic field of the order of 10 Gauss.

- It is found that the hydrodynamic limit is weakly influenced by the additional, a weak, toroidal magnetic field.

- If the fields are strong enough to excite a magnetic instability, this, in turn, is again weakly influenced by the amplitude of the differential rotation at mid-latitudes and high-latitudes. The differential rotation stabilizes, although weakly, the magnetic instability when the belt is placed near equatorial latitudes.

- Even in a case of the tachocline being in a slightly turbulent state (the magnetic diffusivity being about 10 times its microscopic value), the change in the critical field strength is not more than one order of magnitude.

- The maximum stable magnetic field strength of roughly 10 Gauss is found to be nearly independent of the actual rotation profile used. This would mean that it is unlikely that the lower layers of the tachocline, which are only weakly turbulent, can host stable fields of the order of 10^5 Gauss.

- Even the addition of the stable stratification does not add considerably to the stability of the magnetic fields.

- A decrease of the radial thickness of the magnetic-field belts does not deliver increase in the critical magnetic fields. Thus lower dimensional models are not adequate to examine the stability of magnetic fields in the solar tachocline.

- As the tachocline cannot host the strong toroidal magnetic fields, which are prerequisite for the tachocline dynamo models, these results lend support to the dynamo models which place the seat of dynamo in the convection zone itself, like one proposed by Brandenburg (2005).

- Close to the solar surface, using the turbulent values for the magnetic Reynolds number and the magnetic Prandtl number, it can be estimated that a magnetic field of 1000–1500 Gauss would be stable against non-axisymmetric instabilities, which is enough to permit the fields of the suggested surface dynamo (a large-scale field of a few hundred Gauss).
- In the solar tachocline with microscopic diffusivities, the $m = 1$ mode is likely to be the most unstable mode. However, in the convection zone where the magnetic Reynolds number and the magnetic Prandtl number take moderate values, moderately higher azimuthal modes (around $m = 5$) are likely to be the most dominant ones.
- The choice of the most dominant azimuthal mode depends not on the magnetic diffusivity but the absolute value of pole-equator angular velocity difference.
- The non-linear simulation re-confirms preference (namely $m = 4$) to moderately higher azimuthal modes over the $m = 1$ mode for the given magnetic Reynolds number.
- The Fourier spectrum of the velocities in the non-linear simulation indicates presence of Kolmogorov turbulence.

The magnetic model of the solar tachocline self consistently explains its formation due to a weak poloidal field and shows it to be stable for a high degree of differential rotation, even when coupled with the toroidal magnetic field belts. The model presented here can be further improved by inclusion of other features like compressibility, variation of diffusivities and temperature gradients. Even in the current model, a better picture can be obtained by choosing higher magnetic Reynolds numbers and smaller magnetic Prandtl numbers. But all this would have to wait till availability of better computational resources and at this stage, the conclusions of this work, present the most comprehensive analysis of the magnetic solar tachocline.

Appendix A

Solar Parameters

The parameters most commonly used in this work are the following, with corresponding value used in all the calculations:

- The Solar Radius $R = 7 \times 10^{10}$ cm $= 7 \times 10^{8}$ m
- Equatorial rotational frequency at the base of the convection zone $f_{\mathrm{eq}} = 456$ nHz
- Equatorial angular velocity at the base of the convection zone $\Omega_{\mathrm{eq}} = 2\pi f_{\mathrm{eq}} = 2.87 \times 10^{-6}\ s^{-1}$

Following are the parameters taken from the standard solar models (see Figure A.1), helioseismology and related works (Stix & Skaley 1990). These are not as well established as the parameters above and should be treated with a degree of caution.

- the position of the base of the convection zone $R_{\mathrm{base}} = 0.7R$
  This differs slightly from the helioseismological estimates but is chosen for computational convenience.

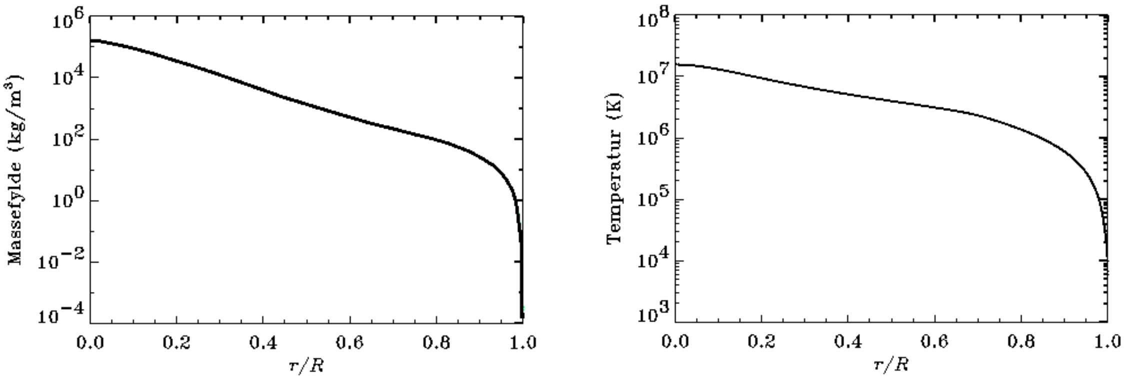

Figure A.1: Left: Radial profile of the density inside the Sun. Right: Radial profile of temperature inside the Sun.

- The density in the tachocline region $\rho_{\text{tacho}} = 0.25$ gm/cm^3
- Average density in the radiative interior $\rho_{\text{rad}} = 1$ gm/cm^3
- Temperatures at $0.1R$ and $0.7R$: 10^7 K and 10^6 K respectively.
- The average kinematic viscosity in the radiative region, $\nu = 15$ cm^2/s
- The average magnetic diffusivity in the radiative region, $\eta = 3000$ cm^2/s
- The gravitational acceleration used in the section used in section 2.4.5 $g = 5.5 \times 10^4$ cm/s^2

Appendix B

Miscellaneous Formulae

Transformation between the physical radius and non-dimensional variable x

$$r = \frac{R_{\text{out}} + R_{\text{in}}}{2} + \frac{R_{\text{out}} - R_{\text{in}}}{2} x \tag{B.1}$$

Representation of velocity field in terms of its poloidal and toroidal components

$$\boldsymbol{u} = \nabla \times (e\hat{\boldsymbol{r}}) + \nabla \times \nabla \times (f\hat{\boldsymbol{r}}) \tag{B.2}$$

$$= \begin{pmatrix} \frac{l(l+1)}{r^2} f \\ \frac{1}{r}\left[\frac{1}{\sin\theta}\partial_\phi e + \partial_r \partial_\theta f\right] \\ \frac{1}{r}\left[\frac{1}{\sin\theta}\partial_r \partial_\phi f - \partial_\theta e\right] \end{pmatrix} \tag{B.3}$$

The magnetic field can be represented similarly by potentials g and h.

Properties of individual terms of the summation in the potentials e, f, g and h:

$$\frac{1}{\sin\theta}\partial_\theta(\sin\theta\partial_\theta f') = \left(\frac{m^2}{\sin^2\theta} - l(l+1)\right) f' \tag{B.4}$$

$$\partial_\phi^2 f' = -m^2\ f' \tag{B.5}$$

where $f = \sum f'$

First few orders of Chebyshev Polynomials:

$$T_0(x) = 1 \tag{B.6}$$

$$T_1(x) = x \tag{B.7}$$

$$T_2(x) = 2x^2 - 1 \tag{B.8}$$

$$T_3(x) = 4x^3 - 3x \tag{B.9}$$

$$T_4(x) = 8x^4 - 8x^2 + 1 \tag{B.10}$$

$$T_5(x) = 16x^5 - 20x^3 + 5x \tag{B.11}$$

$$T_6(x) = 32x^6 - 48x^4 + 18x^2 - 1 \tag{B.12}$$

First few orders of Legendre Polynomials for $m = 0$:

$$P_0(\cos\theta) = 1 \tag{B.13}$$

$$P_1(\cos\theta) = \cos\theta \tag{B.14}$$

$$P_2(\cos\theta) = \frac{1}{2}\left(3\cos^2\theta - 1\right) \tag{B.15}$$

$$P_3(\cos\theta) = \frac{1}{2}\left(5\cos^3\theta - 3\cos\theta\right) \tag{B.16}$$

$$P_4(\cos\theta) = \frac{1}{8}\left(35\cos^4\theta - 30\cos^2\theta + 3\right) \tag{B.17}$$

$$P_5(\cos\theta) = \frac{1}{8}\left(63\cos^5\theta - 70\cos^3\theta + 15\cos\theta\right) \tag{B.18}$$

$$P_6(\cos\theta) = \frac{1}{16}\left(231\cos^6\theta - 315\cos^4\theta + 105\cos^2\theta - 5\right) \tag{B.19}$$

Other properties:

$$T_{k+1}(x) = 2\ x\ T_k(x) - T_{k-1}(x) \tag{B.20}$$

$$P_{l+1}(\cos\theta) = \frac{1}{l+1}\Big[(2l+1)\ \cos\theta\ P_l(\cos\theta) - l\ P_{l-1}(\cos\theta)\Big] \tag{B.21}$$

Acknowledgements

I am here to thank all the people who directly and indirectly helped me in my research as well as writing the thesis. This thesis wouldn't have been possible without support, encouragement and help of many people.

First of all, I would like to thank my advisor, Prof. Günther Rüdiger. He has been very helpful and patient at various stages of my thesis. His wonderful insight into the subject, made my time spent in Potsdam, an efficacious learning experience. His efforts to find second grant for the last one year of the PhD cannot be thanked in any words. His constructive and timely suggestions helped significantly in improving the thesis.

Dr. Rainer Arlt's command over the numerical code and his inputs in the physical interpretation provided an ideal foil to Prof. Rüdiger's 'back to basics' approach. Rainer helped me understand the Hollarbach code and also shared a lot of simulation work. It was a pleasure working with him and I thoroughly enjoyed our discussions on the academic as well as non-academic – be it amateur telescopes or cameras and photography or travelling – matters. He, along with Rashmi – my wife –, also carefully proof-read the thesis to keep it error-free. The help and support of Prof. S. M. Chitre during the final stages of the thesis was very valuable in improving the thesis.

Deutsche Forschungsgemeinschaft should be thanked for their funding through grant number Ru 488/15-1.

This was my first experience of living outside India and it turned out to be a memorable one because of good friends I got inside and outside the institute. It is difficult to name everyone in the limited space but atleast some names deserve to be mentioned. My fellow PhD students from MHD group, Dr. Milijenko Cemeljic, Dr. Natalia Dzyurkevich, Pavel Egorov, Martha Zub, Stavaro Ivanovski, Jasak Szklarski, Oliver Gressel helped a lot. Friends from other research groups within the institute like Dr. Sanjib Sharma, Dr. Robert Piontek, Franziska Köckert, Arman Khalatyan, Christian Maulbetsch, Dr. Christian Fendt, Dr. Karl-Heinz Böning and Dr. Marc Verheijen made my hours spent within the institute memorable ones. All my friends in Berlin and Potsdam, Anand, Manohar, Krishnan, Atul, Padmanabhan, Nimisha, Deepika, Mahesh, Amit and Ram have ensured that my years in Germany will always be cherished in my memory. I want to take many more names here but have to keep this short.

It is not possible to dedicate oneself exclusively to research without full support of the family. My brother Abhishek, my parents and my dear wife Rashmi, all supported me in every manner possible and made sure I stay focused on my work. I simply cannot thank them enough.

Bibliography

Acheson, D. J. 1978, Phil.Trans.Roy.Soc.Lon., A289, 459

Antia, H. M., Basu, S., & Chitre, S. M. 1998, , 298, 543

Arlt, R., Sule, A., & Rüdiger, G. 2005, , 441, 1171

Balbus, S. A., & Hawley, J. F. 1992, , 400, 610

Basu, S. 1997, , 288, 572

Basu, S., & Antia, H.M. 2001, , 324, 498

Brandenburg, A., 2005, , 625, 539

Braithwaite J. 2006, , in press (astro-ph/0512182)

Brown T. M., Christensen-Dalsgaard, J., Dziembowski, W. A. et al. 1989, , 343, 526

Brun, A. S., & Zahn, J.-P. 2006, , 457, 665

Caligari, P., Moreno-Insertis, F., & Schüssler, M. 1995, , 441, 886

Cally, P. S. 2003, , 339, 957

Cally, P. S., Dikpati, M., & Gilman, P. A. 2003, , 582, 1190

Charbonneau, P., & MacGregor, K.B. 1993, , 417, 762

Charbonneau, P., Dikpati, M., & Gilman, P. A. 1999, , 526, 523

Charbonneau, P., Christensen-Dalsgaard, J., Henning, R. et al. 1999, , 527, 445

Choudhuri, A.R., & Gilman P.A., 1987, , 316, 788

D'Silva, S. & Choudhuri, A. R. 1993, , 272, 621

Dikpati, M., Cally, P., & Gilman, P. A. 2004, , 610, 597

Dikpati, M., & Gilman P. A. 1999, , 512, 417

Dikpati, M., & Gilman P. A. 2001, , 551, 536

Dikpati, M., Gilman, P. A., & Rampel, M. 2003, , 596, 680

Dziembowski, W., & Kosovichev, A. 1987, Acta Astronomica, 37, 341

Eff-Darwich, A., Korzennik, S. G., & Jiménez-Reyes, S. J. 2002, , 573, 680

Elliott, J. R. 1997, , 327, 1222

Ferraro, V.C.A. 1937, , 97, 458

Ferriz-Mas, A. & Schüssler, M. 1996, GAFD, 81, 233

Forgács-Dajka, E., & Petrovay, K. 2002, , 389, 629–640

France K., "Standard Solar Model", www.pha.jhu.edu/ france/PAPERS/solmodel.pdf

Garaud, P., "Dynamics of the solar tachocline" 2000, PhD dissertation, University of Cambridge

Garaud, P. 2001, , 324, 68

Garaud, P. 2002, , 329, 1

Gilman, P. 1970, , 162, 1019

Gilman, P., & Dikpati, M. 2000, , 576, 1031

Gilman, P. A., & Fox, P. 1997, , 484, 439

Gough, D.O., & McIntyre, M.E. 1998, , 394, 755

Grec, G., Fosset, E., & Pomerantz, M. 1980, , 288, 541

Guenther, D.B., Demarque, P., Kim, Y.-C. et al. 1992, ApJ, 387, 372

Hollerbach, R. 1994, Phys. Fluids 6, 2540

Hollerbach, R. 2000, Int. J. Numer. Meth. Fluids, 32, 773

Howe, R., et al. 2000, Sci, 272, 1296

Howe, R., Christensen-Dalsgaard, J., Hill, F., et al., 2000, Sci, 287, 2456

Howe, R. 2002, confernce talk, http://www.noao.edu/staff/rhowe/dyn2k2bb/v3dcmnt.htm

Howe, R. 2003, Proc. SOHO 12/ GONG+ 2002, 81

Kippenhahn, R., & Weigert, A. 1994, Stellar Structure and Evolution. Springer

Komm, R., Howe, R., Durney, B.R., Hill, F., 2003, ApJ, 586, 650

Kosovichev, A. G. 1996, , 469, L61

Kosovichev, A. G., Schou, J., Scherrer, P. H. et al. 1997, , 170, 43

Lebreton, Y. & Maeder, A., 1987, , 175, 99

Leighton, R. B., Noyes, R. W. & Simon, G. W. 1962, , 135, 474

MacGregor, K.B., & Charbonneau, P. 1999, , 519, 911

Malkus, W. V. R. 1967, J. Flu. Mech., 28, 793

Malkus, W. V. R. 1968, Tellus, XX, 3

Miesch, M. 2003, , 586, 663

Newton, H. W. & Nunn, M. L. 1951, , 111, 413

Parker, E. N. 1955, , 121, 491

Petrovay, K. 2003, , 215, 17

Pitts, E. & Tayler, R.J. 1986, , 216, 139

Rempel, M., Schüssler, M., & Tóth, G. 2000, , 363, 789

Rüdiger, G., & Kitchatinov, L. 1997, Astron. Nachr., 318, 273

Rüdiger, G., Kitchatinov, L., & Arlt, R. 2005, , 444, L53

Rüdiger, G., & Pipin, V. V. 2001, , 375, 149

Rüdiger, G., Schultz, M., 2006, in prep.

Schou, J., Antia, H. M., Basu, S. et al. 1998, , 505, 390

Schou, J., Howe, R., Basu, S., et al. 2002, , 567, 1234

Spiegel, E.A., & Zahn, J.-P. 1992, , 265, 106

Spruit, H. C. 1999, , 349, 189

Spruit, H. C. 2002, , 381, 923

Stix, M., & Skaley, D. 1990, , 232, 234

Tayler, R.J. 1973, , 161, 365

Thompson, M. J., Toomre, J., Anderson, E. et al. 1996, Sci, 272, 1300

Thompson, M. J., Christensen-Dalsgaard, J., Miesch, M., & Toomre, J. 2003, , 41, 599

Vauclair, S., Vauclair, G., Schatzman, E. et al. 1978, , 223, 567

Velikhov, E. P. 1959, J.Exp.Theo.Phys. (USSR), 36, 1398

Watson, M. 1981, GAFD, 16, 285

Yousef, T.A., Brandenburg A. & Rüdiger, G. 2003, , 411, 321

Zhang, K., Liao, X. & Schubert, G. 2003, , 585, 1124